

# **Simulation of the Interaction of Positively Charged Beams and Electron Clouds**

Dissertation

zur Erlangung des akademischen Grades

Doktor-Ingenieur (Dr.-Ing.)

der Fakultät für Informatik und Elektrotechnik

der Universität Rostock

Rostock, 2013

**vorgelegt von**

Aleksandar Marković,  
geboren am 07.02.1978 in Skopje, Mazedonien

**Gutachter:**

Prof. Dr. rer. nat. habil. Ursula van Rienen,  
Universität Rostock, Institut für Allgemeine Elektrotechnik

Dr. Rainer Wanzenberg,  
Deutsches Elektronen-Synchrotron (DESY)

Prof. Dr. Andreas Jankowiak,  
Humboldt-Universität zu Berlin, Institut für Physik

**Datum der Einreichung:** 28. Juni 2013

**Datum der Verteidigung:** 28. Oktober 2013





X



# Contents

<b>1</b>	<b>Introduction</b>	<b>1</b>
<b>2</b>	<b>Linear Beam Dynamics in Storage Rings and Collective Effects due to Electron Clouds</b>	<b>3</b>
2.1	Charged Particle Dynamics in Electromagnetic Fields . . . . .	4
2.1.1	Non-relativistic Charged Particles . . . . .	4
2.1.2	Lorentz Transformation . . . . .	5
2.1.3	Energy and Momentum of a Relativistic Particle . . . . .	7
2.1.4	Lorentz-Transformed Electric and Magnetic Field . . . . .	8
2.1.5	Relativistic Equation of Motion . . . . .	11
2.2	Linear Transverse Beam Dynamics and Beam Size Parameters	13
2.2.1	Common Definition of a Bunch in a Storage Ring . . . . .	13
2.2.2	Equations of Transverse Motion . . . . .	15
2.2.3	Solution of the Equations of Motion and Linear Beam Optics with Transport Matrices . . . . .	18
2.2.4	Transverse Tune . . . . .	21
2.2.5	Phase-Space Ellipse and Particle Emittance . . . . .	23
2.2.6	Beam Emittance . . . . .	24
2.3	Collective Effects . . . . .	27
2.3.1	Direct Space Charge . . . . .	27
2.3.2	Wake Fields and Impedances . . . . .	29
2.4	Electron Clouds and Induced Instabilities . . . . .	32
2.4.1	Generation of Electron Clouds . . . . .	32
2.4.2	Electron Cloud Effects . . . . .	35
2.5	Summary of the Chapter . . . . .	39
<b>3</b>	<b>Modelling and Implementation of Particle Tracking</b>	<b>41</b>
3.1	Electrostatic Macro-Particle Model . . . . .	42
3.2	Tracking Cycle . . . . .	44
3.3	Charge Weighting . . . . .	47
3.4	Computation of 3D Space Charge Fields of Charged Particle Distributions . . . . .	49
3.4.1	Discretization of the Poisson Equation . . . . .	50
3.4.2	Discrete Poisson Equation in a Domain with Elliptical Cross-Section . . . . .	53
3.4.3	Space Charge Field Computation for Different Boundary Conditions . . . . .	57

3.4.4	Computation of the electric field for relativistic bunches	62
3.4.5	Comparison of the transverse field with analytical Bassetti-Erskine expression . . . . .	62
3.5	Interpolation of the Electrical Field . . . . .	67
3.6	Integration of the Equations of Motion . . . . .	70
3.6.1	Tracking of Relativistic Particles . . . . .	72
3.6.2	Comparison of MOEVE PIC Tracking with other PIC Programs . . . . .	76
<b>4</b>	<b>Interaction of a Positively Charged Bunch with an Electron Cloud</b>	<b>81</b>
4.1	3D self-consistent PIC Simulation of the Interaction . . . . .	81
4.1.1	Interaction Forces . . . . .	83
4.2	Simulation Studies . . . . .	84
4.2.1	Bunch Particles . . . . .	84
4.2.2	Electron Cloud Particles . . . . .	86
4.2.3	Interaction in a Dipole Field . . . . .	92
<b>5</b>	<b>Numerical Estimation of Electron Cloud Effects on a Single Bunch</b>	<b>97</b>
5.1	Coherent Tune Shift due to an Electron Cloud . . . . .	98
5.1.1	Betatron Tune . . . . .	98
5.1.2	Numerical Computation of the Tune Shift . . . . .	100
5.2	Incoherent Effects of Electron Clouds . . . . .	103
5.2.1	Head - Tail Simulation with Vertically Displaced Parts of the Bunch . . . . .	104
5.2.2	Wake Field induced by Electron Cloud . . . . .	107
5.3	Two-Variable Wake Field induced by an Electron Cloud . . . . .	110
5.4	Tracking with a Pre-Computed Wake Matrix . . . . .	113
5.4.1	Properties of the Two-Variable Wake Field . . . . .	113
5.5	Single Bunch Instability . . . . .	118
5.5.1	Tracking of a Positron Bunch in the KEKB-LER with a pre-computed Wake Matrix . . . . .	119
5.6	Study for the PETRA III Storage Ring operated with Positron Beam . . . . .	120
<b>6</b>	<b>Summary</b>	<b>129</b>
<b>A</b>	<b>Machine Parameter</b>	<b>131</b>
A.1	PETRAIII . . . . .	131
A.2	KEKB-LER . . . . .	132
A.3	ILC damping ring . . . . .	132

Contents	v
<b>B Input file</b>	<b>133</b>
<b>Bibliography</b>	<b>135</b>



# Introduction

---

The simulation of beam instabilities due to electron clouds is a highly active field of research. These instabilities may generally occur in storage rings operated with bunches of positively charged particles. The storage rings are being build for different purposes as for instance a particle collider (e.g. the Large Hadron Collider or LHC [Brüning 2004]), a high-brilliance synchrotron radiation source (e.g. PETRA III [Balewski 2004]) or lower energy storage rings for medical purposes etc.. Also, the present and the future terascale accelerator projects as the International Linear Collider (ILC) have, apart from the main accelerator, storage rings for preconditioning of the beam before it enters the main accelerator. Regardless of the type or the purpose of the storage ring the requirements for the beam quality are very strict.

If the storage ring is operated with bunch filling patterns which are favourable to the growth of the electron cloud density, i.e. long bunch trains with short intra-bunch distances, the density of electrons is rapidly growing until a saturation density has been achieved. The electron cloud changes its transverse centroid position very fast during the passage of even a single bunch only. This is due to the strong focusing transverse field of the highly relativistic positively charged bunch. As the density of the electrons near the beam axis grows, its impact on the beam becomes stronger. The interaction of the electron cloud with the bunch could result in a fast beam loss if the electron density is above a certain threshold value which triggers a fast coherent beam instability. However, the beam could also become unstable due to the interaction with electron cloud densities below that threshold. Thereby the particles in the bunch are differently affected by the electron cloud which results in a spread of their betatron frequencies. This incoherent effect appears due to the perturbation of the electron cloud from the head parts of the bunch and the subsequent transverse kick from the electron cloud on the tail parts of the same bunch. The effect is known as the head-tail effect since the transverse position of the head and the tail of the bunch are coupled through the electron cloud. The head-tail effect is manifested through a relatively slow but steady emittance growth and an incoherent tune shift of the single bunches. Fortunately, the incoherent motion of the particles is damped by the synchrotron motion of the particles in the bunch. However, in many modern

synchrotron machines, the synchrotron period is relatively long so that the incoherent instability may still lead to a significant deterioration of the beam quality. Thus, the computational estimation of the beam stability over many turns through the ring is very important, especially during the design phase of an accelerator. The following work deals with this very challenging task to estimate the single bunch instability due to the electron cloud.

The first chapter introduces the basic concepts of charged particle dynamics in storage rings and gives a very short overview of the collective effects on the beam with special focus on the electron cloud phenomena.

The second chapter introduces the particle tracking program *MOEVE PIC Tracking* which can track a single bunch under the influence of its own and external electromagnetic fields.

MOEVE PIC Tracking was created during this work to simulate the interaction of the relativistic bunch and initially static electrons. For the interaction simulations presented in the third chapter, the bunch and the cloud are represented by a 3D distribution of macro-particles in an elliptical beam pipe. The macro-particles are defined in the six-dimensional phase space  $\psi(x, p_x, y, p_y, z, p_z)$  and typical values of their number are of order  $10^6$  for both species. The interaction is simulated during the bunch passage through an electron cloud of certain length with or without the presence of external magnetic field. The simulations give an in-depth knowledge of the behavior of the bunch and the electrons during the interaction.

The last chapter starts with a numerical estimation of the coherent tune shift of a positron bunch due to the interaction with an electron cloud of certain density. Further, the simulations with transversally displaced parts of the bunch illustrate the head-tail effect which resembles a short-range wake field. In order to simulate the stability of a single bunch, the bunch particles are tracked through the linear optics of the machine. Thereby the action of the electron cloud on the bunch is approximated by a transverse wake kick which is applied on each turn. The idea of K. Ohmi to slice the 3D bunch and compute a wake function from every longitudinal slice of the bunch backwards, leads to a triangular wake matrix. In order to apply the computed wake matrix for the bunch tracking, properties of the wake field such as time invariance, superposition and linearity are supposed. A MOEVE PIC Tracking simulation of the interaction of the bunch with an electron cloud yields the wake kick on the tail particles for an offset in the transverse centroid position of the head parts. With such a pre-computed wake matrix, the stability of a single bunch is investigated by tracking it through the linear optics of the ring while at each turn applying the kick from the electron cloud. The simulation results for KEKB-Low Energy Ring beam and for the PETRAIII beam scrubbing runs in 2012 are in a good agreement with the measurements.



# Linear Beam Dynamics in Storage Rings and Collective Effects due to Electron Clouds

---

## Contents

<b>2.1</b>	<b>Charged Particle Dynamics in Electromagnetic Fields</b>	<b>4</b>
2.1.1	Non-relativistic Charged Particles . . . . .	4
2.1.2	Lorentz Transformation . . . . .	5
2.1.3	Energy and Momentum of a Relativistic Particle . . .	7
2.1.4	Lorentz-Transformed Electric and Magnetic Field . .	8
2.1.5	Relativistic Equation of Motion . . . . .	11
<b>2.2</b>	<b>Linear Transverse Beam Dynamics and Beam Size Parameters</b> . . . . .	<b>13</b>
2.2.1	Common Definition of a Bunch in a Storage Ring . . .	13
2.2.2	Equations of Transverse Motion . . . . .	15
2.2.3	Solution of the Equations of Motion and Linear Beam Optics with Transport Matrices . . . . .	18
2.2.4	Transverse Tune . . . . .	21
2.2.5	Phase-Space Ellipse and Particle Emittance . . . . .	23
2.2.6	Beam Emittance . . . . .	24
<b>2.3</b>	<b>Collective Effects</b> . . . . .	<b>27</b>
2.3.1	Direct Space Charge . . . . .	27
2.3.2	Wake Fields and Impedances . . . . .	29
<b>2.4</b>	<b>Electron Clouds and Induced Instabilities</b> . . . . .	<b>32</b>
2.4.1	Generation of Electron Clouds . . . . .	32
2.4.2	Electron Cloud Effects . . . . .	35
2.4.2.1	Beam Instabilities due to Electron Clouds . .	36
<b>2.5</b>	<b>Summary of the Chapter</b> . . . . .	<b>39</b>

---

## 2.1 Charged Particle Dynamics in Electromagnetic Fields

### 2.1.1 Non-relativistic Charged Particles

In this work the term particle will be used to describe a charged particle without spatial extension which is situated at position  $\mathbf{r} = (x, y, z)$  at a certain time  $t$ . The attributes of each particle are the mass  $m$ , the charge  $q$  and its velocity  $\mathbf{v} = (v_x, v_y, v_z)$ . An external electromagnetic force  $\mathbf{F}$  has to be applied in order to affect the motion of the charged particle. The force expressed by the Lorentz equation depends on the applied external electric and magnetic field:

$$\mathbf{F} = q(\mathbf{E} + \mathbf{v} \times \mathbf{B}). \quad (2.1)$$

The term  $q\mathbf{E}$  in equation (2.1) stands for that part of the force due to the applied electric field  $\mathbf{E}$  and the second part  $q(\mathbf{v} \times \mathbf{B})$  is the force resulting from the presence of an external magnetic field, represented by the magnetic flux density  $\mathbf{B}$ . An important conclusion from the Lorentz equation is that the rise of the particles energy depends on the electric field  $\mathbf{E}$  applied in the direction of motion. The force from the applied magnetic field  $\mathbf{B}$  changes the direction of the particle's motion, as this part of the force acts perpendicularly to the direction of motion ( $\mathbf{v} \times \mathbf{B}$ ). An immediate consequence is that the acceleration with resonating electromagnetic fields is only possible with modes where the  $\mathbf{E}$ -field has a strong component in the direction of motion and the  $\mathbf{B}$ -field is zero or very small at the position of the accelerated particles.

Any description of charged particle dynamics starts with the second Newton's law of motion. Applied to a particle (not necessarily a charged one) it provides a relation between the rate of change of the particle's velocity  $\mathbf{v}$ , its mass  $m$  and the force  $\mathbf{F}$  applied to the particle. Introducing the momentum  $\mathbf{p} = (p_x, p_y, p_z)$  as a variable proportional to the mass  $m$  and the velocity  $\mathbf{v} = d\mathbf{r}/dt$ ,

$$\mathbf{p} = m\mathbf{v} \quad \text{or} \quad \frac{\mathbf{p}}{m} = \frac{d\mathbf{r}}{dt}, \quad (2.2)$$

Newton's equation can be written as

$$\mathbf{F} = \frac{d\mathbf{p}}{dt} = \frac{d(m\mathbf{v})}{dt}. \quad (2.3)$$

For non-relativistic particles, the mass  $m$  appears as constant coefficient of proportionality  $m_0$  which represents the rest mass, hence Newton equation reads as:

$$\mathbf{F} = m_0 \frac{d^2 \mathbf{r}}{dt^2}. \quad (2.4)$$

From the computational point of view, (2.3) expresses the following: If the force  $\mathbf{F}$  acting on the particle is known, by integrating over the time  $t$  we obtain the new momentum  $\mathbf{p}$  which integrated again over time yields the new spatial position of the particle  $\mathbf{r}$ . The vector space spanned by the position  $\mathbf{r}$  and the momentum  $\mathbf{p}$  is called phase space. In the following chapters the phase space representation will be used to show the dynamics of charged particles.

### 2.1.2 Lorentz Transformation

Prior of considering the dynamics of relativistic charged particles it is necessary to define some terms and facts emerging from the fundamental postulates of Einstein's special theory of relativity which are described in detail in classical textbooks as [Jackson 1999], [Feynman 2006]. First, we picture the difference between the Galilean transformation and the Lorentz transformation between the coordinates of two reference systems. For that purpose we imagine the reference frames K (laboratory frame) and K' (rest frame) with parallel coordinate axes as displayed in Figure 2.1. The spatial and temporal coordinates of a single point in both frames are given as  $(x, y, z, t)$  for K and  $(x', y', z', t')$  for K'. In order to simplify the expressions it is assumed that at the moment  $t = t' = 0$  both reference frames had their coordinate origin matched at the same point. From that point in time on, the frame K' moves only in the positive  $z$ -direction with uniform velocity  $v$  relative to reference frame K.

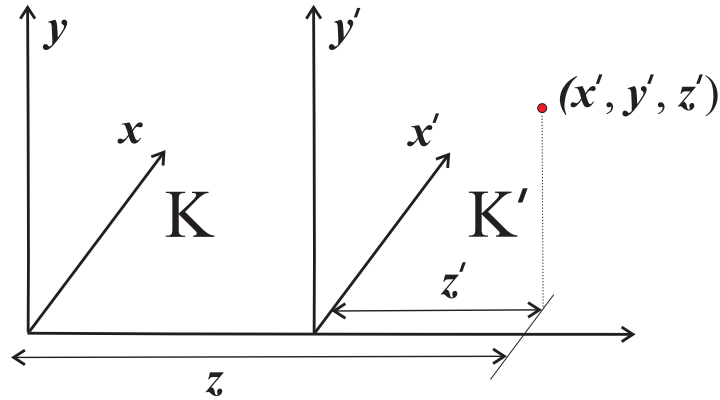


Figure 2.1: Reference frame K' moving in the positive  $z$ -direction with uniform velocity  $v$  relative to the reference frame K.

The Galilean transformation, which is intuitive and a good approximation in the classical kinematics (for velocities  $v = |\mathbf{v}|$  much smaller than the speed

of light in vacuum  $c$  ( $v \ll c$ ), assumes that the time in both frames is absolute  $t = t'$ , i.e. it runs for all observers at the same rate. Therefore, the  $z'_G$ -coordinate ( $G$  stands for a Galilean transformed coordinate) in the reference frame  $K'$  is equal to the  $z$ -coordinate in  $K$  minus the relative displacement of the frames which is proportional to the elapsed time  $t$ . Hence the relation between the coordinates in  $K$  and  $K'$  is linear:

$$z'_G = z - vt, \quad x'_G = x, \quad y'_G = y \quad \text{and} \quad t'_G = t. \quad (2.5)$$

However, the Galilean transformation is not applicable anymore if the velocity  $v$  of the reference frame  $K'$  is approaching the velocity of light  $c$ .

Then, according to the Lorentz-FitzGerald hypothesis<sup>1</sup>, the length  $\Delta z'$  of a body (which rests in the reference frame  $K'$ ), is contracted by a factor  $\gamma$  in the direction of motion of  $K'$  if observed from the reference frame  $K$ :

$$\Delta z = \frac{\Delta z'}{\gamma}. \quad (2.6)$$

The factor  $\gamma$  is known as the Lorentz factor and reads as:

$$\gamma = \frac{1}{\sqrt{1 - \frac{v^2}{c^2}}}. \quad (2.7)$$

The Lorentz factor  $\gamma \geq 1$  gets larger as the velocity  $v$  approaches the velocity of light  $c$  ( $\gamma \gg 1$ ), thus according to (2.6), the length  $\Delta z$  appears for the observer in the  $K$  (laboratory) frame  $\gamma$ -times shorter compared to the length  $\Delta z'$  in the  $K'$  (rest) frame.

Assuming a particle at rest in  $K'$  (as shown in Fig. 2.1), its  $z'$ -coordinate represents the distance to the origin in the  $z$ -direction  $\Delta z' = z' - 0$ . Applying expression (2.6), the length  $\Delta z'$  in the reference frame  $K$  will be contracted to

$$\Delta z = \frac{z'}{\gamma}. \quad (2.8)$$

On the other hand, the same distance as seen from the  $K$  frame is equal to the Galilean transformed coordinate of  $K'$ :

$$\Delta z = z'_G = z - vt. \quad (2.9)$$

Combining the last two expressions results in the Lorentz transformation of the  $z$ -coordinate between the reference frames  $K$  and  $K'$ ,

$$z' = z'_G \gamma = (z - vt) \gamma. \quad (2.10)$$

---

<sup>1</sup>Later it was proven by Lorentz that the contraction can also be applied to a movement of charged particles.

The  $x$ - and  $y$ -coordinates are not changing in this transformation

$$x' = x \quad \text{and} \quad y' = y, \quad (2.11)$$

because we assumed a special case of relative movement between the frames only in  $z$ -direction.

The Lorentz transformation of the time can be derived based on Einstein's second postulate which is the assumption that light always propagates through vacuum at definite velocity  $c$  which is independent of the speed of the light source or the one of the observer. Back to the setup with two reference frames  $K$  and  $K'$  we imagine that at time  $t = t' = 0$  (when the coordinate origins of  $K$  and  $K'$  were at the same point) a light source situated at the origin of  $K$  emits a flash of light. The light front propagates with  $c$  from the source in  $z$ -direction while the  $K'$  frame moves in the same direction with  $v < c$ . By comparing the distance of the light front to the origin of  $K'$  as seen from the observer in  $K$  and  $K'$  and having in mind that the light velocity in  $K'$  is also  $c$  we get the expression for the time measured by the observer in  $K'$

$$t' = \left(t - \frac{vz}{c^2}\right) \gamma \quad (2.12)$$

Relation (2.12) expresses the fact that the time measured in the frame  $K$  is larger than the time measured in the frame  $K'$ . Thus, we speak about time dilatation in laboratory frame  $K$ .

### 2.1.3 Energy and Momentum of a Relativistic Particle

As a consequence of the special relativity theory, the mass  $m$  and the energy  $E$  of a particle are equivalent. Einstein's famous expression for the energy

$$E = mc^2 = \gamma m_0 c^2, \quad (2.13)$$

includes the kinetic energy  $E_{kin}$  as well as the rest mass energy of a particle  $m_0 c^2$ :

$$E = E_{kin} + m_0 c^2. \quad (2.14)$$

From the definition of the relativistic mass, the relativistic momentum reads as:

$$\mathbf{p} = m\mathbf{v} = \gamma m_0 \mathbf{v} = m_0 \frac{\mathbf{v}}{\sqrt{1 - \frac{v^2}{c^2}}}. \quad (2.15)$$

Multiplying (2.15) by the speed of light  $c$  yields an expression of the momentum  $p = |\mathbf{p}|$  through the energy of the particle:

$$pc = \sqrt{E^2 - m_0^2 c^4} = m_0 c^2 \sqrt{\gamma^2 - 1}. \quad (2.16)$$

In particle accelerator physics it is common to use the unit of energy eV (electron-Volt) to express the momentum in eV/c. For highly relativistic particles where the total energy  $E \gg m_0 c^2$  (i. e.  $\gamma \gg 1$ ), the magnitude of the momentum is approximated very well by:

$$p \approx \frac{E}{c}. \quad (2.17)$$

### 2.1.4 Lorentz-Transformed Electric and Magnetic Field

In a high energy particle accelerator, a large number<sup>2</sup> of relativistic particles form a bunch. All the particles in the bunch are packed in a very small portion of the  $(x, p_x)$ ,  $(y, p_y)$  and  $(z, p_z)$  phase-space. Since all the particles in the bunch are accelerated approximately to the same velocity  $v$ , one could say that they are resting in the (center of mass) reference frame  $K'$ . On the other hand the magnets which are focusing or stirring the bunch on its way through the accelerator are at rest in the laboratory frame  $K$ . Hence, assuming a bunch motion in the  $z$ -direction of the laboratory frame  $K$ , the relative motion of the bunch rest frame  $K'$  is along the  $z$ -direction with the same velocity as the bunch.

In order to compute the dynamics of charged particles in a certain reference frame under the influence of its own and/or external electromagnetic fields (EM), it is necessary to know the field vectors  $(\mathbf{E}, \mathbf{B})$  in the respective reference frame. Thus, if  $\mathbf{E}$  and  $\mathbf{B}$  are known or computed in one frame, e.g. in the center of mass frame  $K'$ , it is necessary to transform them into the laboratory frame  $K$ . The transformation of the  $\mathbf{E}$  and  $\mathbf{B}$  field strength between two inertial systems, is a consequence of the Lorentz-transformation. The derivation and a detailed explanation are given in the lectures of R. Feynman [Feynman 2006]. For the special case of relativistic motion in the  $z$  direction only, the Lorentz-transformation for the components of  $\mathbf{E}$  and  $\mathbf{B}$  is written as:

$$E_{\parallel} = E'_{\parallel} \quad B_{\parallel} = B'_{\parallel} \quad (2.18)$$

$$E'_{\perp} = \frac{(\mathbf{E} + \mathbf{v} \times \mathbf{B})_{\perp}}{\sqrt{1 - \frac{v^2}{c^2}}} \quad B'_{\perp} = \frac{(\mathbf{B} - \frac{\mathbf{v} \times \mathbf{E}}{c^2})_{\perp}}{\sqrt{1 - \frac{v^2}{c^2}}}. \quad (2.19)$$

The longitudinal or the  $z$ -components of the field in (2.18) are denoted as  $E_{\parallel}$  and  $B_{\parallel}$  because they are parallel with the direction of the relative motion between  $K$  and  $K'$ . The transverse components of the field in  $x$  and  $y$  direction are denoted as  $E_{\perp}$  and  $B_{\perp}$  because they reside in a plane which is perpendicular to the relative motion. From (2.18) and (2.19) it is obvious that only

---

<sup>2</sup>in the order of  $10^{10}$  and higher

the transverse components of the field ( $E_x, E_y, B_x, B_y$ ) are being transformed while the longitudinal ones are invariant.

Since the main goal of this work is the investigation of the interaction between a relativistic bunch and non-relativistic electrons, the Lorentz transformation of the space charge fields of such a bunch should be specified: As previously mentioned, it is assumed that the particles of the bunch are at rest in the  $K'$  frame which moves with relativistic velocity  $v$  in the longitudinal  $z$ -direction relative to the laboratory frame  $K$ . Since the particles do not move in the bunch rest frame  $K'$  exists only their own space charge field  $\mathbf{E}'$  whereas the magnetic field in the  $K'$  frame  $\mathbf{B}'=0$ . Plugging  $\mathbf{E}'$  and  $\mathbf{B}'$  into the right hand side of expressions (2.18) and (2.19) yields  $\mathbf{E}$  and  $\mathbf{B}$  in the frame  $K$ . In expressions (2.18) and (2.19) the velocity  $v$  is taken with the opposite sign since the frame  $K$  moves with velocity  $v$  in the negative  $z$ -direction relative to the frame  $K'$ . Finally the expressions for the transformation of the space charge field in the laboratory frame can be written as:

$$E_{\parallel} = E'_{\parallel} \quad B_{\parallel} = 0 \quad (2.20)$$

$$E_{\perp} = \gamma E'_{\perp} \quad B_{\perp} = \frac{\gamma}{c^2} (\mathbf{v} \times \mathbf{E}')_{\perp}. \quad (2.21)$$

Thus, according to (2.21), in the laboratory frame  $K$  there is also a transversal magnetic field  $\mathbf{B}_{\perp}$  besides the electric field  $\mathbf{E}$ . Another fact emerging from the transformation is that the transversal component of the field in the laboratory frame  $K$  is  $\gamma$  times stronger than the transversal component computed in the center of mass frame. On the other hand, the longitudinal field computed in  $K'$  is equal to the longitudinal component in  $K$ .

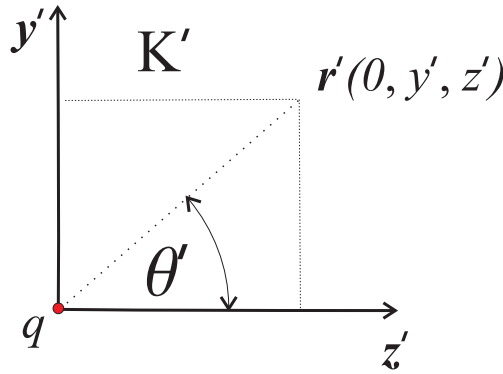


Figure 2.2:  $(z', y')$  plane in the rest frame  $K'$  of a point charge  $q$  moving with relativistic velocity (from left to right in the picture).

To illustrate this fact we transform the field of a single charged particle

$q$ , moving with uniform relativistic velocity  $v$  in  $z$ -direction, shown in its rest frame  $K'$  in Figure 2.2. The particle is situated at the origin of the  $K'$  frame. The magnitude of the  $\mathbf{E}'$  field at any point  $\mathbf{r}' = (x', y', z')$  in the  $K'$  frame is given by Coulomb's law

$$E' = \frac{q}{4\pi\epsilon_0 r'^2} = \frac{kq}{r'^2} \text{ with } k = \frac{1}{4\pi\epsilon_0}. \quad (2.22)$$

The electrostatic field lines extend radially from the particle as shown in the left part of Figure 2.3. Because of the rotational symmetry of the  $\mathbf{E}$  field, we can simplify the expressions and evaluate the field in points of the  $(y', z')$  plane  $\mathbf{r}' = (0, y', z')$  as shown in Figure 2.2. The components of the  $\mathbf{E}'$  field in a point with relative distance to the particle defined by the vector  $\mathbf{r}'$  can be written as a function of the angle  $\theta'$ :

$$E'_z = E' \frac{z'}{r'} = E' \cos(\theta') \quad E'_y = E' \frac{y'}{r'} = E' \sin(\theta'). \quad (2.23)$$

The Lorentz transformation of the coordinates provides for  $z'$  and  $y'$ :

$$z' = \gamma z = \gamma r \cos(\theta) \quad y' = y = r \sin(\theta). \quad (2.24)$$

Since  $r'$  equals

$$r' = \sqrt{y'^2 + z'^2}, \quad (2.25)$$

we could write  $r'$  in dependence of the coordinates  $(y, z)$  in  $K$ :

$$r' = \sqrt{\gamma^2 z^2 + y^2}. \quad (2.26)$$

According to (2.20) and (2.21) the corresponding transversal and longitudinal components of the field in the laboratory frame  $K$  are:

$$E_z = E_{||} = E'_z = E'_z \quad \text{and} \quad E_y = E_{\perp} = \gamma E'_y = \gamma E'_y. \quad (2.27)$$

Expressing  $E'_z$  and  $E'_y$  from (2.23) by the coordinates  $y$  and  $z$  in  $K$  we finally obtain through (2.27) the expressions for the  $\mathbf{E}$  field in  $K$  as a function of the point coordinates in  $K$ :

$$E_z = \frac{kqz\gamma}{(\gamma^2 z^2 + y^2)^{\frac{3}{2}}} \quad (2.28)$$

$$E_y = \frac{kqy\gamma}{(\gamma^2 z^2 + y^2)^{\frac{3}{2}}}. \quad (2.29)$$

Finally, the  $\mathbf{E}$  field in  $K$  is given as:

$$\mathbf{E} = \frac{kq\mathbf{r}\gamma}{(\gamma^2 z^2 + y^2 + x^2)^{\frac{3}{2}}}. \quad (2.30)$$



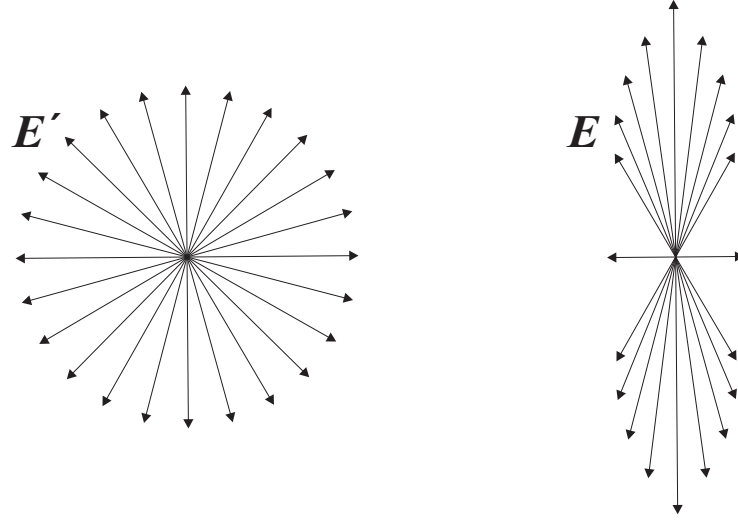


Figure 2.3: Electric field of a point charge moving with relativistic velocity (from left to right) as seen from its rest frame  $K'$  (left) and in the laboratory frame  $K$  (right).

Figure 2.3 shows the field of a single particle moving with relativistic velocity. The field lines are shown in a profile plane where the bunch moves from left to right. On the left part of the figure, the  $\mathbf{E}'$  field of the particle in its rest frame  $K'$  is given. The field is radial starting from the actual position of the particle. The right part of the same figure depicts the qualitative representation of the electric field of the same particle as seen from the laboratory frame  $K$ . In a 3D representation the field lines with same field strength build a cone with the tip on the position of the particle. In this case, the magnetic field lines are concentric around the perimeter of the cone's surface. If the velocity of the particle is very high  $\gamma \gg 1$  the cones of the  $\mathbf{E}$  field and the concentric  $\mathbf{B}$  field in the laboratory frame will be pushed together in a flat disk around the charge with the direction of motion as symmetry axis.

### 2.1.5 Relativistic Equation of Motion

After computing the electric and magnetic field in the appropriate inertial frame, the aim is to see how they affect the dynamics of the relativistic particles. In contrast to the classical Newtonian kinematics, the mass of the relativistic particles  $m = m_0\gamma$  is not constant. Since the Lorentz factor  $\gamma$  (2.7) depends on the particle velocity  $v(t)$  it means that also the Lorentz factor is a time-dependent quantity  $\gamma(t)$ . Hence, the force  $\mathbf{F}$  from (2.3) which equals

the time derivative of the momentum ( $\mathbf{p} = m_0\gamma\mathbf{v}$ ) reads as:

$$\mathbf{F} = \frac{d\mathbf{p}}{dt} = m_0 \frac{d(\gamma\mathbf{v})}{dt}. \quad (2.31)$$

Consequently, putting expression (2.31) for the force  $\mathbf{F}$  into the Lorentz equation (2.1) yields the equation of motion for relativistic particles:

$$\mathbf{F} = m_0 \frac{d(\gamma\mathbf{v})}{dt} = m_0 \frac{d(\gamma \frac{d\mathbf{r}}{dt})}{dt} = q(\mathbf{E} + \mathbf{v} \times \mathbf{B}). \quad (2.32)$$

## 2.2 Linear Transverse Beam Dynamics and Beam Size Parameters

### 2.2.1 Common Definition of a Bunch in a Storage Ring

While circulating in a storage ring, the particles loose some of their energy (e.g. via synchrotron radiation). The losses over each turn are compensated by the energy of the radio frequency (RF)  $\mathbf{E}$  field in the accelerating cavities. The fundamental resonating mode TM<sub>01</sub><sup>1</sup> (Figure 2.4) provides a strong longitudinal electric field  $E_z$  on the beam axis which in turn changes the particle momentum  $p = |\mathbf{p}|$

$$\frac{dp}{dt} = m_0 \frac{d(\gamma v)}{dt} = qE_z. \quad (2.33)$$

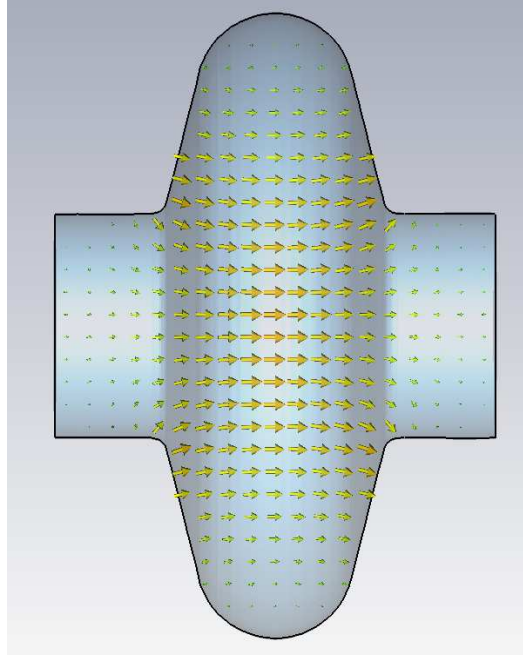


Figure 2.4: Accelerating RF  $\mathbf{E}$  field in a rotationally symmetric superconducting cavity.

The acceleration with RF cavities requires that the motion of the particles must be synchronized with the RF field in the cavity i.e. the particles should arrive in the middle of the cavity at the moment when the accelerating field reaches its maximum. Hence the particle beam has to be bunched. A bunch is an densely populated ensemble of particles in the six-dimensional phase

<sup>1</sup>TM modes (Transverse Magnetic) - no magnetic field in the direction of propagation.

space  $\psi(x, p_x, y, p_y, z, p_z)$  around the synchronous particle which is a reference particle moving in exact synchronism with the accelerating field.

The synchronous particle has always constant RF phase which enables it to gain the maximum energy from the RF field which in turn provides it with a nominal energy while orbiting the ring. In the approximation of a constant bending field, the synchronous particle would have an ideal circular orbit and all other particles which have some spatial or energy deviation would oscillate in both transversal and longitudinal direction around the synchronous particle, as principally shown in Figure 2.5.

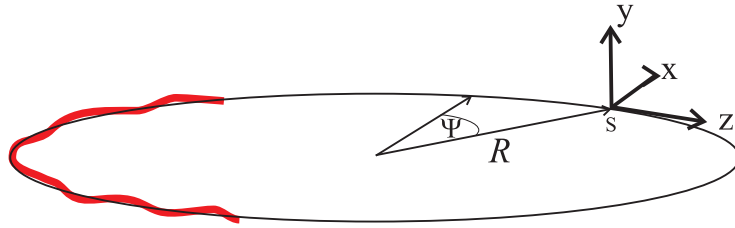


Figure 2.5: Ideal circular orbit and the possible trajectory of a real particle (red) in a storage ring with radius R.

As shown in Figure 2.7, the particles of the bunch are defined in a Cartesian coordinate system which is attached to the synchronous particle and follows its bending in the horizontal plane. Thus the longitudinal coordinate  $z$  of a particle in the bunch is always given relative to the longitudinal position of the ideal synchronous particle of the bunch. Since the synchronous particle follows the ideal orbit with the velocity  $v \approx c$  corresponding to the nominal momentum  $\mathbf{p}$ , its absolute position  $s$  along the circumference of the ring is known at any given time  $t$  as  $s = vt$ .

For highly relativistic particles the transverse components of the momentum  $p_x$  and  $p_y$  are very small compared to the longitudinal one  $p_z$ , so that the amplitude of the momentum  $|\mathbf{p}|$  nearly equals the longitudinal component  $|\mathbf{p}| \approx p_z$ . The beam in a storage ring is comprised of many bunches which circulate with the same velocity  $v \approx c$ . The position of the bunches along the circumference of the storage ring is dependent on the RF-frequency with the RF-period  $T_{RF}$  defining the shortest possible distance of two bunches in a train.

The longitudinal charge density of a bunch of  $N_p$  particles is usually given by a Gaussian distribution around the synchronous particle with local coordinate  $z = 0$ . The length of the bunch in longitudinal direction is defined through the standard deviation value  $\sigma_z$ , hence the longitudinal charge density along the bunch length is given by  $\lambda(z) = N_p / \sqrt{2\pi}\sigma_z \exp(-z^2/2\sigma_z^2)$ .

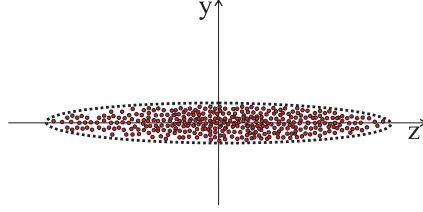


Figure 2.6: Principal representation of the longitudinal charge distribution within a bunch.

### 2.2.2 Equations of Transverse Motion

Apart from being accelerated in the electrical field provided by RF cavities the particles are guided around the ideal orbit, as principally shown in Figure 2.5, by applying a magnetic field. The transverse motion of the particles is determined by the forces from the magnetic field which should only act on the particles in the transversal  $(x, y)$  plane. The force on each individual particle is a function of the magnetic field strength at the particle position and of its energy. Several types of magnets are used for guiding the beam, of which the dipole field (defined by the magnetic flux density  $B_{y0}$ ) is used for bending the beam in the horizontal direction  $x$ . By simply equalizing the centrifugal

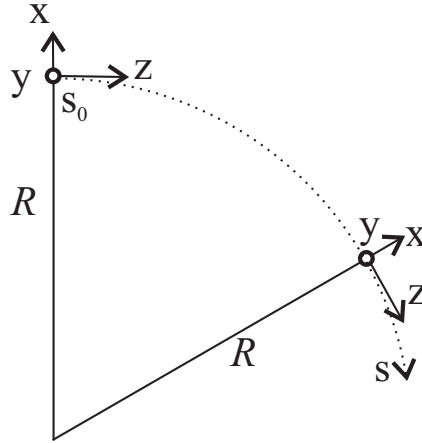


Figure 2.7: Local Cartesian system used to follow the bends in the axial "s" coordinate.

force with the dipole Lorentz force for a particle with a designed momentum  $p$  and charge  $q$ , the necessary dipole field strength  $B_{y0}$  to keep the particle circulating on the ideal orbit with radius  $R$  can be easily computed as:

$$B_{y0} = \frac{1}{R} \frac{p}{q}. \quad (2.34)$$

As a rule of thumb, if the radius of the storage ring  $R$  and the required beam energy are fixed the necessary magnetic flux density  $B$  in Tesla could be computed by the following expression:

$$B_{y0} \approx 0.3 \frac{p[\text{GeV}/c]}{R[\text{m}]}. \quad (2.35)$$

As previously mentioned, because of the longitudinal spatial deviation of the particles in the bunch (relative to the synchronous one) most particles do not experience the accelerating  $E$  field with an optimal RF phase which eventually leads to a dispersion of the particle energy in the bunch  $\Delta p$  represented by the relative momentum deviation of a particle  $\delta = \Delta p/p$ . Thus in the dipole magnets according to (2.34) the particles with momentum deviation are either bent too much if  $\Delta p < 0$  (the momentum is less than the nominal  $p$ ) or bent less than the synchronous particle if  $\Delta p > 0$ . In other words the particles with momentum deviation would have different radius of curvature

$$\rho = \frac{1}{B_{y0}} \frac{p}{q}, \quad (2.36)$$

which is either  $\rho > R$  if  $\Delta p < 0$  or  $\rho < R$  if  $\Delta p > 0$ . The change of the bending radius in the dipoles represents a particle motion in the transversal plane as a consequence of which some of the particles will have shorter and some longer orbits than the ideal orbit. In turn, even a slightly changed orbit of a particle results in a change of its longitudinal position and with it in a change of the particle's RF-phase which again yields a change in the energy of the particle.

Finally, in the longitudinal direction the particles exhibit an oscillatory motion around the synchronous particle (by which the bunch remains in an average synchronism with the RF field) - the so-called synchrotron motion. In transversal direction the particles also oscillate around the ideal orbit, not only in horizontal (due to the energy dispersion) but also in a vertical direction as well.

Thus quadrupole magnets (e.g. Figure 2.8) are used to focus the particles such that they stay in the proximity of the ideal orbit in both transversal directions  $x$  and  $y$ .

By linearizing the components of the quadrupole field with a certain gradient  $g$ , the total guiding field in the horizontal plane of both dipole and quadrupole magnets reads as:

$$B_y(x) = B_{y0} + \frac{\partial B_y}{\partial y} x = B_{y0} + gx. \quad (2.37)$$

Normalizing the  $B_y$  field with the momentum by dividing (2.37) by  $p/q$

$$\frac{qB_y(x)}{p} = \frac{qB_{y0}}{p} + \frac{qg}{p} x, \quad (2.38)$$

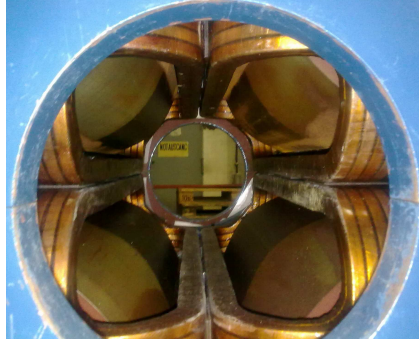


Figure 2.8: Cross-section of a quadrupole magnet (photo made at DESY).

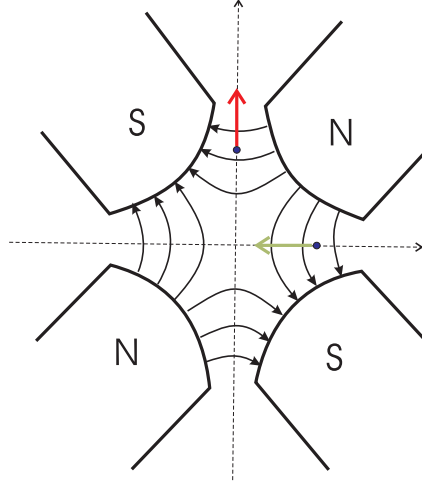


Figure 2.9: Principle view of the magnetic field lines of a quadrupole magnet. The particles are focused in the horizontal plane and defocused in the vertical plane.

replacing  $B_{y0}$  from (2.34) and wrapping  $qg/p$  as a constant  $k$  yields the following expression for the normalized linear vertical guiding field acting on the particles in the horizontal plane:

$$\frac{qB_y(x)}{p} = \frac{1}{R} + kx. \quad (2.39)$$

Finally the equations of motion of a particle in a transversal plane could be derived from the equation of non-relativistic motion<sup>2</sup> (2.3). In general, for the horizontal direction the second derivative of the particle's radial position  $\rho = R + x$  with respect to time equals the sum of the Lorentz force and the

<sup>2</sup>The oscillatory movement of the particles in the transversal plane isn't relativistic.

centrifugal force

$$m \frac{d^2(x + R)}{dt^2} = qB_y v + \frac{v^2 m}{x + R}. \quad (2.40)$$

As described in detail in [Holzer 2006] inserting  $B_y$  from (2.39) in (2.40) and replacing the independent variable  $t$  by  $s$  so that

$$\frac{dx}{dt} = \frac{dx}{ds} \frac{ds}{dt} = \frac{dx}{ds} v = x' v,$$

the equation of horizontal motion along the coordinate  $s$  reads as:

$$x''(s) + \left( \frac{1}{R^2} - k(s) \right) x(s) = 0. \quad (2.41)$$

Following the argumentation from above that the particles with spatial deviation  $x$  in the horizontal direction also have a small momentum deviation  $\Delta p$  yields the following inhomogeneous equation (Hill's equation) of particle motion

$$x''(s) + \left( \frac{1}{\rho^2(s)} - k(s) \right) x(s) = \frac{\Delta p}{p} \frac{1}{\rho(s)}, \quad (2.42)$$

whereas the motion in vertical direction only depends on the quadrupole field strength

$$y''(s) + k(s)y(s) = 0. \quad (2.43)$$

Depending on the presence of dipole or quadrupole fields along the particle trajectory  $s$  the coefficients  $1/\rho(s)$  or  $k(s)$  in (2.42) and (2.43) will take non-zero values.

### 2.2.3 Solution of the Equations of Motion and Linear Beam Optics with Transport Matrices

The general form of the equations of transverse motion (2.42) and (2.43) for a particle with nominal momentum  $\Delta p = 0$  could be written as homogeneous differential equation:

$$u''(s) - K(s)u(s) = 0, \quad (2.44)$$

which is also known as Hill's equation. The variable  $K(s)$  characterizes the magnets in both transverse directions:

$$u(s) = \begin{cases} x(s) & K(s) = \frac{1}{\rho^2(s)} - k(s), \\ y(s) & K(s) = -k(s). \end{cases}$$



Assuming a constant bending or focusing strength ( $K = \text{const}$ ) along the length  $l$  of the element <sup>3</sup> the general solution of equation (2.44) is given by:

$$u(s) = a_1 \cos(\sqrt{K}s) + a_2 \sin(\sqrt{K}s). \quad (2.45)$$

The coefficients  $a_1$  and  $a_2$  are computed from the initial conditions, i.e. for  $s = 0$  where the position  $u(0) = u_0$  and the velocity  $u'(0) = u'_0$  are known. Hence the coefficients write as  $a_1 = u_0$  and  $a_2 = u'_0/\sqrt{K}$ . Accordingly in a horizontally focusing quadrupole ( $K > 0$ ) without any bending ( $1/R = 0$ ), the motion in the horizontal plane is given by the following expressions:

$$x(s) = x_0 \cos(\sqrt{K}s) + \frac{x'_0}{\sqrt{K}} \sin(\sqrt{K}s), \quad (2.46)$$

$$x'(s) = -x_0 \sqrt{K} \sin(\sqrt{K}s) + x'_0 \cos(\sqrt{K}s). \quad (2.47)$$

The above equations (2.46) and (2.47) could elegantly be "wrapped" in a matrix form

$$\begin{pmatrix} x(s) \\ x'(s) \end{pmatrix} = \mathbf{M}_{\mathbf{QF}} \begin{pmatrix} x(s_0) \\ x'(s_0) \end{pmatrix},$$

which describes the change of  $x$  and  $x'$  along the coordinate  $s$  in a focusing quadrupole characterized by  $K$  and represented by the transformation matrix<sup>4</sup>

$$\mathbf{M}_{\mathbf{QF}} = \begin{pmatrix} \cos(\sqrt{K}s) & \frac{1}{\sqrt{K}} \sin(\sqrt{K}s) \\ -\sqrt{K} \sin(\sqrt{K}s) & \cos(\sqrt{K}s) \end{pmatrix}.$$

Similarly a quadrupole which is defocusing in the horizontal plane ( $K < 0$ ) is represented by the following transformation matrix:

$$\mathbf{M}_{\mathbf{QD}} = \begin{pmatrix} \cosh(\sqrt{K}s) & \frac{1}{\sqrt{K}} \sinh(\sqrt{K}s) \\ -\sqrt{K} \sinh(\sqrt{K}s) & \cosh(\sqrt{K}s) \end{pmatrix}.$$

In a drift part of the storage ring where no external guiding fields are present ( $K = 0$ ) the transformation matrix is given by

$$\mathbf{M}_{\mathbf{Drift}} = \begin{pmatrix} 1 & s \\ 0 & 1 \end{pmatrix}.$$

Finally the transformation matrix of a dipole sector magnet with a constant bending radius  $R$  writes as:

$$\mathbf{M}_{\mathbf{Dipole}} = \begin{pmatrix} \cos(\frac{s}{R}) & R \sin(\frac{s}{R}) \\ -\frac{1}{R} \sin(\frac{s}{R}) & \cos(\frac{s}{R}) \end{pmatrix}.$$

<sup>3</sup>A real magnet does not have a constant field along its length, especially not at the edges, thus this is a so-called hard edge model approximation.

<sup>4</sup>Determinants of the transformation matrices of the linear beam optics are always equal to one i. e.  $\det \mathbf{M} = 1$ .

Similarly the transformation matrices can be derived as well for the particle motion in  $y$ -direction. Since the particles generally move simultaneously in both transverse directions, in order to completely describe their motion in the transversal plane the trajectory vector  $\mathbf{U} = (x, x', y, y')^T$  is transformed by multiplying it with the  $(4 \times 4)$  transformation matrices comprised of two  $(2 \times 2)$  blocks on the diagonal representing the transformation in  $x$ - and  $y$ -direction. Thus, for a horizontally focusing quadrupole ( $K > 0, k < 0$ ) the transformation matrix is given by:

$$\mathbf{M}_{\mathbf{QF}} = \begin{pmatrix} \cos(\sqrt{K}s) & \frac{\sin(\sqrt{K}s)}{\sqrt{K}} & 0 & 0 \\ -\sqrt{K} \sin(\sqrt{K}s) & \cos(\sqrt{K}s) & 0 & 0 \\ 0 & 0 & \cosh(\sqrt{K}s) & \frac{\sinh(\sqrt{K}s)}{\sqrt{K}} \\ 0 & 0 & -\sqrt{K} \sinh(\sqrt{K}s) & \cosh(\sqrt{K}s) \end{pmatrix}.$$

Inserting the length  $l$  of the individual beam transport line components in the matrices above ( $s = l$ ) they would describe the transport of the particles through the individual element. Hence, if the matrices of individual elements are multiplied in their physical order along the beam line (the so-called beam magnetic lattice), the particles could numerically be transported from the initial point  $s_1$  to some point  $s_2$  down the beam line:

$$\mathbf{U}_{(s_2)} = \mathbf{M}_{(s_2, s_1)} \mathbf{U}_{(s_1)}.$$

The matrix  $\mathbf{M}_{(s_2, s_1)}$  represents the result of the multiplication of the individual transport matrices of the elements between  $s_1$  and  $s_2$ . The transport matrices are therefore perfectly suitable, during the design phase of a particle accelerator machine, to make a fast tracking of the particles through the designed magnetic lattice.

For particles with momentum deviation  $\Delta p$  the general solution of (2.42) is a sum of the solution  $x(s)$  of the homogeneous part as given in (2.44) and the particular solution  $x_i$  of the inhomogeneous equation

$$x_i''(s) - K(s)x_i(s) = \frac{\Delta p}{p} \frac{1}{\rho(s)}. \quad (2.48)$$

The particular solution  $x_i(s)$  is taken to be equal to  $x_i = D(s) \frac{\Delta p}{p}$  where  $D(s)$  is the dispersion function. The dispersion function  $D(s)$  and the bending radius  $\rho(s)$  give the lengthening of the orbit  $\delta l$  for a particle with momentum deviation  $\Delta p$ :

$$\delta l_{\Delta p} = \frac{\Delta p}{p} \oint \frac{D(s)}{\rho(s)} ds. \quad (2.49)$$

Thus, in matrix form, the equations of motion for particles with momentum deviation  $\Delta p$  read as

$$\begin{pmatrix} x(s) \\ x'(s) \end{pmatrix} = \mathbf{M}_{\mathbf{QF}} \begin{pmatrix} x(s_0) \\ x'(s_0) \end{pmatrix} + \frac{\Delta p}{p} \begin{pmatrix} D(s) \\ D'(s) \end{pmatrix}. \quad (2.50)$$

The matrix expression (2.50) could be written in a  $(3 \times 3)$ -matrix form for both directions each, hence the emerging transformation matrix  $\mathbf{M}$  for both transverse directions is a  $(5 \times 5)$ -matrix:

$$\begin{pmatrix} x(s) \\ x'(s) \\ y(s) \\ y'(s) \\ \frac{\Delta p}{p} \end{pmatrix} = \mathbf{M} \begin{pmatrix} x(s_0) \\ x'(s_0) \\ y(s_0) \\ y'(s_0) \\ \frac{\Delta p}{p} \end{pmatrix}. \quad (2.51)$$

The transformation of the particle trajectory by multiplying the position vector with the matrix from (2.51) includes the approximation that the particle focussing is independent of its momentum deviation  $\Delta p$ .

### 2.2.4 Transverse Tune

The previous section 2.2.3 briefly described how single particle trajectories could be tracked through the linearized magnet optics. Equation (2.44) is also used to describe the behavior in the transverse plane of a bunched beam of many particles of same nominal momentum  $p$ . Because of the alternating focussing along the ring the bunch particles perform an oscillatory motion in the transverse plane. These oscillations are known as betatron oscillations and are regarded in both, the vertical  $y$  and the horizontal  $x$  direction. In the horizontal direction the solution ansatz for Hill's equation is given as

$$x(s) = A f(s) \cos(\Psi(s) + \phi), \quad (2.52)$$

where the constant  $A$  and the phase  $\phi$  are integration constants. Furthermore the constant  $A$  and the amplitude function  $f(s)$  are defined to be equal to  $\sqrt{\varepsilon}$  and  $\sqrt{\beta(s)}$  correspondingly so that (2.52) can be written as

$$x(s) = \sqrt{\varepsilon} \sqrt{\beta(s)} \cos(\Psi(s) + \phi). \quad (2.53)$$

Expression (2.53) describes the betatron oscillation of the particles. Their trajectories lie within an envelope of the amplitude defined by  $\sqrt{\varepsilon \beta(s)}$  as shown in Figure 2.10. The local value of the so-called beta function  $\beta(s)$  depends on the local focussing  $K(s)$  whereas the emittance value  $\varepsilon$  is invariant

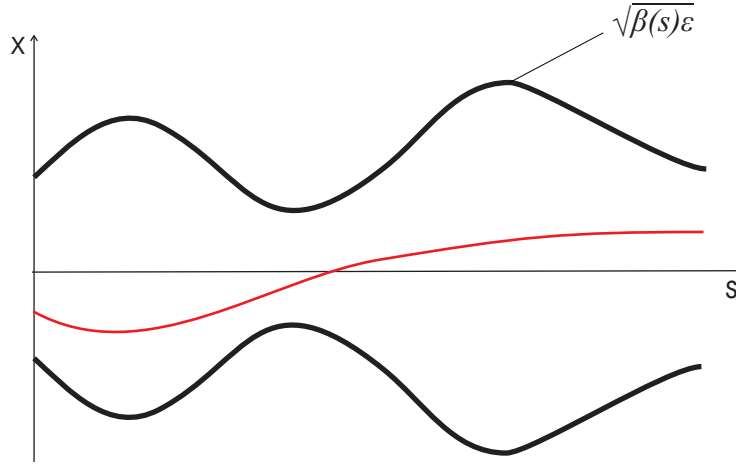


Figure 2.10: Beam envelope with an exemplary particle trajectory.

along the orbit. Inserting (2.53) in (2.44) yields the relation between the change of the oscillation phase  $\Psi(s)$  and the so-called beta function  $\beta(s)$ :

$$\Psi(s) = \int_0^s \frac{ds}{\beta(s)} \quad (2.54)$$

The beta function represents the local wavelength of the betatron oscillation  $\lambda(s) = 2\pi\beta(s)$ . In circular machines the beam optics is periodic and repeats after each turn so that  $K(s) = K(s + L)$ , where  $L$  is the length of the ideal orbit per turn. The phase change  $\Delta\Psi(s)$  of the betatron oscillation over a complete turn reads as

$$\Delta\Psi = \int_0^L \frac{ds}{\beta(s)}. \quad (2.55)$$

Thus the total number of oscillations over one turn defines the betatron tune:

$$Q = \frac{\Delta\Psi}{2\pi}. \quad (2.56)$$

In order to avoid resonances of the betatron oscillation due to imperfection in the magnet optics, the tune  $Q$  has to avoid integer as well as half-integer values. Hence for the beam stability only the fractional part of the corresponding tune is of significance.

The motion of the synchronous particle, unperturbed by the so-called collective effects (i.e. space charge forces etc.) and with the idealization of constant focusing, is modelled by the equation of a harmonic oscillator. In such a case the beta function becomes a constant value  $\beta_{x0}$  or  $\beta_{y0}$ . Then, assuming no coupling of the motion in horizontal and vertical plane, the equations of motion are given by:

$$x'' + \left(\frac{1}{\beta_{x0}}\right)^2 x = 0 \quad (2.57)$$

for the horizontal direction and

$$y'' + \left(\frac{1}{\beta_{y0}}\right)^2 y = 0 \quad (2.58)$$

for the vertical direction. The equations of motion of an unperturbed particle in the transversal plane (2.57) and (2.58) can also be written in terms of the corresponding unperturbed tunes and the ring radius  $R$ :

$$x'' + \left(\frac{Q_{x0}}{R}\right)^2 x = 0, \quad (2.59)$$

$$y'' + \left(\frac{Q_{y0}}{R}\right)^2 y = 0. \quad (2.60)$$

As previously explained, over a longer period of many revolutions the particle performs oscillatory motion in the longitudinal direction with respect to the position of the synchronous particle, also called synchrotron motion. Similarly to the definition of the betatron tune, a tune for the unperturbed synchrotron motion of the particles  $Q_{z0}$  can be defined.

Finally, the tunes are dimension-free numbers which represent the number of oscillations of a particle in  $x$ -,  $y$ - or  $z$ -direction during one revolution. While the transversal tunes are  $Q_{x0} \gg 1$  and  $Q_{y0} \gg 1$  in the longitudinal plane the particle needs much more time to perform an oscillation around the reference particle. Depending on the machine, the period of the synchrotron oscillation can take some thousands of revolutions so that  $Q_{z0} \ll 1$ .

### 2.2.5 Phase-Space Ellipse and Particle Emittance

With the defined envelope of the transverse motion as shown in Figure 2.10 it is possible to evaluate the beam size in the corresponding transverse direction at a certain position  $s$ . However, to fully describe the beam state at the position  $s$  it is necessary to know the phase, i.e.,  $x'$  or  $y'$ , as well. Computing the first derivative of the position with respect to time from equation (2.53) yields for the  $x$ -direction:

$$x'(s) = -\frac{\sqrt{\varepsilon}}{\sqrt{\beta(s)}} (\alpha(s) \cos(\Psi(s) + \phi) + \sin(\Psi(s) + \phi)), \quad (2.61)$$

where  $\alpha(s)$  is another optical function derived from  $\beta(s)$  as  $\alpha(s) = \beta'(s)/2$ . Eliminating the trigonometric terms  $\cos$  and  $\sin$  by expressing  $\cos(\Psi(s) + \phi)$

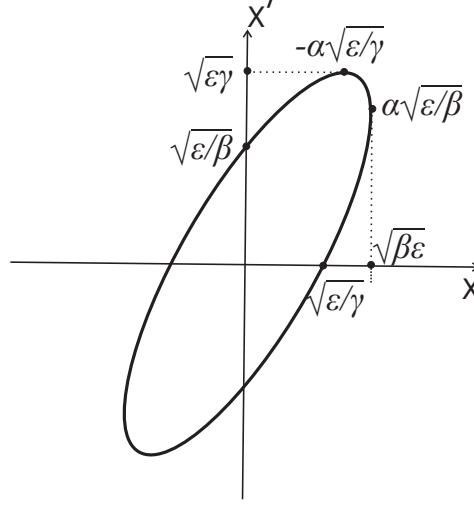


Figure 2.11: Ellipse in the phase space plane  $(x, x')$  accommodating the possible phase-space values of a single particle at a certain position in the storage ring.

through (2.53) and introducing another optical function  $\gamma(s) = \frac{1+\alpha^2(s)}{\beta(s)}$  leads to the following expression for the single particle emittance  $\varepsilon$ :

$$\gamma(s)x^2(s) + 2\alpha(s)x(s)x'(s) + \beta(s)x'^2(s) = \varepsilon. \quad (2.62)$$

The optical functions  $\alpha(s)$ ,  $\beta(s)$  and  $\gamma(s)$  are denoted as twiss-parameter. As described in [Wille 1992], the expression (2.62) represents an ellipse in the phase space plane  $(x, x')$ . Generally, as shown in Figure 2.11, the ellipse is tilted. Yet, if  $\alpha(s)$  is zero, the half axes of the phase-space ellipse are parallel with the coordinates  $x$  and  $x'$  and are equal to  $\sqrt{\varepsilon\beta}$  and  $\sqrt{\varepsilon/\beta}$ , correspondingly. Consequently, the area of the phase ellipse is  $A = \pi\varepsilon$ , which gives a physical meaning to the single particle emittance  $\varepsilon$ . Furthermore, no matter of the ellipse form, which changes along the ring with the local  $\beta$  function, its area remains constant if the motion of the particle is not perturbed. Because of the non-integer tune  $Q$ , at each turn, at a certain position  $s$  in the ring, a single particle has a new set of position and phase values within the phase space ellipse.

### 2.2.6 Beam Emittance

Under the assumption of a linear guiding optics in a storage ring, according to Liouville's theorem [Holzer 2006], the phase space volume of the particles comprising the bunch remains preserved and it is determined only by the characteristics of the beam injector system. Instead of the phase space volume, for

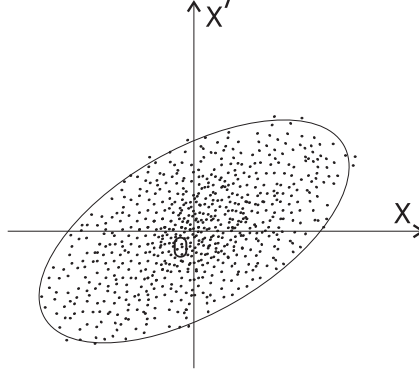


Figure 2.12: Phase space ellipse of an undistorted beam.

practical reasons its projection areas on the three orthogonal planes are considered<sup>5</sup>. Regardless of the application, for the beam quality it always applies: the smaller the effective phase space area occupied by the beam, the better the quality of the beam. However, practically the nonlinear or fringed fields of the magnets as well as a number of collective effects, here of particular interest the interaction with electron clouds, could irreversibly distort the particle distribution and with it blow up the effective phase space area/volume of the bunch. The beam emittance quantifies the ability to focus the bunch particles. In order to quantify and compare the quality of the beam as an ensemble of particles it is necessary to define the beam emittance through the smallest ellipse enclosing a certain number of bunch particles in the phase space plane. Figure 2.12 qualitatively shows the phase space ellipse of a beam which is not distorted. Figure 2.13 shows the ellipse enclosing the phase space distribution of a distorted beam. In both figures, the phase space area of the particle distribution is equal, however the envelope ellipse from Figure 2.13 takes a larger area than the one in Figure 2.12 which means that the effective phase space area of the distorted bunch is larger. Hence the emittance is an empirical quantity that characterizes the effective phase volume (or area) of a beam distribution, including the effects of irreversible processes. If the movement of the particles in the bunch is taken to be uncoupled in different directions then the emittance could be defined separately for each direction. Practically the emittance  $\varepsilon_x$  is defined as the area of the ellipse containing certain percentage of all the particles in its interior. Hence the emittance is computed as a statistical quantity in form of the rms emittance. This is especially convenient for the particle tracking programs where particle distributions are defined as an

<sup>5</sup>for emittance definition the phase space is considered as  $(x, x')$  and not the canonical  $(x, p_x)$  space

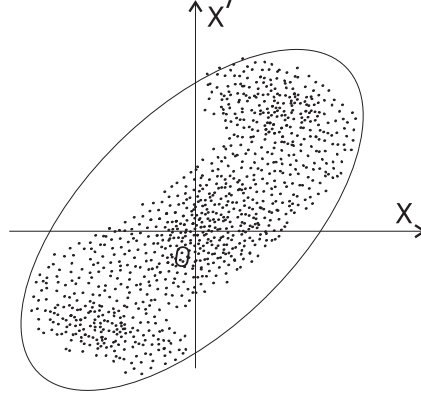


Figure 2.13: Phase space ellipse of a distorted beam.

array holding the six-dimensional phase space coordinates for each particle. Having that record, the statistical transverse emittance can be computed as:

$$\varepsilon_x = \sqrt{\overline{x^2} \cdot \overline{x'^2} - (\overline{xx'})^2}. \quad (2.63)$$

Here

$$\overline{x^2} = \frac{1}{N} \sum_{i=1}^N (x_i - \bar{x})^2, \quad (2.64)$$

$$\overline{x'^2} = \frac{1}{N} \sum_{i=1}^N (x'_i - \bar{x}')^2 \quad (2.65)$$

and

$$\overline{xx'} = \frac{1}{N} \sum_{i=1}^N (x_i - \bar{x})(x'_i - \bar{x}') \quad (2.66)$$

are the second order momenta of the particle distribution with respect to the barycenter of the distribution given by:

$$\bar{x} = \frac{1}{N} \sum_{i=1}^N x_i, \quad \bar{x}' = \frac{1}{N} \sum_{i=1}^N x'_i. \quad (2.67)$$

Finally the beam size at a position  $s$  can be computed as:

$$\sigma_{b,x}(s) = \sqrt{\varepsilon_{b,x} \beta(s)}. \quad (2.68)$$



## 2.3 Collective Effects

Main challenges in accelerator design and operation are the stability of the beam coherent motion and the preservation of the designed emittance of the particle distribution. In the first design stage, the beam optics is set up for a bunch which is reduced to a single particle without any interaction with its environment. The issues of the beam stability and quality are considered in a later phase of the vacuum chamber design by treating the beam as ensemble of many particles with the corresponding collective effects. These are rather difficult tasks considering the number of effects on the beam particles arising from the interaction of the beam with its self-field and its environment.

The beam environment of modern storage rings is the vacuum chamber with normal conducting or superconducting beam pipes and all the necessary beam-conditioning and diagnostic equipment inside.

In a broader sense the beam environment, which affects its stability, could also be vacuum impurities. Those impurities could result in trapped ions for electron beams, or electron clouds in a vacuum chamber of positively charged beams i.e. a positron-, proton- or ion-beams.

The number of effects which could harm the beam appearing as a result of the presence of many particles of same or opposite charge are called collective effects. For different beam parameters certain collective effects are more pronounced than others but nevertheless these effects always appear if the beam bears attributes like high current, high intensity or high brightness.

Independent of the type of a collective effect the additional force perturbs the motion of a bunch particle. Adding the electromagnetic perturbation force  $F_{perturb.}$  e.g. in the force equation (2.40) modifies equation (2.60) of the unperturbed motion in vertical direction:

$$y'' + \left(\frac{Q_{y0}}{R}\right)^2 y = \frac{F_{perturb.}}{mv^2} = \frac{q}{\gamma m_0 \beta_{rel}^2 c^2} (E_{perturb.} + v \times B_{perturb.})_y. \quad (2.69)$$

Hence the perturbation force changes the betatron tune  $Q_{y0}$  of the particles with velocity  $v = \beta_{rel}c$  charge  $q$  and total mass  $m = \gamma m_0$ .

### 2.3.1 Direct Space Charge

The most prominent force acting on a particle distribution packed in a bunch with a very small phase space volume is the own direct space charge force. Because of the Coulomb forces the charges of the same sign repel each other. Naturally, the space charge force acting on the bunch particles will be larger as the charge per bunch grows.

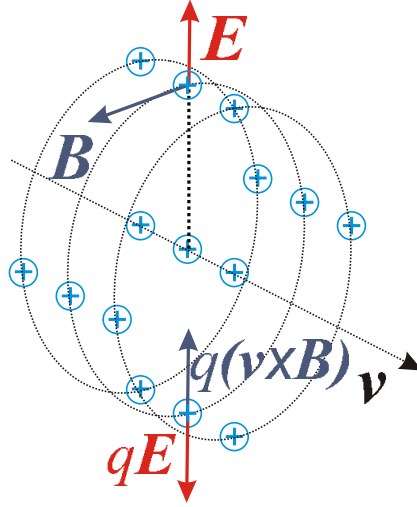


Figure 2.14: Direct space charge force on the bunch particles is in equilibrium with the force due to the own magnetic field for highly relativistic bunches.

This collective effect is usually of concern if the bunches are at low energies, i.e. at the beginning of acceleration with still low values of the Lorentz factor  $\gamma$ . The space charge force acts on the bunch particles in both transverse and longitudinal direction.

If the bunch is accelerated to a relativistic energy the repulsive force of the electric field in transverse direction is diminished by the force of the own magnetic field  $B_{\perp}$  which focuses the particles as shown in Figure 2.14. Since the transversal magnetic field  $B_{\perp}$  as shown in (2.21) depends on the own transverse electric field ( $E_{\perp} = \gamma E'_{\perp}$ ) the Lorentz force on a bunch particle in radial direction reads as:

$$F_{\perp} = \gamma E'_{\perp} - v^2 \frac{\gamma E'_{\perp}}{c^2} = \gamma E'_{\perp} \left(1 - \frac{v^2}{c^2}\right) = \gamma E'_{\perp} \frac{1}{\gamma^2} = \frac{E'_{\perp}}{\gamma}. \quad (2.70)$$

Hence the total Lorentz force due to the own space charge<sup>6</sup> of the bunch decays with  $1/\gamma$  so that the increase of the bunch energy leads to a reduction of the direct space charge force in the transverse plane. For ultra-relativistic energies where  $\gamma$  is of the order of several thousands, the direct space charge forces are practically not an issue for the stability of the bunch in a storage ring.

It is worth mentioning that for bunched beams which are in the focus of this work the direct space charge force perturbs the transverse oscillation of the particles depending on their longitudinal position in the bunch and on the

---

<sup>6</sup>Please remind that  $\mathbf{E}'$  is the space charge field of the bunch in its rest frame.

charge profile of the bunch  $\lambda(z)$ . Thus the betatron oscillation frequencies of the particles inside the bunch are shifted and moreover there is a spread of the betatron frequencies of the incoherent motion of the particles. However the direct space charge force of the bunch is an internal force which is not affecting the coherent oscillation of the bunch i.e. does not change the center of mass motion. As for the beam quality in a synchrotron ring the change of the betatron tune of the incoherent motion of the particles could result in a slow emittance growth of the beam.

### 2.3.2 Wake Fields and Impedances

Another type of unwanted effects on the beam occurs due to the electromagnetic interactions of the self-field of the bunch with the surrounding surfaces of the vacuum chamber. The term vacuum chamber will be used in the following as a general term describing the whole beam vacuum environment including the accelerating cavities. The surface of the vacuum chamber is made of normal conducting or superconducting material which modifies the field of the bunch. Assuming a Perfect Electric Conducting (PEC) surface of the vacuum chamber the electrical boundary conditions impose a perpendicular electric field on the surface. Thus, the field distribution inside the vacuum chamber depends on the geometry of the vacuum chamber (Fig. 2.15 and Fig. 2.16). If the bunch velocity is approximated by the velocity of light  $c$  then its self-field could only exist from the head of the bunch backwards and is usually referred to as a wake field. In the resonant structures of the beam chamber as the RF-cavities, the wake field excited by the bunch remains oscillating for a relatively long time period compared to the bunch length. This is principally shown in Fig. 2.17.

Hence, for subsequent bunches the wake field represents an unwanted electromagnetic force which leads to a loss of energy. Moreover this multi-bunch effect produces a kick in the transverse direction which shifts the betatron tune of the bunch coherent motion accelerating the beam instability and in extreme cases it could even lead to a beam loss.

The electromagnetic (EM) interaction of the beam and its environment is described by wake-functions or impedances. The two-particle model as described e. g. in [Chao 1993] gives an intuitive picture of the wake function  $W(z)$ . As principally displayed in Fig. 2.18 the wake function  $W(z)$  is a function of the relative distance  $z$  between the charge  $q$  which excites the wake fields and the charge  $e$  which receives the action from the wake field. The wake function in one transverse direction  $W(z)_\perp$  is defined through the total accumulated change of the momentum  $\Delta p_\perp$  of the charge  $e$  which is an integral of the acting force  $F_\perp(s, z)$  along some path length  $L$ . For the vertical

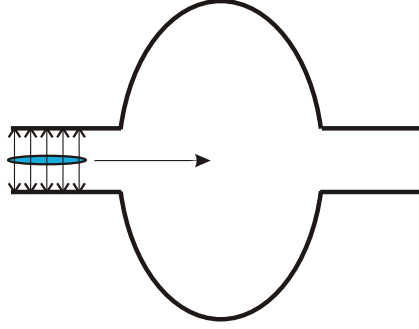


Figure 2.15: The electric field of the bunch satisfies the boundary conditions of the beam pipe.

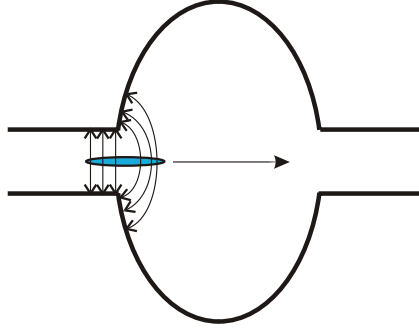


Figure 2.16: The electric field of the bunch is being distorted by satisfying the PEC boundary conditions in the RF cavity.

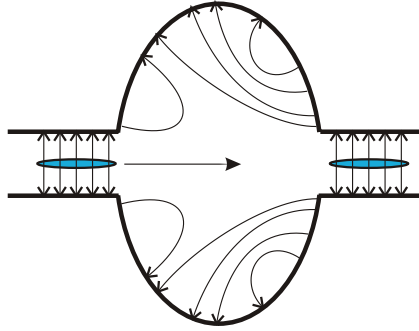


Figure 2.17: After the passage of the bunch its wake field remains oscillating in the resonating structure. The resonance time depends on the quality factor  $Q$  of the resonant structure.

direction the relation is given by

$$\Delta p_y = \int_0^L F_y(s, z) ds = eW_y(z) \Delta y q. \quad (2.71)$$

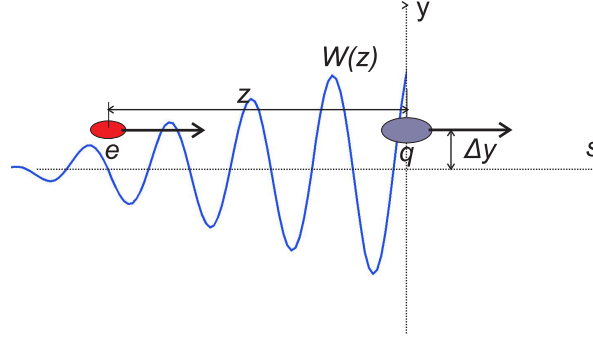


Figure 2.18: The wake function  $W(z)$  experienced by the second particle with charge  $e$  is a function of the distance  $z$  to the preceding charge ( $q$ ) which excites the wake field.

The transverse wake force on the charge  $e$  is proportional to the transverse offset  $\Delta y$  of the exciting charge  $q$ . If the beam pipe could be approximated as PEC then the wake function  $W(z)$  entirely depends on the geometry of the vacuum chamber. The wake functions are used to evaluate the effect of the wake fields on the beam dynamics in time domain. In the frequency domain the corresponding quantity is the impedance which is a Fourier transform of the wake function  $W_{\perp}(z)$

$$Z_{\perp}(\omega) = i \int_{-\infty}^{+\infty} \frac{dz}{c} e^{-i\omega z/c} W_{\perp}(z). \quad (2.72)$$

The impedance defined as such is a line impedance since its unit is  $\Omega/m$ . However, for practical evaluation the impedance is defined by the resonator model:

$$Z_{\perp}(\omega) = \frac{c}{\omega} \frac{R_s}{1 + iQ\left(\frac{\omega_R}{\omega} - \frac{\omega}{\omega_R}\right)}, \quad (2.73)$$

used in the RF cavity design along with the terms as resonant frequency  $\omega_R$ , quality factor  $Q$  (defined by the relation of the stored energy and the power loss):

$$Q = \frac{\omega W_s}{P_v} = \frac{\text{frequency} \times \text{stored energy}}{\text{wall losses}}$$

and the shunt impedance  $R_s$  (the ratio of the squared accelerating voltage and the wall losses of the resonant cavity) [van Rienen 2001]:

$$R_s = \frac{V^2}{P_v} = \frac{\text{voltage}^2}{\text{wall losses}}.$$

In turn, the Fourier transformation of the impedance from (2.73) gives a wake function  $W(z)$  exponentially decaying as a function of the longitudinal

distance  $z$ . In the extreme case of a very good resonator featuring very high  $Q$  the unwanted wake function  $W(z)$  oscillates in the longitudinal direction with frequency  $\omega_R$ , without decaying. The corresponding impedance is called a narrow band impedance. Since it acts on the beam not only locally where the wake field is excited but rather travels backwards in the longitudinal direction it is very unfavorable for the beam stability.

Depending on the range of action of the wake fields they could excite a single or a multi-bunch instability. The single bunch instability is usually caused by short range wake fields while the multi-bunch instability is due to long range wake fields/narrow-band impedances from the preceding bunches.

## 2.4 Electron Clouds and Induced Instabilities

Apart from the self-fields, the beam experiences another type of collective effects from the interaction with other parasitic species of particles which are not belonging to the beam. The interaction of an electron beam with ionized rest gas in the vacuum chamber is such an effect. This study is concentrated on the effects of the interaction of positively charged beams with parasitic electrons gathered in the vacuum chamber.

### 2.4.1 Generation of Electron Clouds

Initially the electrons appear in the beam pipe partly because of vacuum impurity and the ionization of the residual gas but mostly because of the synchrotron radiation of the beam hitting the walls of the vacuum chamber where it causes emission of electrons. The number of photoelectrons produced by each new bunch (Figure 2.19) is a function of the bunch parameters but

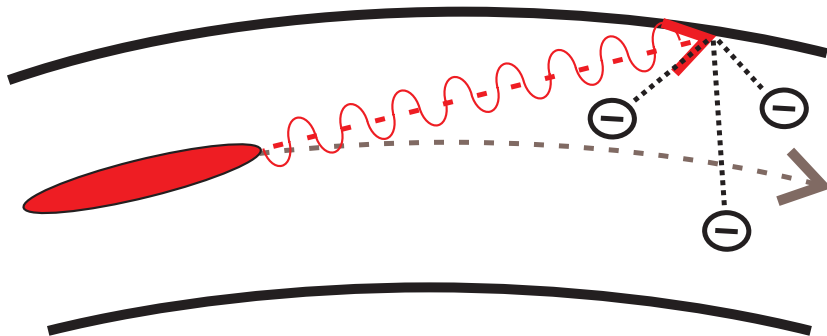


Figure 2.19: Bending the beam by dipole magnets results in synchrotron radiation in the horizontal plane. The radiation directly emits electrons within a  $1/\gamma$  angle from the point where it impinges.

also a function of the material properties, the conditioning and the geometry of the chamber. Therefore the dipole regions of a storage ring, where most of the photoelectrons emerge, have a special design in order to reduce the number of photoelectrons (see Figure 2.20). After an initial photoelectron



Figure 2.20: Principal view of a cross section of the vacuum chamber with an antechamber, in a dipole (right) and in a wiggler magnet (left). The red spot in the middle of the vacuum chamber represents the beam.

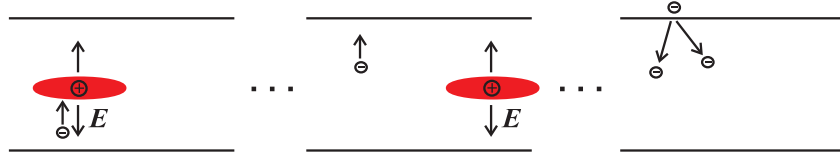


Figure 2.21: Principle of the generation of true secondary electrons from the vacuum chamber walls.

concentration is in place it is attracted in the transversal direction by the passing high-energetic beam. Accelerated by the transverse electric force of the passing beam the electrons reach energies which enable them to produce new electrons when hitting the conducting wall of the vacuum chamber. Those electrons are called secondary electrons. The process is principally shown in Figure 2.21. One incident electron could emit several secondary electrons if the surface property "secondary emission yield" (SEY) is bigger than one. The SEY  $\delta_{SE}(E)$  is a material property which is also a function of the energy  $E$  of the incident electron analytically modelled by M. Furman [Furman 1998] as:

$$\delta_{SE}(E) = \delta_{\max} \frac{s(E/E_{\max})}{s - 1 + (E/E_{\max})^s}. \quad (2.74)$$

The material parameters  $\delta_{\max}$ ,  $E_{\max}$  and  $s$  also depend on the angle at which the incident electron hits the wall of the vacuum chamber. The number of secondary electrons after a very short while prevails in the overall electron concentration as the secondary electrons, accelerated by the passing bunch, produce again new secondaries. In a very unfavorable case where the time which the electrons need to reach the surface of the chamber in transverse direction is equal to the intra-bunch time spacing it may come to a resonant behavior and an exponential growth of the number of electrons. By such a mechanism the electron concentration in the beam chamber grows until

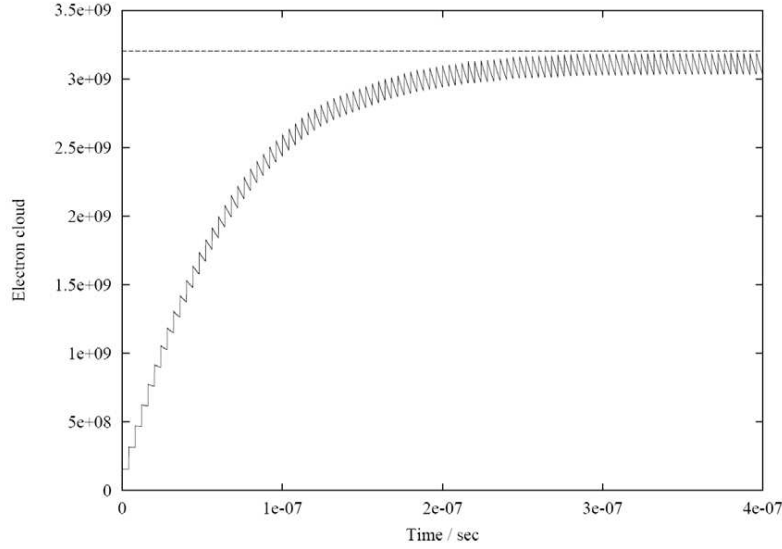


Figure 2.22: Saturation of the electron density in the vacuum chamber. Simulation with the e-cloud build-up code ECLOUD 2.3, courtesy of R. Wanzenberg.

a certain dynamical saturation density has been established. The electron density saturates due to the own repelling space charge forces of the electrons in the cloud. Figure 2.22 results from the simulation of the electron cloud (e-cloud) build-up with the ECLOUD 2.3 code [Zimmermann 2003] by R. Wanzenberg [Wanzenberg 2004]. It represents the development of the number of electrons in the vacuum chamber while a train of many bunches with total current of 200 mA and a small bunch spacing of only 4 ns is passing through. Since the beam is bunched, the attractive force for the electrons is of periodical appearance and the next bunch produces additional primary electrons which explains the ripple of the curve in Figure 2.22. After a passage of one bunch the number of electrons in the proximity of the beam trajectory starts to decay until the next bunch arrives. The dynamic equilibrium density is reached after some 100 bunches passed through the e-cloud. Hence the total number of electrons forming the e-cloud depends on surface properties - as the source of electrons, and on the beam parameters - as the beam provides a strong focusing force acting on the electrons. Therefore the time gap between the bunches in the train is a very important parameter for the e-cloud density. Finally, the e-cloud density in the vacuum chamber is an interplay of many elements: vacuum pressure, geometry and size of the vacuum chamber, the material and the conditioning of the vacuum chamber walls and the corresponding SEY, bunch intensity and dimensions, the beam filling scheme but also the beam loss rate and the photoelectron yield. Typical e-cloud



densities are between  $10^{10}$  and  $10^{13}$  electrons/m<sup>3</sup>. Two computer programs are mainly used for the simulation of the build-up and evolution of the e-clouds: POSINST [Furman 2002] and ECLOUD [Zimmermann 2003]. Recently analytical approaches ([Demma 2007], [Petracca 2011]) to parameterize the bunch-to-bunch evolution of the e-cloud line density were presented as an alternative to the simulation codes.

### 2.4.2 Electron Cloud Effects

The beam and the e-cloud interact through electromagnetic forces originating from both charge distributions enclosed in a conducting beam pipe. The interaction with electron clouds affects the beam quality, the stability and finally its life-time. Further, the presence of e-clouds in the vacuum chamber is also affecting the beam diagnostic systems, the cryogenic system and certainly the vacuum quality. The radiation from the beam-gas scattering could even give some undesirable background to the experiments in collider machines. The

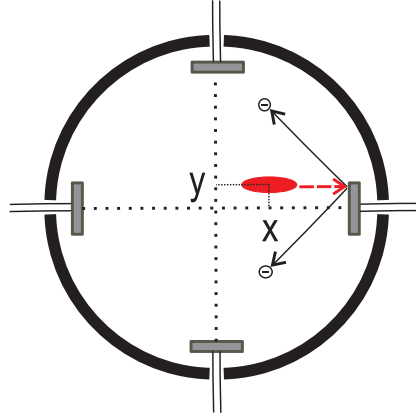


Figure 2.23: Principle sketch of pickup electrodes of a beam positioning monitor.

beam positioning monitors (BPM) in an arc of a synchrotron ring are affected by the synchrotron light. As shown in Figure 2.23, one of the electrodes of the BPM may become a source of photoelectrons whereas the other three electrodes register the electron current. Those electron currents, which may be amplified if the beam induces multipacting, represent a noise for the beam diagnostics and need to be treated by further electronic processing of the BPM pickup signals.

Another big concern for the accelerator operation is the heat load from the electrons deposited by hitting the beam screen, as shown for the Large Hadron Collider (LHC) in Figure 2.24. The beam screen shields the cold superconducting parts from the synchrotron radiation of the beam and for that

purpose needs to be cooled with a complex and expensive cryogenic system. Hence the cooling capacity needs to accommodate the thermal energy from the e-cloud as well. Thereby the additional cooling rapidly raises the cost of the accelerator operation. Moreover in an extreme case, due to constructive limitations, the capacity of the cryogenic system may not be enough to dissipate the extra heat load in the vacuum chamber originating from the e-cloud. The consequence of this might be a quenching of the superconducting magnets and a stop of the storage ring operation.

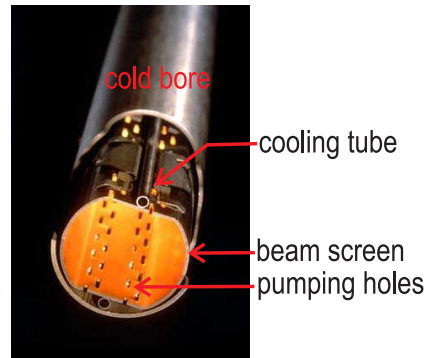


Figure 2.24: Cross-section of LHC prototype beam pipes showing the beam screens, Source: CERN Document Server [Loiez 1997].

#### 2.4.2.1 Beam Instabilities due to Electron Clouds

Generally the collective effects on a bunched beam can be described as coherent or incoherent effects. The coherent effects affect all the particles of the bunch more or less equally. If all the particles of the bunch receive an equal transversal kick, due to the interaction with the e-cloud, their betatron oscillation frequency changes or shifts in the same manner so that the effect on the beam is referred to as a coherent transverse tune shift. Observations ([Ohmi 1995], [Ohmi 2000a], [Ohmi 2001c]) show that above a certain threshold value of the e-cloud density, the beam starts to behave resonantly due to the excitation from the cloud and it becomes coherently unstable. Such a coherent instability usually leads to a very fast beam loss. The instability is registered by monitoring the centroid bunch motion in the transverse plane, characterized by fast growing amplitudes and a coherent tune shift in the same transverse direction. However, the beam could also become unstable due to the interaction with e-cloud densities below the threshold which triggers fast coherent beam instability. Thereby the particles in the bunch are differently affected by the e-cloud which results in a spread of their betatron frequencies. Hence the effect is called incoherent. The diffusion of the particles in space

and in phase is manifested through a relatively slow but steady emittance growth and an incoherent tune shift of the single bunches. Eventually a slow beam loss could be registered by measuring the number of the particles in each bunch of the train. The bunches in the back of the train loose more particles than the ones in the beginning of the train which is reasonable since the density of the e-cloud rises along the train as shown in Figure 2.22. Fortunately, the incoherent motion of the particles is damped by the synchrotron radiation of the particles in the bunch. However, in many modern synchrotron machines, the synchrotron period is relatively long so that the incoherent instability may still lead to a significant deterioration of the beam quality. In turn, loosing the parameters needed for the respective experiments shortens the beam life time in the machine.

Both, the coherent and the incoherent effects can be either transverse or longitudinal. The collective effects arising from the interaction of a positively charged bunched beam with an e-cloud are affecting the beam mainly in the transverse plane. Depending on the beam parameter the effects on the beam due to the interaction with the e-cloud could be of a single- and/or multi-bunch nature.

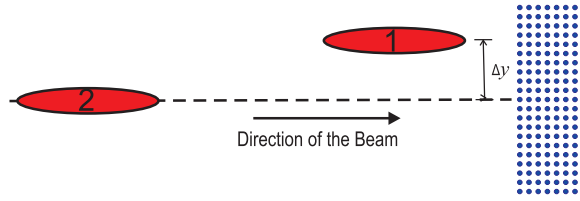


Figure 2.25: The displaced bunch perturbs the electron distribution.

Suppose a bunch with some transverse displacement (relative to the other bunches in the train) is progressing through an initially homogeneous electron cloud as principally shown in Figure 2.25. The electron distribution will be perturbed in such a manner that it is imposing a dipole force on the following bunches. If the electron distribution cannot recover from the distortion after the interaction with the preceding bunch and since it acts back on the successive bunch (see Figure 2.26) it consequently represents a case of multi-bunch effect. Such a multi-bunch instability depends on the accelerator operation mode, i.e. the charge and the time spacing between the consecutive bunches but also on the number of bunches in a train and the time spacing between them. The multi-bunch instability due to an e-cloud is analogous to a narrow band resonator response on the wakefield of a bunch.

A single bunch effect occurs due to the interaction of the bunch with the e-cloud whereby the head part of the bunch perturbs the e-cloud which then acts on the rear parts of the bunch. The head and the tail motion of a single

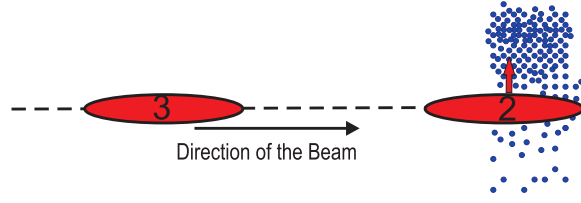


Figure 2.26: The following bunches (2 and 3) receive a dipole kick from the perturbed electron cloud - a mechanism of multi-bunch instability.

bunch are coupled by the induced distortion of the electron cloud distribution. Figures 2.27 and 2.28 qualitatively explain the mechanism of the head-tail instability where the transverse beam size is blown up due to the deflection of the tail part of the bunch. The rate of the head-tail instability depends on the charge per bunch and its length, but most of all on the electron cloud density which again is dependent on the beam filling pattern i.e. the intra-bunch spacing.

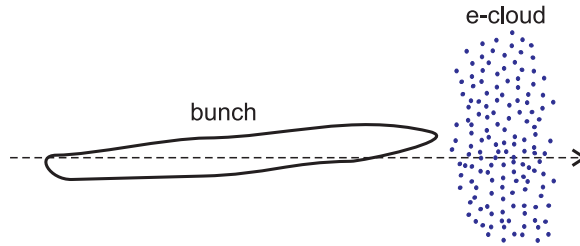


Figure 2.27: Head-tail instability: the head of the bunch changes the electron cloud centroid position in the transverse plane.

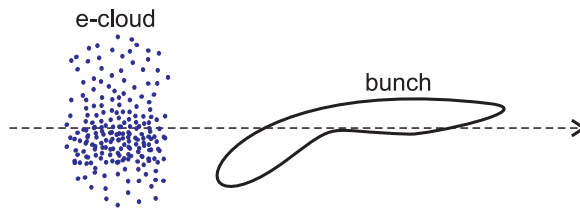


Figure 2.28: The kick on the tail parts of the bunch results in a beam size growth and sidebands in the betatron frequency as the effect is incoherent.

Storage rings built for very high luminosity or brightness are characterized by large aspect ratios in the transverse emittances. Thus the bunches are usually very flat which results in higher electrical fields of the bunch in vertical direction. These strong vertical fields accelerate the electrons in vertical direction so that the electron cloud effect is more pronounced in the vertical than in the horizontal bunch motion. A cure for trapping the electrons

and slowing down the rate of the head-tail instability is the application of solenoidal fields. Also the single bunch instability due to e-clouds is analogous to a broadband response of a resonating structure on the excitation of a bunch. A broadband impedance model for the electron cloud was proposed in [Ohmi 2001c]. However, the analogy is restricted only on the broadband type of response. The computation and the prediction of which is much more difficult for the interaction of beam and e-cloud. The e-cloud as a environment of the beam changes rapidly during the bunch passage whereas the vacuum chamber geometry is a rigid environment which does not change over time. The goal of this work is to simulate in detail the interaction of a single bunch with an electron cloud and with it to help the estimation of the effects on the bunch due to the interaction with e-clouds.

## 2.5 Summary of the Chapter

As briefly described in this chapter apart from the guiding magnetic fields a number of collective effects act on the beam particles in a storage ring. Some collective effects as the beam's own wake fields, due to the vacuum chamber geometry and the resistive walls, can be described by wake functions or impedances. Hence their influence on the bunch could be evaluated by tracking the bunch through the beam optics while at each turn a kick proportional to the pre-computed wake function is applied on the bunch. From a computational point of view this is a very cheap and fast simulation. On the other hand, the influence of other collective effects, as the own space charge fields or the influence of other parasitic charged particles in the vacuum chamber, can not be adequately described in terms of the classical wake functions as briefly introduced in 2.3.2 ([Rumolo 2002] and [Ohmi 2001c]). The interaction of the bunch particles with their own or the space charge fields of other parasitic particle species as ions or electron clouds has to be simulated over a certain time to evaluate the influence of those collective effects on the bunch motion. Such a simulation requires a computation of the space charge fields and is much more expensive in terms of computational time, compared with the bunch tracking through the linear optics and thereby applying a pre-computed wake-kick.



# Modelling and Implementation of Particle Tracking

---

## Contents

---

<b>3.1</b>	<b>Electrostatic Macro-Particle Model . . . . .</b>	<b>42</b>
<b>3.2</b>	<b>Tracking Cycle . . . . .</b>	<b>44</b>
<b>3.3</b>	<b>Charge Weighting . . . . .</b>	<b>47</b>
<b>3.4</b>	<b>Computation of 3D Space Charge Fields of Charged Particle Distributions . . . . .</b>	<b>49</b>
3.4.1	Discretization of the Poisson Equation . . . . .	50
3.4.2	Discrete Poisson Equation in a Domain with Elliptical Cross-Section . . . . .	53
3.4.3	Space Charge Field Computation for Different Boundary Conditions . . . . .	57
3.4.3.1	Conducting boundary conditions on beam pipes with elliptical cross section . . . . .	58
3.4.4	Computation of the electric field for relativistic bunches	62
3.4.5	Comparison of the transverse field with analytical Bassetti-Erskine expression . . . . .	62
<b>3.5</b>	<b>Interpolation of the Electrical Field . . . . .</b>	<b>67</b>
<b>3.6</b>	<b>Integration of the Equations of Motion . . . . .</b>	<b>70</b>
3.6.1	Tracking of Relativistic Particles . . . . .	72
3.6.2	Comparison of MOEVE PIC Tracking with other PIC Programs . . . . .	76

---

The program MOEVE PIC Tracking was initially created during this work to simulate the interaction between the particles of a relativistic bunch and electron clouds. The particle tracking routines evolved around the Multi-grid based 3D Poisson solver MOEVE [Pöplau 2005] originally developed by Gisela Pöplau. For the purposes of this work the 3D Poisson solver MOEVE

was complemented with space-charge routines which implement PEC boundaries describing a vacuum chamber with elliptical cross section. In MOEVE PIC Tracking the particle distribution is discretized in space and its evolution under the influence of the guiding and collective fields is simulated in time. The source of those collective fields are the bunch particles themselves or other parasitic particles. Thereby the space charge fields of the particle distribution are computed and then the resulting forces are applied back on each particle. Thus the particle distribution evolves over time under the influence of the collective field forces. The time discretization for the simulation is determined by the mobility of the particles involved. Finally the parameters for the interaction simulation depend on the type of effects on the beam to be examined (the collective fields of the e-cloud and the ions are changing on different time scale simply because of the different particle mass which determines the dynamics of the distribution).

In any case, the computation of the space charge force for each particle is based on a superposition of the forces from all other particles. Considering the fact that a typical bunch can be represented by several millions of particles the direct particle-particle method would be computationally inefficient since it scales by  $N^2$ , where  $N$  is the number of particles. Therefore, a three dimensional (3D) mesh is defined over the particle distribution in the so-called "particle-mesh" or "particle-in-cell" (PIC) model for iterative computation of the forces. The method is well established for the low pressure plasma simulations and in depth described in the book of Birdsall [Birdsall 1991]. Thereby the charge densities are deposited at the grid points by weighting the charges from the particles positioned in the proximity of each grid point. Next, for example in the PIC electrostatic observation, the discretized Poisson equation is solved on the grid using the finite difference method. Once the electric field between the grid points is computed it is interpolated at the position of the particles. The new position of the particles is then obtained by the time integration of the Lorentz equation of motion with all the fields acting on the particle taken into account. The external magnetic forces are modelled by mapping or by an analytical description as functions in space and time.

### 3.1 Electrostatic Macro-Particle Model

The number of particles in a bunch, which dynamics should be simulated, is very large i.e. in the order of  $10^{10} - 10^{12}$  unit particles. The storage requirement and the successive update of the position of such a number of particles limits the performance of the simulation even with the present computational resources. Therefore, in the numerical model their number is reduced typi-



cally to the order of  $10^6 - 10^7$  particles also known as macro-particles. They represent multiple unit particles bearing the multiple of the unit charge and weight. Since the ratio between the charge  $Q$  and the mass  $M$  of the macro-particle remains the same as for the elementary particle ( $\frac{Q}{M} = \frac{q}{m_0}$ ), their dynamic behavior in electromagnetic fields will be the same as that of the elementary particle. The approximation made by placing de facto many

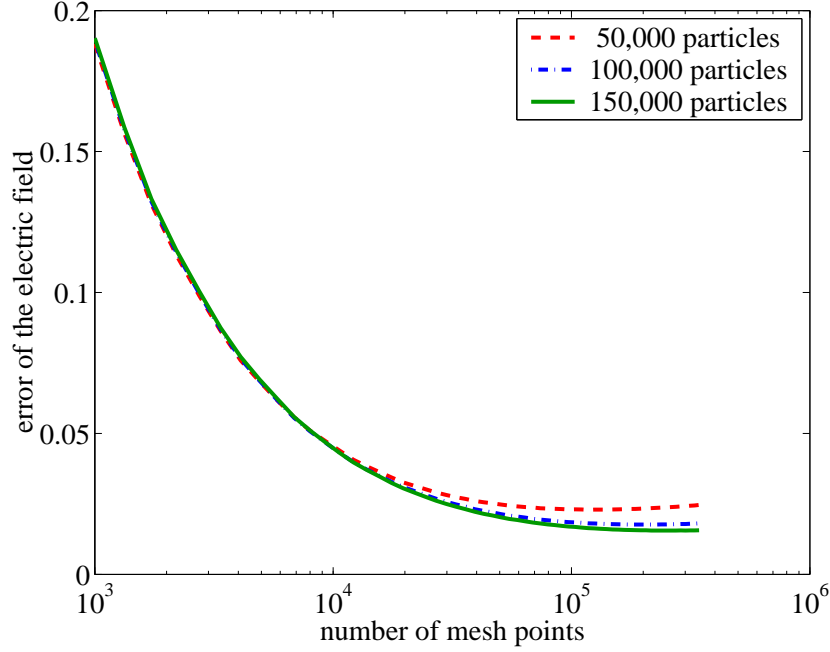


Figure 3.1: Relative error of the electric field from uniformly distributed macro-particles in a sphere with constant charge. Comparison of different number of macro-particles on an equidistant mesh [Pöplau 2005].

unit particles on the same spot does not have considerable influence on the accuracy of the space charge fields computed later. Numerical experiments with even a smaller number of macro-particles (order of magnitude  $10^5$ ) show that for uniform (Figure 3.1) and Gaussian (Figure 3.2) particle distributions the deviation of the field from the analytically computed values for different number of macro-particles are insignificant. Figures 3.1 and 3.2 reveal one important parameter of the PIC space charge field computation namely that the accuracy of the computed field from the particle distribution depends on the number of mesh cells discretizing the space. Generally, the accuracy is improved by increasing the number of mesh cells. In MOEVE PIC Tracking the particles and the vacuum chamber are defined in a 3D Cartesian mesh. Its resolution should be fine enough to resolve the particle distribution in a reasonable number of grid cells, thus for practical computations a non-equidistant

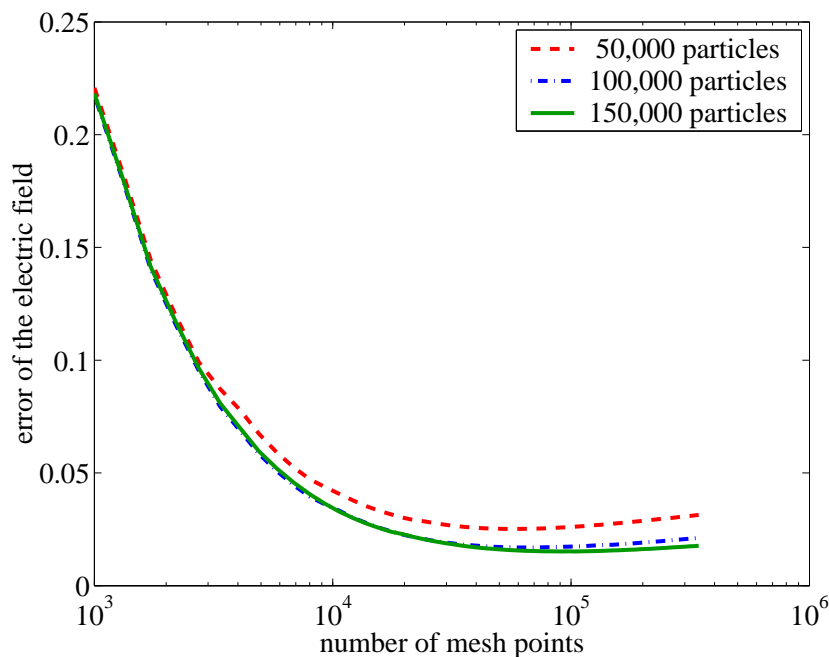


Figure 3.2: Relative error of the electric field from Gaussian distributed macro-particles in a sphere with constant charge. Comparison of different number of macro-particles on a non-equidistant mesh [Pöplau 2005].

is indispensable.

Since in storage rings of our interest the particles of the bunch are highly relativistic (i.e.  $> 1\text{GeV}$ ) it could be assumed that they don't change their relative position to each other in the direction of acceleration (longitudinal). Thus, those point charges moving in the laboratory frame with constant velocity (approaching the velocity of light) are seen as stationary in the bunch rest frame. In the rest frame, the electric field of each particle expands radially from the point charge, the Coulomb law holds and the own space charge field can be solved as an electrostatic problem.

## 3.2 Tracking Cycle

The tracking cycle for plasma simulations described in [Birdsall 1991] is slightly modified for the simulation of the dynamics of relativistic bunched particles. The definition of the initial macro-particle distribution is written in an ASCII file which holds the space coordinates of each particle as well as their impulse components and their mass-charge ratio  $(x, y, z, p_x, p_y, p_z, Q/M)$ . The bunch is usually represented by a Gaussian distribution of particles in space but the program is able to process any other given distribution of particles.

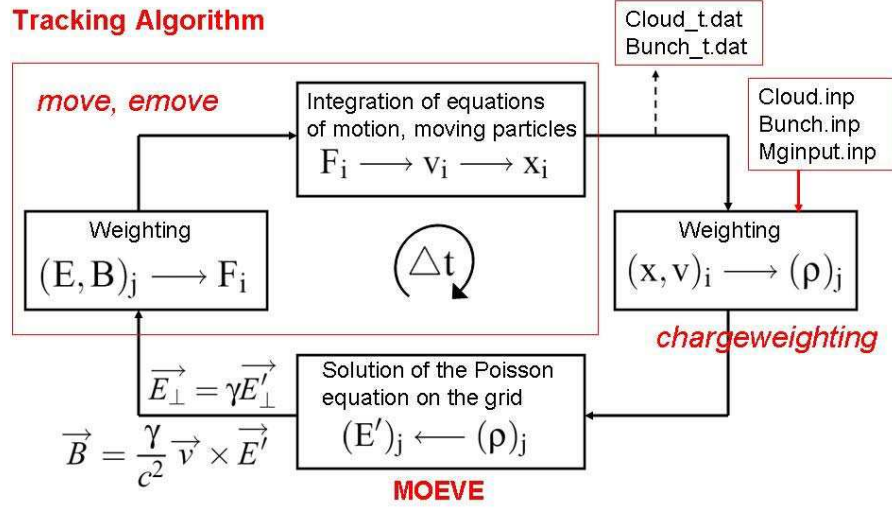


Figure 3.3: Cycle of the tracking algorithm implemented in MOEVE PIC Tracking.

The position of the particles is defined relative to one leading particle with space coordinates  $(0, 0, 0)$ . The leading particle bears also the defined impulse of the bunch thus it is defined by  $(0, 0, 0, 0, 0, p_z, Q/M)$ . The momenta of the other bunch particles are distributed around the momentum of the leading particle according to the defined energy spread of the bunch.

The primary goal of MOEVE PIC Tracking is to simulate the interaction of the bunch with electron clouds. In such a case the distribution of the electrons written in the same format as the bunch distribution has to be loaded as well. Typically the initial distribution of the electrons in a drift section is homogeneously filling the beam tube. Currently the distribution is generated by a routine called "generator.exe" from the program package ASTRA [Flöttmann 2000] written at DESY mainly for Free Electron Laser (FEL) machine simulations. The generated particle distributions are bound in a vacuum space by a certain geometry of Perfect Electrical Conducting (PEC) beam pipe. In MOEVE PIC Tracking we offer the possibility to define a beam pipe with rectangular or elliptical transverse cross-section. The elliptical cross-section is defined by the lengths of the ellipse half-axes  $a$  and  $b$  as shown in Figure 3.4. The beam pipe modelled as PEC implicitly incorporates the influence of the mirror charges on the bunch. After the beam pipe dimensions are defined and the particle distribution is read from the program, the volume

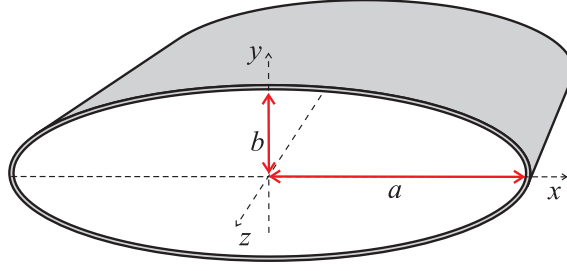


Figure 3.4: Elliptical cross-section of a beam pipe.

has to be discretized. MOEVE PIC Tracking uses a 3D Cartesian grid as defined in the input file presented in the Appendix B. The user could define the grid lines in each direction arbitrarily and non-equidistantly in order to allow denser meshing at the position of the particle distribution and a coarser meshing elsewhere.

In order to compute the space charge fields of the particles scattered between the grid<sup>1</sup> lines it is necessary to deposit the charge of the particles on the grid points. Consequently the discrete charge density  $\varrho_j$  is computed from the charge on the grid points. This is done by a charge weighting routine at the beginning of the simulation and after each time step in which the particles change their position.

The particle tracking simulation starts at a time  $t = 0$  and is performed until the defined end time  $t_{end}$  is reached. The time step  $dt$  in which the equations of motion of the particles are integrated is also predefined according to the particle mass and charge ratio. Usually for positron bunches and electron clouds the time step  $dt$  is of picosecond range.

The computation of the space charge forces from the spatially distributed charges succeeds by computing first the electrical scalar potential  $\varphi$  from the Poisson equation [van Rienen 2001, Page 23]:

$$-\Delta\varphi = \frac{\varrho}{\varepsilon_0}. \quad (3.1)$$

Since we assume a vacuum in the beam pipe,  $\varepsilon_0$  is the dielectric constant of vacuum and  $\varrho$  the charge density. The Poisson equation is discretized and solved for the nodes of the grid.

Applying the gradient operator on the computed discrete scalar potential values  $\varphi$ , yields the field components  $\mathbf{E}'$  for each grid point  $m$ . After the relativistic transformation from the bunch rest frame back into the laboratory frame the program yields the components of  $\mathbf{E}_m$  but also components of the

<sup>1</sup>In the further text the terms grid or mesh are used as synonym and describe the spatial discretization set upon the particle distribution and the beam pipe.

magnetic flux density  $B_m$  produced by the beam at a discrete grid point  $m$ . The discrete field components are then interpolated on the position of each particle and the particle trajectories are integrated with the time step  $dt$ . The single steps of the tracking cycle are explained in detail in following sections.

### 3.3 Charge Weighting

In order to solve the discretized Poisson equation, the charge of the spatially distributed particles should be allocated on the grid nodes. The allocation of the charge on the grid points could be of arbitrary complexity. In MOEVE PIC Tracking we use the first order weighting for the particle charge in the three dimensional space. Figure 3.5 clarifies the charge weighting for two dimensions (2D). It shows a part of a 2D grid and a single particle (colored

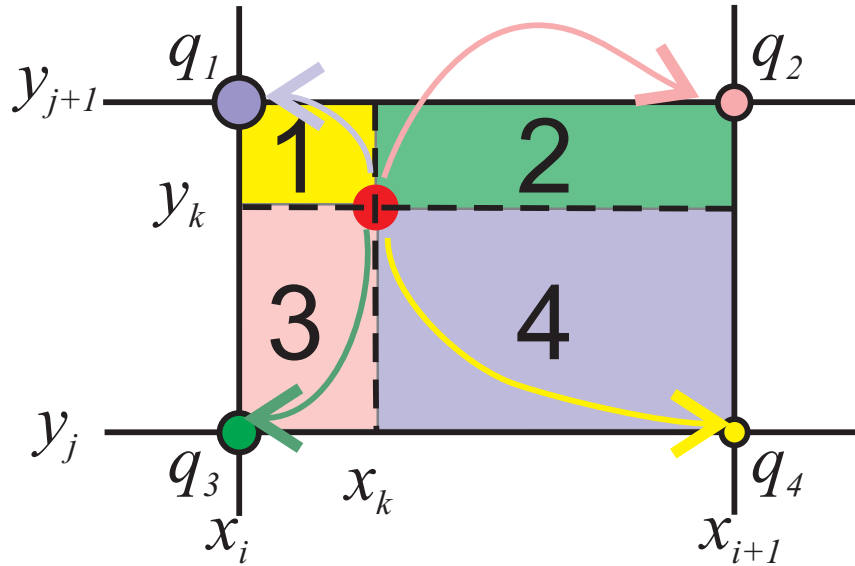


Figure 3.5: 1<sup>st</sup> order charge weighting in 2D.

red) inside one cell. The charge of the  $k$ -th particle with coordinates  $(x_k, y_k)$  is distributed among the nodes of the grid cell according to its position inside the cell. The cell is defined by the horizontal  $y_j$  and  $y_{j+1}$  and the vertical  $x_i$  and  $x_{i+1}$  grid lines. Naturally, since the grid node belonging to subsection 1 of the grid cell in which the particle is located, is the nearest node to the particle it receives the largest portion  $q_1$  of the charge  $q$ . The smallest part of the charge  $q$  should receive the node belonging to subsection 4. The part  $q_4$  of the charge  $q$  is computed by weighting the charge  $q$  with the ratio of the area of the opposite section 1 and the total area of the grid cell. Hence, the

total charge  $q$  of the particle is distributed among the nodes as:

$$\begin{aligned}
 q_1 &= q \frac{(x_{i+1} - x_k)(y_k - y_j)}{(x_{i+1} - x_i)(y_{j+1} - y_j)}, \\
 q_2 &= q \frac{(x_k - x_i)(y_k - y_j)}{(x_{i+1} - x_i)(y_{j+1} - y_j)}, \\
 q_3 &= q \frac{(x_{i+1} - x_k)(y_{j+1} - y_k)}{(x_{i+1} - x_i)(y_{j+1} - y_j)}, \\
 q_4 &= q \frac{(x_k - x_i)(y_{j+1} - y_k)}{(x_{i+1} - x_i)(y_{j+1} - y_j)}.
 \end{aligned} \tag{3.2}$$

Higher-order weighting by using smooth shape functions with quadratic or cubic splines further reduces the noise of the weighted particle density, however at the cost of much higher computational effort. Depending on the grid density

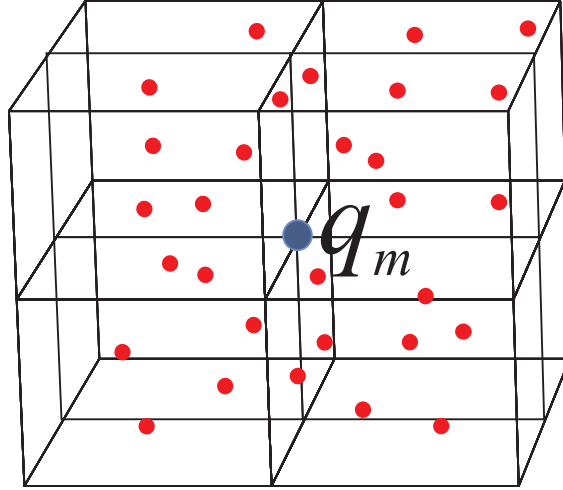


Figure 3.6: All the particles in the eight neighboring cells are contributing to the charge of the node in the center.

and the particle distribution, a number of grid cells contain more than one particle inside, so that the charge  $q_m$  in the node  $m$  is a sum of the partial charges of all the particles in the eight adjacent cells as shown in Figure 3.6.

Finally, after allocating the charge of all the particles on the grid nodes, the spatial charge density  $\varrho$  could be computed by dividing the charge on each node with the corresponding cell volume. Thus, the right hand side of the discretized Poisson equation at grid node  $m$  reads as:

$$\frac{\varrho_m}{\varepsilon_0} = \frac{q_m}{(x_{i+1} - x_i)(y_{j+1} - y_j)(z_{k+1} - z_k)\varepsilon_0}. \tag{3.3}$$

### 3.4 Computation of 3D Space Charge Fields of Charged Particle Distributions

The electrostatic field is defined as a gradient of the electric scalar potential:

$$E = -\text{grad}\varphi. \quad (3.4)$$

As previously mentioned, the scalar potential has to be computed from Poisson's equation (3.1), which for a numerical solution has to be discretized on a predefined Cartesian grid. Figure 3.7 shows an example of three dimensional

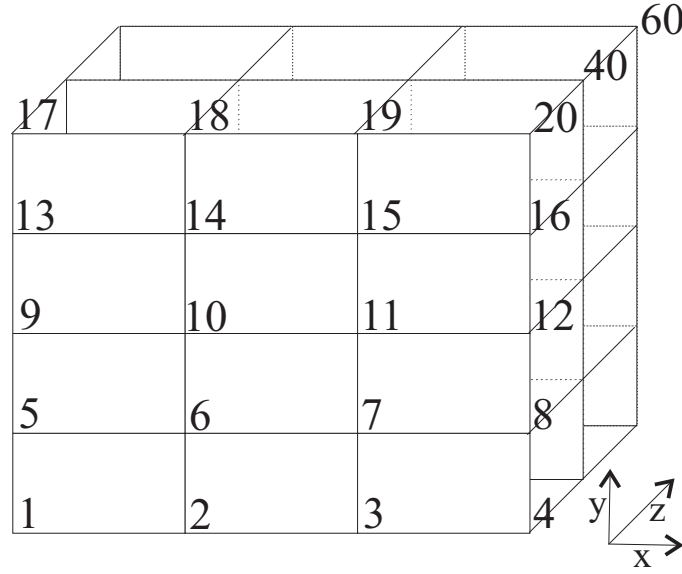


Figure 3.7: Cartesian grid with  $N_x = 4$ ,  $N_y = 5$  and  $N_z = 3$ .

Cartesian grid. The grid is defined by a number of grid planes  $N_x$ ,  $N_y$  and  $N_z$  in each coordinate direction  $x$ ,  $y$  and  $z$ , respectively. The  $N_x$  planes for example in  $x$ -direction are defined by the coordinate value  $x_i$  where  $i = 1, \dots, N_x$ . Planes in  $y$ - and  $z$ -direction are defined by  $y_j$  and  $z_k$  correspondingly, where  $j = 1, \dots, N_y$  and  $k = 1, \dots, N_z$ . The grid nodes are defined at the intersection points of three grid planes, hence each node is clearly defined by the indexing of the intersecting planes  $(i, j, k)$ , which give the coordinates of the node  $(x_i, y_j, z_k)$ . However, for practical reasons the enumeration of the grid nodes is in lexicographic order, i.e. the  $(i, j, k)$  node is numbered as

$$m = i + (j - 1)N_x + (k - 1)N_xN_y.$$

As shown in Figure 3.7 the node  $m = 1$  is given by  $(1, 1, 1)$  and the total number of grid nodes is  $N_p = N_xN_yN_z = 4 \cdot 5 \cdot 3 = 60$  in the depicted example.

$N_p$  is also the maximal possible number of unknowns which determines the size of the system of linear equations. The system of linear equations emerges from the discretization of the Poisson equation for each grid point.

### 3.4.1 Discretization of the Poisson Equation

Currently, in MOEVE PIC Tracking the Poisson equation is numerically solved in two different types of domains. One is a rectangular box domain  $\Gamma = [x_1, x_N] \times [y_1, y_N] \times [z_1, z_N]$  bounded in transverse direction on  $\partial\Gamma_1$  with Dirichlet boundary conditions (b.c.) and *open* boundary conditions in axial direction on  $\partial\Gamma_2$ :

$$\begin{aligned} -\Delta\varphi &= \frac{\rho}{\varepsilon_0} & \text{in } \Gamma \subset \mathbb{R}^3, \\ \varphi &= g & \text{on } \partial\Gamma_1, \\ \frac{\partial\varphi}{\partial n} + \frac{1}{r}\varphi &= 0 & \text{on } \partial\Gamma_2, \end{aligned} \tag{3.5}$$

where the boundary  $\partial\Gamma$  of the domain is  $\partial\Gamma = \partial\Gamma_1 \cup \partial\Gamma_2$ . In practise the Dirichlet b.c. are applied by assigning a certain value for the electric scalar potential  $\varphi = g$  on the boundary  $\partial\Gamma_1$ . Evenmore the transverse boundary  $\partial\Gamma_1$  could be sub-divided in parts with different potentials assigned, for example if some clearing electrodes with constant potential need to be placed in the beam pipe.

The second type of domain  $\Omega$  is a cylindrical structure with an elliptical cross-section as shown in Figure 3.4 and a certain length in axial direction  $L = z_N - z_1$ . The Poisson equation (3.1) is considered with the following boundary conditions:

$$\begin{aligned} -\Delta\varphi &= \frac{\rho}{\varepsilon_0} & \text{in } \Omega \subset \mathbb{R}^3, \\ \varphi &= 0 & \text{on } \partial\Omega_1, \\ \frac{\partial\varphi}{\partial n} + \frac{1}{r}\varphi &= 0 & \text{on } \partial\Omega_2, \end{aligned} \tag{3.6}$$

where  $\partial\Omega_1$  is the side surface area of the elliptic cylinder whose shape is given by

$$\frac{x^2}{a^2} + \frac{y^2}{b^2} = 1$$

and  $\partial\Omega_2$  designates the two elliptical bases of the cylinder satisfying

$$\frac{x^2}{a^2} + \frac{y^2}{b^2} \leq 1.$$

The elliptical bases are perpendicular to the  $z$ -axis positioned at  $z = z_1$  and  $z = z_N$ . The boundary condition  $\varphi = 0$  on  $\partial\Omega_1$  means that the surface of the



beam pipe is approximated as an ideal electrical conductor. The open boundary conditions in  $z$ -direction approximate an indefinitely long cylinder within the finite computational domain. The cylindrical computational domain  $\Omega$  as shown in Figure 3.8 is embedded in the discretized rectangular volume  $\Gamma$  defined in (3.5).

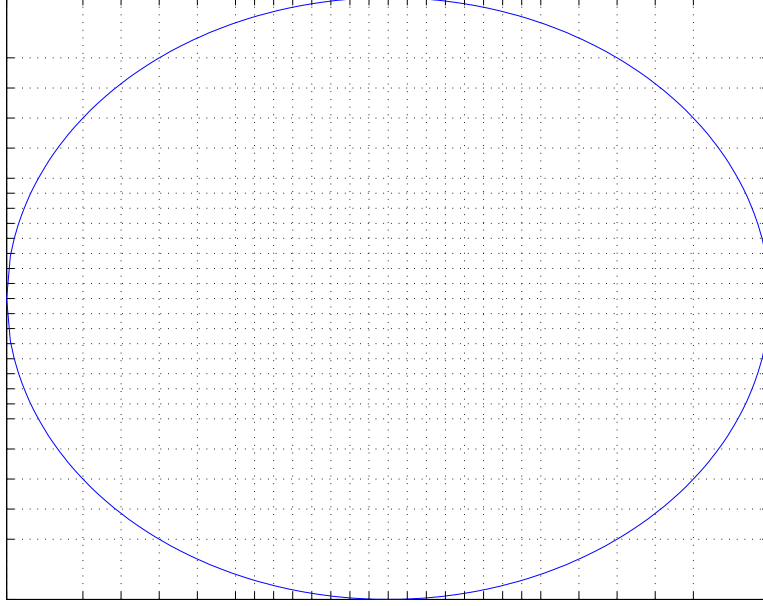


Figure 3.8: Elliptic cross-section of the domain  $\Omega$  embedded in the discretized domain  $\Gamma$ .

Following the notations for the Cartesian grid given in Figure 3.7 the box  $\Gamma$  is discretized along the  $x$ -,  $y$ - and  $z$ -axis in  $N_x - 1$ ,  $N_y - 1$  and  $N_z - 1$  subintervals, respectively. The subintervals are defined by the discrete grid points in the respective direction, in  $x$ -direction the subintervals are defined as:

$$h_{x,1} = x_2 - x_1, \quad h_{x,2} = x_3 - x_2, \dots, \quad h_{x,N_x-1} = x_N - x_{N-1},$$

and the length of the domain in  $x$ -direction is  $x_N - x_1 = \sum_{i=1}^{N_x-1} h_{x,i}$ . Analogously, the  $y$ - and  $z$ -coordinate are discretized by  $N_y - 1$  and  $N_z - 1$  subintervals.

Further we define the subintervals:

$$\tilde{h}_{x,i} = \begin{cases} \frac{h_{x,i-1} + h_{x,i}}{2}, & i = 2, \dots, N_x - 1 \\ \frac{h_{x,i}}{2}, & i = 1 \\ \frac{h_{x,i-1}}{2}, & i = N_x \end{cases} \quad (3.7)$$

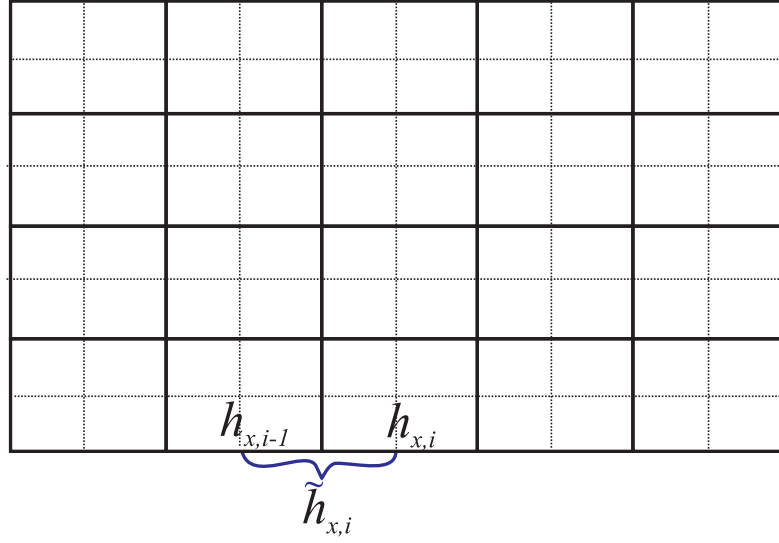


Figure 3.9: Grid subintervals  $h_{x,i-1}$ ,  $h_{x,i}$  and the corresponding dual grid subinterval  $\tilde{h}_{x,i}$ .

( $\tilde{h}_{y,j}$ ,  $j = 1, \dots, N_y$  and  $\tilde{h}_{z,k}$ ,  $k = 1, \dots, N_z$  in the same way) which in Finite Integration Technique (FIT) [Weiland 1977] are known as mesh spacing on the dual grid as show in Figure 3.9.

The sum of  $\varphi(x_{i+1}, y_j, z_k) = \varphi(x_i + h_{x,i}, y_j, z_k)$  and  $\varphi(x_{i-1}) = \varphi(x_i - h_{x,i-1}, y_j, z_k)$  developed as a Taylor series, up to the second order, yields the discretization of the second order derivative with second order finite differences. In the general case of a non-equidistant mesh in  $x$ -direction the finite differences equation reads as:

$$\frac{\partial^2 \varphi(x_i, y_j, z_k)}{\partial x^2} \approx \frac{\varphi(x_{i-1}, y_j, z_k)}{\tilde{h}_{x,i} h_{x,i-1}} - \frac{2\varphi(x_i, y_j, z_k)}{h_{x,i} h_{x,i-1}} + \frac{\varphi(x_{i+1}, y_j, z_k)}{h_{x,i} \tilde{h}_{x,i}}. \quad (3.8)$$

By adopting the following notation for the grid scalar potential  $\varphi_{i,j,k} = \varphi(x_i, y_j, z_k)$ , the discretization of the Poisson equation with second order finite differences on the above described non-equidistant Cartesian mesh in all three directions leads to the following equation:

$$\begin{aligned} & \tilde{h}_{y,j} \tilde{h}_{z,k} \left( -\frac{1}{h_{x,i-1}} \varphi_{i-1,j,k} + \left( \frac{1}{h_{x,i-1}} + \frac{1}{h_{x,i}} \right) \varphi_{i,j,k} - \frac{1}{h_{x,i}} \varphi_{i+1,j,k} \right) \\ & + \tilde{h}_{x,i} \tilde{h}_{z,k} \left( -\frac{1}{h_{y,j-1}} \varphi_{i,j-1,k} + \left( \frac{1}{h_{y,j-1}} + \frac{1}{h_{y,j}} \right) \varphi_{i,j,k} - \frac{1}{h_{y,i}} \varphi_{i,j+1,k} \right) \\ & + \tilde{h}_{x,i} \tilde{h}_{y,j} \left( -\frac{1}{h_{z,k-1}} \varphi_{i,j,k-1} + \left( \frac{1}{h_{z,k-1}} + \frac{1}{h_{z,k}} \right) \varphi_{i,j,k} - \frac{1}{h_{z,k}} \varphi_{i,j,k+1} \right) \\ & = \tilde{h}_{x,i} \tilde{h}_{y,j} \tilde{h}_{z,k} f_{i,j,k} \end{aligned} \quad (3.9)$$

for any grid point defined by the indices  $i, j$  and  $k$ . On the right-hand side  $f_{i,j,k}$ , as given in (3.3), is a function of the charge  $q_{i,j,k}$  deposited on the

$(i, j, k)$ —node and the dielectric permittivity  $\varepsilon_{i,j,k}$  defined for that node. In fact, writing the discretization star equation (3.9) for all the points in the computational domain  $\Gamma$  or  $\Omega$  yields a system of linear equations with the electric scalar potential  $\varphi$  as unknown vector. The same system of equations is obtained with the application of the Finite Integration Technique.

By using the Kronecker product ' $\otimes$ ' (see e.g. [van Loan 1992]) the system of linear equations for the grid points in the domain  $\Gamma$  can be written in a compact matrix vector notation as:

$$A\varphi = \tilde{H}_z \otimes \tilde{H}_y \otimes \tilde{H}_x f. \quad (3.10)$$

For Dirichlet boundary conditions applied in transversal direction on  $\partial\Gamma = \Gamma_1$  the  $\tilde{H}_x = \tilde{H}_{x,D}$  is defined as

$$\tilde{H}_{x,D} := \text{Diag}(\tilde{h}_{x,2}, \tilde{h}_{x,3}, \dots, \tilde{h}_{x,N_x-1}).$$

The system matrix  $A$  is defined as

$$A = \tilde{H}_z \otimes \tilde{H}_y \otimes A_x + \tilde{H}_z \otimes A_y \otimes \tilde{H}_x + A_z \otimes \tilde{H}_y \otimes \tilde{H}_x. \quad (3.11)$$

where again for Dirichlet boundary conditions  $A_x = A_{x,D}$  where

$$\mathbf{A}_{x,D} := \begin{pmatrix} \left(\frac{1}{h_{x,1}} + \frac{1}{h_{x,2}}\right) & -\frac{1}{h_{x,2}} & & & \\ -\frac{1}{h_{x,2}} & \left(\frac{1}{h_{x,2}} + \frac{1}{h_{x,3}}\right) & -\frac{1}{h_{x,3}} & & \\ & & \ddots & & \\ & & & -\frac{1}{h_{x,N_x-2}} & \left(\frac{1}{h_{x,N_x-2}} + \frac{1}{h_{x,N_x-1}}\right) \end{pmatrix}.$$

The diagonal matrices  $\tilde{H}_y$  and  $\tilde{H}_z$  are defined analogously to  $\tilde{H}_x$  and the finite difference matrices  $\mathbf{A}_y$  and  $\mathbf{A}_z$  analogously to  $\mathbf{A}_x$ . Note the different dimensions of the matrices corresponding to the number of mesh lines in every coordinate direction. The vectors  $\mathbf{f} = (f_{i,j,k})_{i=2,j=2,k=2}^{N_x-1,N_y-1,N_z-1}$  and  $\varphi = (\varphi_{i,j,k})_{i=2,j=2,k=2}^{N_x-1,N_y-1,N_z-1}$  represent the values of the right hand side and the potential on the mesh points, respectively. The right hand side entries for the points next to the boundary contain also the explicit value of the potential on the boundary defined as a Dirichlet boundary condition.

### 3.4.2 Discrete Poisson Equation in a Domain with Elliptical Cross-Section

The elliptical cross-section domain  $\Omega$ , as shown in Figure 3.10, is inscribed into the rectangular domain  $\Gamma$ . Applying Dirichlet boundary conditions on

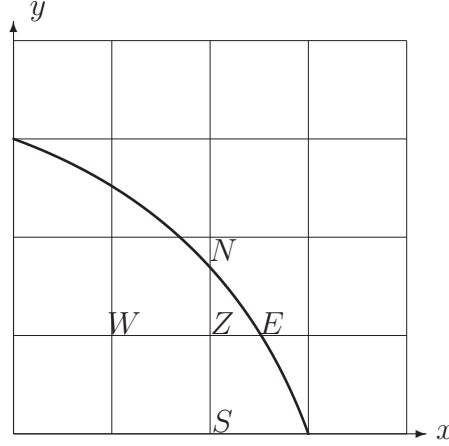


Figure 3.10: Two-dimensional representation of the elliptic shape of the boundary.

the curved boundary  $\partial\Omega = \Omega_1$  the discrete Poisson equation (3.9) needs only to be written for the grid points which are inside  $\Omega$ . Hence, compared with the rectangular domain  $\Gamma$ , the number of unknowns is considerably smaller since in each  $(x, y)$ -plane all grid points which are outside the ellipse are omitted from the computation. The matrix  $\mathbf{A}$  remains block structured but the blocks will have different dimensions (see Figure 3.13). In order to approximate the geometry of the boundary as accurately as possible the finite difference equation (3.9) for each grid point near the boundary needs to take into account the distances to the intersection points of the grid lines and the curved boundary  $\partial\Omega_1$ . Thus, for each point immediately near the boundary  $\partial\Omega_1$  the coefficients in equation (3.9) and so the corresponding entries in  $\mathbf{A}$  are not only determined by the grid spacing but also by the neighboring boundary points. Figure 3.11 shows a grid point  $Z$  which in both directions of the transverse plane neighbors the intersection points  $N$  and  $E$ . By computing the respective distances  $h_n$  and  $h_e$  from point  $Z$  the distances for the appropriate finite difference equation (3.9)  $h_{x,i} \equiv h_e$ ,  $h_{y,j} \equiv h_n$  as well as  $\tilde{h}_{x,i}$  and  $\tilde{h}_{y,j}$  are also determined. If Dirichlet b. c. are defined, the potential of the boundary points is constant and known so that the terms of equation (3.9) containing those potentials move to the right hand side of the equation. In case of a PEC boundary the potential of those boundary points is zero and those terms are completely omitted from the equation. Figure 3.11 displays the non-symmetric discretization star for grid points near the boundary where some of the lengths  $h_n$ ,  $h_s$ ,  $h_w$ ,  $h_e$  are shortened due to the intersection with the boundary curve. Thus it is also clear that even for an equidistant grid spacing the discretization stars of neighboring grid points inside  $\Omega$  are not

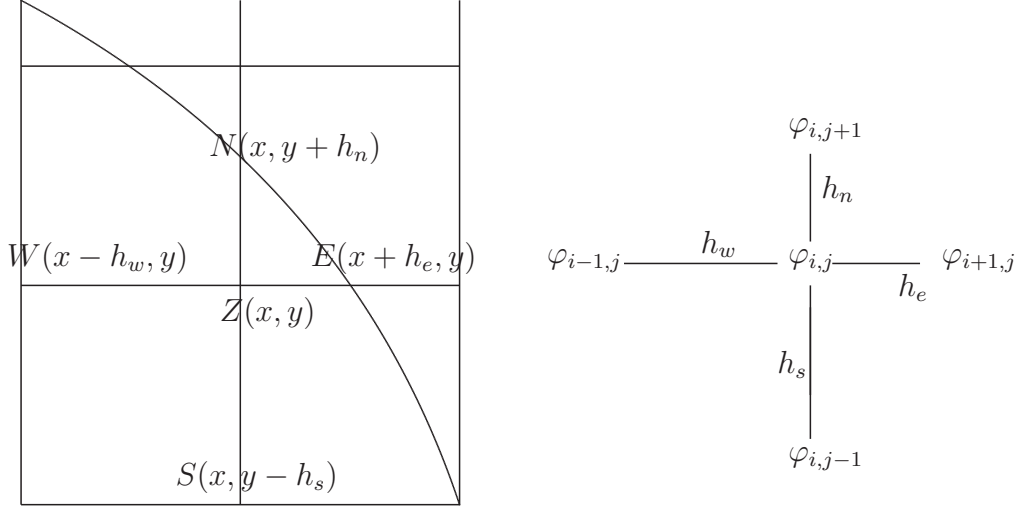


Figure 3.11: Non-symmetric 2-D Shortley-Weller Star.

equal, e.g. the points  $m$  and  $m + 1$  in Figure 3.12. This implies that the discretization matrix  $\mathbf{A}$  for the elliptical domain  $\Omega$  will be non-symmetric. On the other hand the non-equidistant discretization of the rectangular domain  $\Gamma$  would still result in a symmetric system matrix  $\mathbf{A}$ .

To illustrate this we consider only the first row of equation (3.9) which gives the entries next to the main diagonal and contributes to the diagonal entries of the matrix  $\mathbf{A}$ . For the two consecutive points  $m$  and  $m + 1$  as shown in Figure 3.12 we obtain for  $\tilde{h}_{y,j}$ :

$$\tilde{h}_{y,j}^m = \frac{h_{n,m} + h_{s,m}}{2}, \quad \tilde{h}_{y,j}^{m+1} = \frac{h_{n,m+1} + h_{s,m+1}}{2},$$

where  $m$  and  $m + 1$  in the superscript means  $\tilde{h}_{y,j}$  for the  $m$ -th and  $(m + 1)$ -th point, respectively. The first row of equation (3.9) for the point  $m$  reads as

$$\tilde{h}_{y,j}^m \tilde{h}_{z,k}^m \left( -\frac{1}{h_{x,i-1}} \varphi_{i-1,j,k} + \left( \frac{1}{h_{x,i-1}} + \frac{1}{h_{x,i}} \right) \varphi_{i,j,k} - \frac{1}{h_{x,i}} \varphi_{i+1,j,k} \right), \quad (3.12)$$

and for  $m + 1$  as

$$\tilde{h}_{y,j}^{m+1} \tilde{h}_{z,k}^{m+1} \left( -\frac{1}{h_{x,i}} \varphi_{i,j,k} + \left( \frac{1}{h_{x,i}} + \frac{1}{h_{x,i+1}} \right) \varphi_{i+1,j,k} - \frac{1}{h_{x,i+1}} \varphi_{i+2,j,k} \right). \quad (3.13)$$

In order  $\mathbf{A}$  to be symmetric the coefficient multiplying  $\varphi_{i+1,j,k}$  in (3.12) has to be equal with the coefficient multiplying  $\varphi_{i,j,k}$  in (3.13). From Figure 3.12 it is obvious that in the case of a rectangular domain  $\Gamma$ , the distances  $h_{s,m}$  and  $h_{s,m+1}$  are equal and so are  $h_{n,m}$  and  $h_{n,m+1}$ . Thus  $\tilde{h}_{y,j}^m = \tilde{h}_{y,j}^{m+1}$  which means

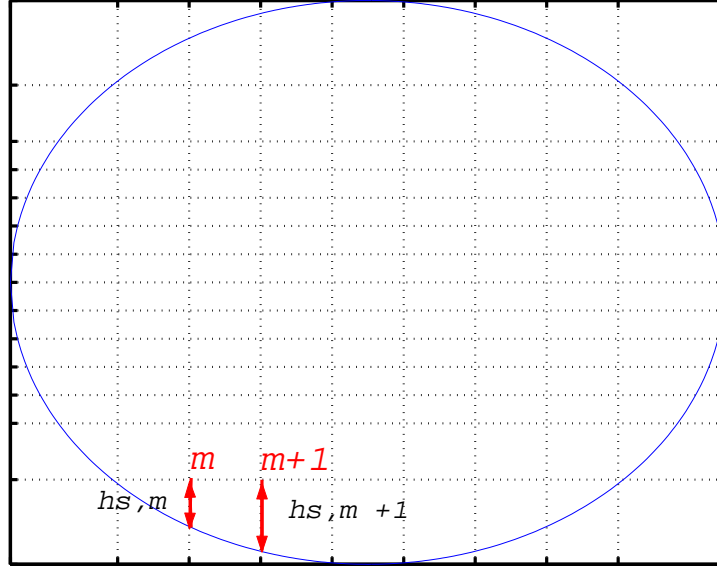


Figure 3.12: Two points  $m$  and  $m + 1$  determining two consecutive rows in the system matrix  $\mathbf{A}$ .

that the respective matrix entries will have the same value ( $\tilde{h}_{y,j}^m \tilde{h}_{z,k}^m / h_{x,i} = \tilde{h}_{y,j}^{m+1} \tilde{h}_{z,k}^{m+1} / h_{x,i}$ ) and the matrix  $\mathbf{A}$  will be symmetric regardless of the non-equidistant mesh. In case of the cylindrical domain  $\Omega$  from Figure 3.12,  $h_{s,m} \neq h_{s,m+1}$  and with it the coefficients  $\tilde{h}_{y,j}^m \neq \tilde{h}_{y,j}^{m+1}$  so that the entries in the two consecutive rows of matrix  $\mathbf{A}$ , above and below the main diagonal, would not be equal which makes the system matrix  $\mathbf{A}$  non-symmetric. However

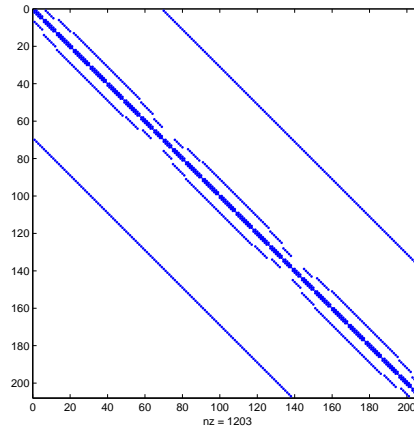


Figure 3.13: Band structure of matrix  $A$  (nz = non-zero elements).

the band structure of matrix  $\mathbf{A}$  will remain symmetric with respect to the main diagonal as shown in Figure 3.13. Furthermore the matrix will remain weak diagonally dominant which eventually makes it also non-singular as in detail shown in [Marković 2005]. The properties of the system matrix  $\mathbf{A}$  are important for the choice of the algorithm for a numerical solution of the system of linear equations which is treated in detail in [Marković 2005]. Although the system matrix  $\mathbf{A}$  is nonsymmetric one it turns out that  $\mathbf{A}$  is positive definite and therefore BiCGSTAB(i.e. [van Rienen 2001]) is an appropriate algorithm to solve the system. The numerical solution of the linear system (3.10) directly yields the electrostatic potential  $\varphi_{i,j,k}$  of each discrete point inside the computational domain  $\Omega$ .

### 3.4.3 Space Charge Field Computation for Different Boundary Conditions

A precise simulation of charged particle dynamics inside a vacuum chamber due to the own or the space charge fields from other particle species, i.e. the e-clouds, requires a precise computation of the electrical field. As shown in the previous sections MOEVE PIC Tracking exploits the finite difference method for the solution of the Poisson equation. The solution depends on the realistic modelling of the material properties and the shape of the boundary. Since the vacuum chamber of particle accelerators is made of copper or a superconducting material, the boundary of the computational domain could be assumed to be a Perfect Electric Conductor (PEC). Practically, a ground potential of  $\varphi_b = 0\text{V}$  is applied on the boundary.

From electromagnetic theory it is well known that in the presence of a conducting surface the electric field of a space charge is distorted because it has to fulfill the boundary condition(b. c.) to be perpendicular to the surface. Hence the computed space charge field distribution inside the vacuum chamber depends also on the boundary shape of the computational domain. Especially for simulations of transversal bunch instabilities a precise discretization of the transverse boundary shape is very important in order to get more accurate field distribution inside the beam pipe. A possible error of the field leads immediately to an error of the space charge force which individual particles experience. Since a PIC tracking program (which models the interactions of a single bunch and electron clouds) requires a computation of the space charge fields at each discrete time step, the perpetual error of the field distribution might lead to incorrect simulation of the particle dynamics.

Many simulation tools used in particle accelerator design use conducting b.c. applied on a rectangular cross section of the computational domain or apply a so called open b.c. by letting the potential decline with  $1/r$  rate from the

centroid position of the distribution. However the rectangular cross section is not the best approximation of the true geometry of the beam pipe. Currently in MOEVE PIC Tracking the beam pipe cross section can be additionally approximated by an arbitrary elliptical shape on which PEC boundary conditions are applied.

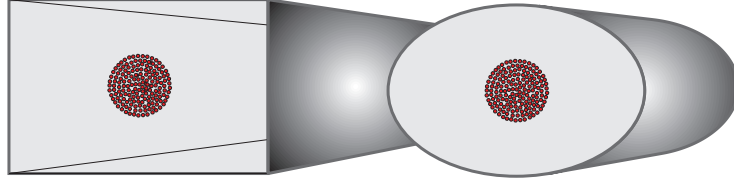


Figure 3.14: Rectangular and elliptic domain for space charge field computation bounded with perfect electric conductor.

In order to illustrate the difference in the computed fields in the following section we present 3D space charge field computation results for open (free space) and conducting b.c.. Conducting b.c. are applied on the transverse walls of rectangular and elliptic domains shown in Fig.3.14.

#### 3.4.3.1 Conducting boundary conditions on beam pipes with elliptical cross section

To compare the computed fields with open and conducting b.c. on a rectangular and elliptic pipe we choose a spherical bunch with uniformly distributed charge of  $-1$  nC, situated in the center of the beam pipe without any velocity. The bunch radius  $r$  is 10 mm. The domain represents a beam pipe of certain length with different cross sections. In the axial  $z$  direction the domain is bounded by open boundary condition. The rectangular cross section is quadratic with  $a = 100$  mm or rectangular with sides  $a = 150$  mm and  $b = 100$  mm. The elliptical domain cross section is inscribed in the rectangular domain so that the ellipse half axes are  $a = b = 100$  mm or  $a = 150$  mm and  $b = 100$  mm.

Figures 3.15 and 3.16 plot the  $x$  component of the electrical field  $E_x$  along the  $x$  axis ( $y = 0$ ). The  $E_x$  component is perpendicular on the domain boundary for any of the domains. Since the boundary is far from the bunch ( $r_b \ll a, b$ ) the  $E_x$  field values are almost equal for the open b.c. and the conducting b.c. in both the circular/quadratic (Fig.3.15) and the elliptic/rectangular (Fig.3.16) cross sections.

However plotting  $E_x$  along  $y = b/2$  line reveals the differences in the electrical field for different boundary conditions and shapes. Both Fig. 3.17 and Fig. 3.18 show that the  $E_x$  field component far from the boundaries



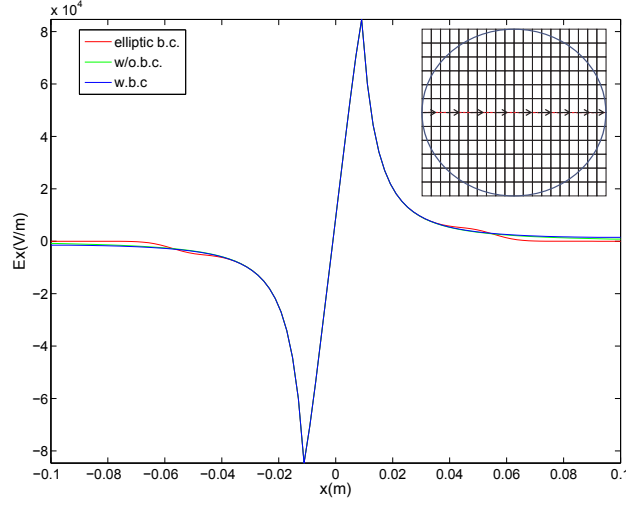


Figure 3.15: Electric field  $E_x$  along  $x$ -axis of a square  $a = b$ , computed with open (w/o.b.c.) and conducting b.c. on a rectangular (w.b.c.) and elliptic (elliptic b.c.) pipe.

matches fairly good for all types of boundary conditions and shapes. Yet  $E_x$  becomes significantly different approaching the boundary of the domain. The maximum of  $E_x$  along  $y = b/2$  for the elliptic domain differs at position

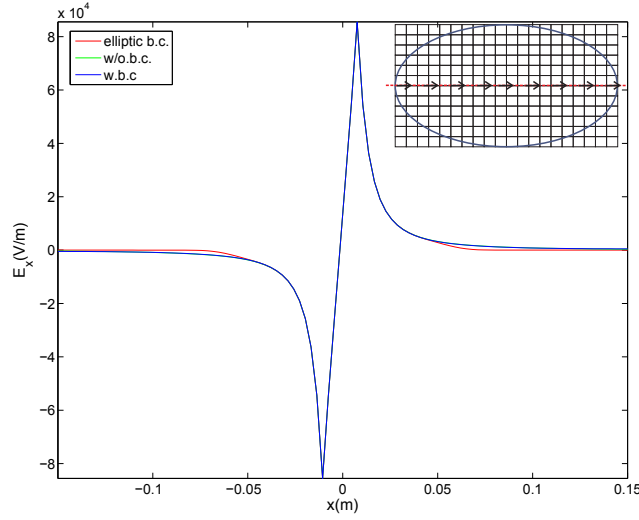


Figure 3.16: Electric field  $E_x$  along  $x$ -axis of a rectangular box  $a = 1.5b$ , computed with open (w/o.b.c.) and conducting b.c. on a rectangular (w.b.c.) and elliptic (elliptic b.c.) pipe.

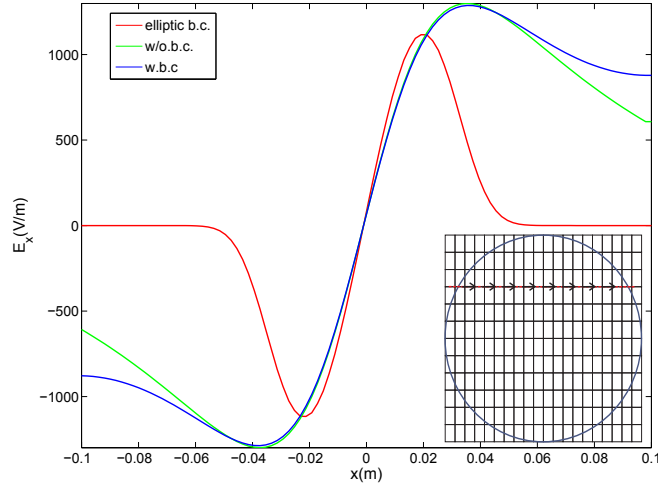


Figure 3.17: Electric field  $E_x$  along  $y = \pm b/2$  of a square  $a = b$  computed with open (w/o.b.c.) and conducting b.c. on a rectangular (w.b.c.) and elliptic (elliptic b.c.) pipe.

and in its value from the extreme values for the rectangular domain with PEC and open b.c.. Since the rectangular domain is large compared to the bunch size the field distribution in the rectangular domain with PEC and open b.c.

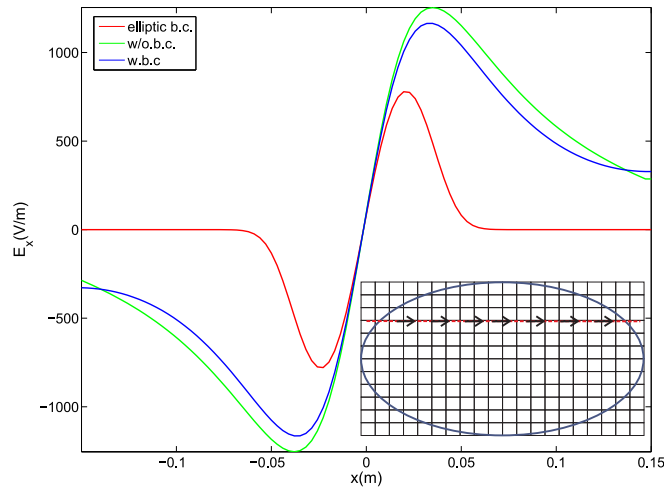


Figure 3.18: Electric field  $E_x$  along  $y = \pm b/2$  of a square  $a = b$  computed with open (w/o.b.c.) and conducting b.c. on a rectangular (w.b.c.) and elliptic (elliptic b.c.) pipe.

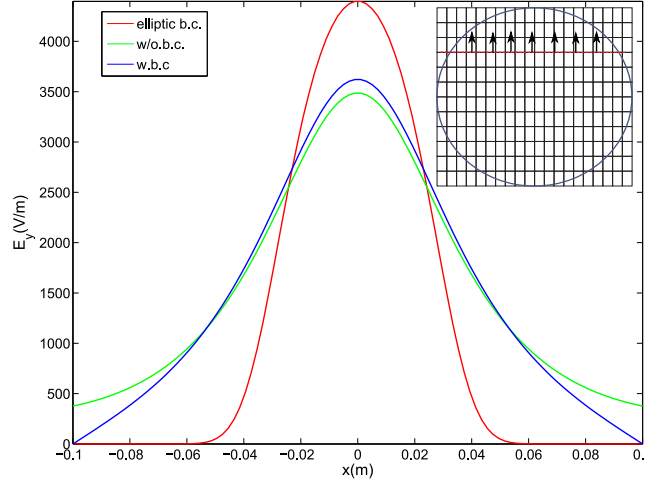


Figure 3.19: Electric field  $E_y$  along  $y = \pm b/2$  of a square  $a = b$  box computed with open (w/o.b.c.) and conducting b.c. on a rectangular (w.b.c.) and elliptic (elliptic b.c.) pipe.

doesn't differ much. Comparing  $E_x$  at the boundary of the rectangular domain with PEC and open b.c. in 3.17 and 3.18 it is evident that the smaller the domain is the stronger will be the field on the PEC boundary. Since the total energy of the field has to be equal for all the domains the smaller the domain is the higher the electric field will be inside. Thus in Fig.3.19 the  $E_y$  along  $y = b/2$  for the circular domain with PEC b.c. has the highest amplitude.

A general observation from the field computation is that the difference between the electric field computed in the rectangular domain with PEC and open b.c. and the PEC bounded elliptical cylinder becomes more significant towards the boundary of the beam pipe. Furthermore the space charge fields compared here are computed for a resting bunch. However in practical applications the bunches are ultra-relativistic with  $\gamma$  of several thousands. Their transverse field in the laboratory frame (as shown in section 2.1.4) is  $\gamma$  times stronger than the computed transverse field in the rest frame. Finally it means that the absolute difference of the fields compared here is also  $\gamma$  times stronger in the laboratory frame. That is a very important perception for the simulation of the interaction between the bunch and the electron cloud since the electrons fill the whole beam pipe. Regarding the simulation of electron cloud build-up the discrepancy in the field near the boundary influences the number and the energy of the produced secondary electrons from the beam pipe. The results stress the necessity of an accurate description of the computational domain.

### 3.4.4 Computation of the electric field for relativistic bunches

As previously described the charge of the macro-particles is deposited on the grid nodes in the laboratory frame of the bunch. Since the bunch has a relativistic velocity in one particular direction, before the Poisson Equation is solved, the setup is transformed in the bunch center of mass frame. Practically

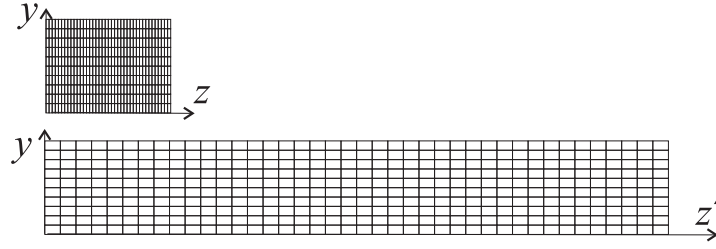


Figure 3.20: Cartesian grid in the laboratory frame (up) and in the bunch rest frame (down).

the distance of the grid nodes in direction of the bunch motion is multiplied by the Lorentz factor  $\gamma$ , whereas the transverse grid spacing remains as in the laboratory frame. In the bunch rest frame the Poisson equation will be solved as previously described and the result is an electrostatic potential  $\varphi_m$  for each grid node  $m$  ( $m = i + (j - 1)N_x + (k - 1)N_xN_y$ ) of the domain. With the computed grid electrostatic potential  $\varphi_m$  back in the laboratory frame the field components on the edges of the Cartesian grid cells are computed as:

$$\begin{aligned} E_x(x_i, y_j, z_k) &= -\gamma(\varphi(x_{i+1}, y_j, z_k) - \varphi(x_i, y_j, z_k))/h_{x,i}, \\ E_y(x_i, y_j, z_k) &= -\gamma(\varphi(x_i, y_{j+1}, z_k) - \varphi(x_i, y_j, z_k))/h_{y,j}, \\ E_z(x_i, y_j, z_k) &= -(\varphi(x_i, y_j, z_{k+1}) - \varphi(x_i, y_j, z_k))/h_{z,k}. \end{aligned} \quad (3.14)$$

Where  $h_{x,i}$ ,  $h_{y,j}$  and  $h_{z,k}$  are the corresponding grid subintervals in  $x$ ,  $y$  and  $z$  direction of the grid in the bunch laboratory frame.

### 3.4.5 Comparison of the transverse field with analytical Bassetti-Erskine expression

Many simulation programs which simulate beam-e-cloud interaction (i.e. [Furman 1997], [Rumolo 2001], [Ohmi 2000b]) use the analytical Bassetti-Erskine (BE) expression [Bassetti 1980] for the electromagnetic field of a two-dimensional Gaussian charge distribution. Thereby the three-dimensional bunch is sliced in a series of consecutive two-dimensional charge distributions perpendicular to the direction of motion as shown in Fig. 3.21. The expression

in terms of the complex error function  $w(z)$  assumes that the two-dimensional charge distribution is Gaussian with dimensions described by the standard deviations of the distribution  $\sigma_x$  and  $\sigma_y$  and the total charge of the 2D bunch is  $Q$ . The field components  $E_x$  and  $E_y$  according to the BE formula read as

$$\begin{aligned} E_x &= \frac{Q}{2\varepsilon_0\sqrt{2\pi(\sigma_x^2-\sigma_y^2)}} \mathbf{Im} \left( w\left(\frac{x+iy}{\sqrt{2(\sigma_x^2-\sigma_y^2)}}\right) - e^{[-\frac{x^2}{2\sigma_x^2} + \frac{y^2}{2\sigma_y^2}]} w\left(\frac{\frac{x\sigma_y}{\sigma_x} + iy\frac{\sigma_x}{\sigma_y}}{\sqrt{2(\sigma_x^2-\sigma_y^2)}}\right) \right), \\ E_y &= \frac{Q}{2\varepsilon_0\sqrt{2\pi(\sigma_x^2-\sigma_y^2)}} \mathbf{Re} \left( w\left(\frac{x+iy}{\sqrt{2(\sigma_x^2-\sigma_y^2)}}\right) - e^{[-\frac{x^2}{2\sigma_x^2} + \frac{y^2}{2\sigma_y^2}]} w\left(\frac{\frac{x\sigma_y}{\sigma_x} + iy\frac{\sigma_x}{\sigma_y}}{\sqrt{2(\sigma_x^2-\sigma_y^2)}}\right) \right), \end{aligned} \quad (3.15)$$

where the complex error function  $w(z)$  read as:

$$w(z) = e^{-z^2} \left( 1 + \frac{2i}{\sqrt{\pi}} \int_0^z e^{\zeta^2} d\zeta \right). \quad (3.16)$$

Regarding the application of the BE formula for the interaction simulation it is interesting to see if the transverse electric fields computed by the BE formula are matching with the transverse electric fields computed by our 3D MOEVE Poisson solver. Here the field components  $E_x$  and  $E_y$  are compared in an infinitesimal thin transversal plane at a certain longitudinal position  $z$  in the bunch. As previously shown the bunch is defined in the laboratory frame with a macro-particle distribution in the six-dimensional phase space  $\Psi(x, p_x, y, p_y, z, p_z)$ . Each macro-particle is located inside a grid cell and its charge, correspondingly to its position in the cell, is weighted on the eight grid nodes defining that 3D grid cell, where four of the eight cell nodes belong to one discrete transversal plane. For an appropriate comparison of the fields in a transversal plane at position  $z$ , the input charge  $Q$  in the BE formula should be equal to the corresponding line charge density  $\lambda_b(z)$  of the bunch at  $z$ . The  $E_x$  and  $E_y$  components are compared on one of the discrete transversal grid planes of the 3D discretization domain. The amount of charge  $Q_m$  deposited on that transversal plane can be considered as the total amount of charge between two neighboring transversal planes of the 3D Cartesian grid and therefore should be divided by the distance between the planes  $h'_z$ . Since MOEVE computes the fields in the rest frame of the relativistic bunch, the length  $h_z$  (defined in the laboratory frame) is multiplied by the relativistic factor  $\gamma$ . Hence the distance between transversal planes in the rest frame is  $h'_z = \gamma h_z$  and the input charge for the BE formula is  $\lambda_b(z) = Q_m/h'_z$ . It follows a comparison of the computed transversal fields  $E_x$  and  $E_y$  in the middle transversal plane (as principally shown in Fig. 3.21) of two positron bunches defined in Table A.3. The positron bunch in the damping ring of the planned International Linear Collider (ILC) [Committee 2003] is defined as Gaussian

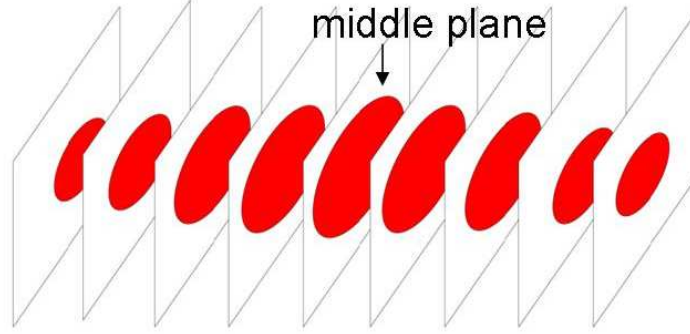


Figure 3.21: In order to compute the fields of the bunch with the BE formula (for simulation interaction with e-clouds) the bunch charge is represented as a series of two dimensional charge distributions.

distribution with  $\sigma_x = 0.6$  mm,  $\sigma_y = 0.006$  mm and  $\sigma_z = 6$  mm and its charge ( $Q = 3.22$  nC) discretized in the longitudinal direction as shown in Figure 3.22. Similarly the charge ( $Q = 5.28$  nC) of the KEKB Low Energy Ring (KEKB LER) [Funakoshi 2001] bunch ( $\sigma_x = 0.42$  mm,  $\sigma_y = 0.06$  mm and  $\sigma_z = 6$  mm) is discretized in the longitudinal direction as shown in Figure 3.23. The maximum in Figure 3.22 ( $Q_m = 4.118 \cdot 10^{-10}$  C) and Figure 3.23 ( $Q_m = 6.7525 \cdot 10^{-10}$  C) is the charge at the middle transversal plane of the ILC and the KEKB positron bunch, respectively. This value can be considered as the total charge between two transversal planes. The longitudinal grid discretization in the laboratory frame provides  $h_z = 2$  mm. Since the bunch is highly relativistic (5 GeV energy for the ILC positron bunch in the damping

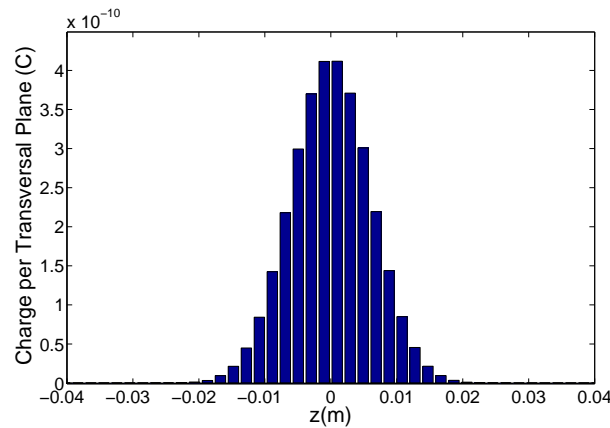


Figure 3.22: Discretized longitudinal charge distribution of the ILC bunch.

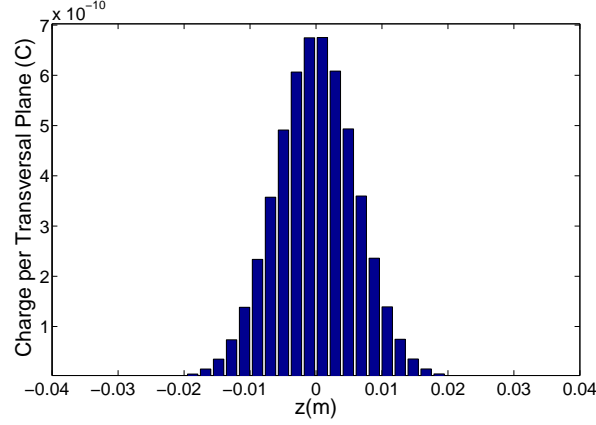


Figure 3.23: Discretized longitudinal charge distribution of the KEKB bunch.

ring and 3.5 GeV for the KEKB LER positron bunch), in the rest frame  $h_z$  multiplies by  $\gamma$  ( $\gamma = 9765.7$  and  $\gamma = 6836$ ) and yields  $h'_z = \gamma h_z$ . Thus the obtained line density is  $\lambda_b = Q_m/h'_z = 2.1084 \cdot 10^{-11}$  C/m for the ILC and  $\lambda_b = Q_m/h'_z = 4.9389 \cdot 10^{-11}$  C/m for the KEKB LER as input charge for the BE formula. The field components computed by means of the BE formula

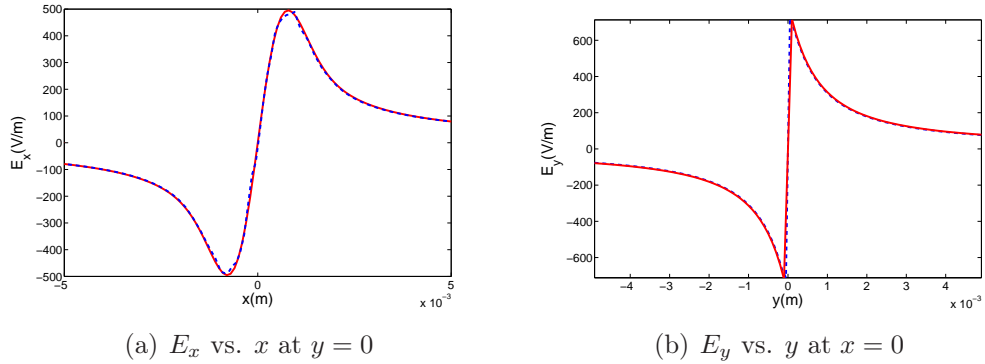


Figure 3.24: ILC bunch: BE (solid) and 3D MOEVE (dashed lines).

are compared to the results computed by the 3D Poisson solver MOEVE on the middle transversal plane. The 3D Poisson solver assumed perfect electrical conductor boundary condition (PEC b.c.) on a circular beam pipe with a radius of  $r = 5$  mm. It should be pointed out that the fields compared here are the fields in the rest frame of the bunch. The fields that the e-cloud experience in the laboratory frame are multiplied by the corresponding  $\gamma$ . The plots of  $E_x$  at  $y=0$  and  $E_y$  at  $x=0$ , are presented in Figure 3.24 for the ILC and in Figure 3.25 for the KEKB bunch. The discretization is non-equidistant in  $y$ -direction with an aspect ratio of 2. Figures 3.26 and 3.27 show  $E_x$  and

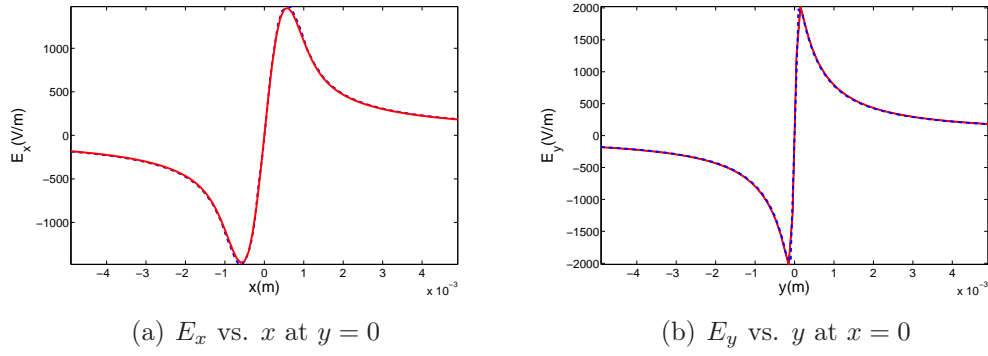


Figure 3.25: KEKB LER bunch: BE (solid) and 3D MOEVE (dashed lines).

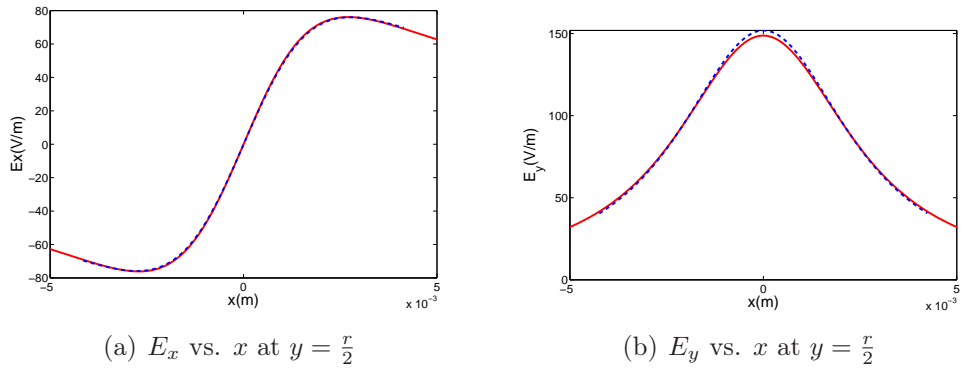


Figure 3.26: ILC bunch: BE (solid) and 3D MOEVE (dashed lines).

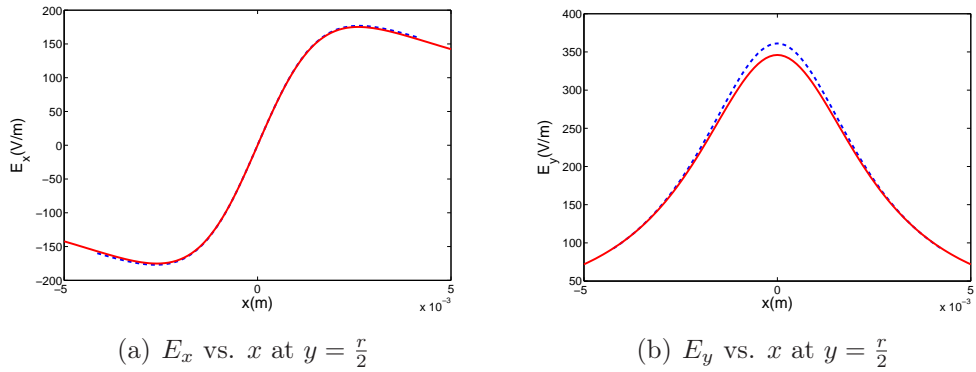


Figure 3.27: KEKB bunch: BE (solid) and 3D MOEVE (dashed lines).

$E_y$  at  $y = \frac{r}{2}$  for the ILC and the KEKB bunch, respectively. Figures 3.24-3.27 show a very good match of the fields computed with BE (solid lines) and MOEVE PIC Tracking (dashed lines).



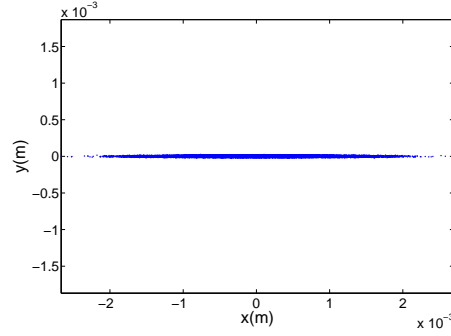


Figure 3.28: Transversal profile of the ILC flat beam, Gaussian distribution in every direction with  $\sigma_x = 0.6$  mm,  $\sigma_y = 0.006$  mm,  $\sigma_z = 6$  mm.

Regarding the simulation of bunch - e-cloud interaction, the results presented here justify the approach used in many programs of the so-called  $2+1/2$  dimensional modelling of the bunch. Thereby the bunch is represented as a sequence of particle distributions in transversal planes as principally shown in Fig. 3.21. The e-cloud interacting with the bunch is also defined as a particle distribution in a single transversal plane at a certain position in the storage ring. The interaction simulation is a sequence of two dimensional interactions of the bunch transverse planes with the e-cloud plane. The fields of the bunch are computed using the analytical BE formula which takes as input the corresponding line charge density  $\lambda_b(z)$  and the slice dimensions ( $\sigma_x$  and  $\sigma_y$ ). Generally the more transversal slices the bunch is divided into the better dynamic simulation is achieved. On the other hand the fields from the fast changing transversal distribution of the electrons in the cloud, during the interaction with the beam, can not be approximated well by the BE formula since the e-cloud distribution in the transversal plane is far from being Gaussian. Therefore the interaction of the bunch with the e-cloud can be more precisely computed by approximating the fields with the Poisson solver MOEVE. Furthermore it allows a full 3D beam - e-cloud interaction simulation.

### 3.5 Interpolation of the Electrical Field

After computing the  $\mathbf{E}$  field on the grid in the laboratory frame each field component needs to be interpolated to the position of each macro-particle. A macro-particle with coordinates  $(x, y, z)$  can be situated anywhere inside a grid cell defined by grid line pairs:  $(x_i, x_{i+1})$ ,  $(y_j, y_{j+1})$  and  $(z_k, z_{k+1})$ . Hence particle coordinates satisfy:  $x_i < x < x_{i+1}$ ,  $y_j < y < y_{j+1}$  and  $z_k < z < z_{k+1}$ . In MOEVE PIC Tracking the field components at the macro-particles position

are approximated with a trilinear interpolation method which is explained in the following. For reasons of clarity and comprehensibility the explanation is given only for one direction ( $E_x$ ). The interpolation for the two other components  $E_y$ ,  $E_y$  is identical. Figure 3.29 displays the grid electrical fields

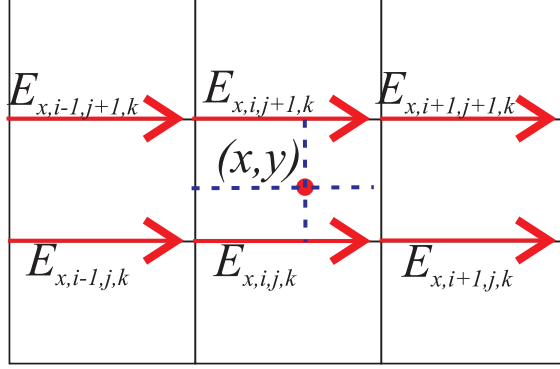


Figure 3.29: The horizontal components of the electrical field in the transverse plane  $z_k$ .

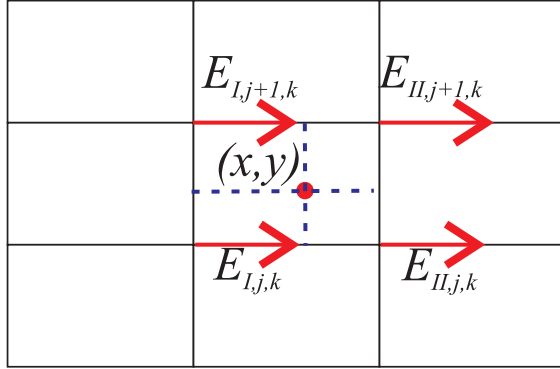


Figure 3.30: Linear interpolation between the neighboring grid fields yields the field values in the corner nodes of the cell the particle belongs to.

computed straight from the potential  $\varphi$  and the grid distances  $h_x$ . Figure 3.29 shows part of the transverse  $((x, y))$  plane at the lower axial value  $z_k$ . A linear interpolation between the neighboring grid fields yields the field values in the corner nodes of the cell the particle belongs to. For the four grid nodes on the transverse plane at  $z_k$  shown in Fig. 3.30) the field is given as:

$$\begin{aligned} E_{I,j+1,k} &= (E_{x,i-1,j+1,k}h_{x,i} + E_{x,i,j+1,k}h_{x,i-1})/(h_{x,i-1} + h_{x,i}), \\ E_{II,j+1,k} &= (E_{x,i,j+1,k}h_{x,i+1} + E_{x,i+1,j+1,k}h_{x,i})/(h_{x,i} + h_{x,i+1}), \\ E_{I,j,k} &= (E_{x,i-1,j,k}h_{x,i} + E_{x,i,j,k}h_{x,i-1})/(h_{x,i-1} + h_{x,i}), \end{aligned}$$

$$E_{II,j,k} = (E_{x,i,j,k}h_{x,i+1} + E_{x,i+1,j,k}h_{x,i})/(h_{x,i} + h_{x,i+1}).$$

Interpolating the field along the grid lines in  $x$  direction at the particles position  $x$  leads to the field components  $E_{j,k}$ ,  $E_{j+1,k}$  as displayed in 3.31:

$$E_{j+1,k} = (E_{I,j+1,k}(x_{i+1} - x) + E_{II,j+1,k}(x - x_i))/h_{x,i},$$

$$E_{j,k} = (E_{I,j,k}(x_{i+1} - x) + E_{II,j,k}(x - x_i))/h_{x,i},$$

The  $E_{j,k}$ ,  $E_{j+1,k}$  belong to the transverse plane at  $z_k$ . Similarly the fields  $E_{j,k+1}$ ,  $E_{j+1,k+1}$  at the the transverse plane  $z_{k+1}$  are also interpolated. Figure 3.32 displays the field components  $E_{j,k}$ ,  $E_{j+1,k}$ ,  $E_{j,k+1}$  and  $E_{j+1,k+1}$  along the horizontal grid lines at the particles position  $x$ .

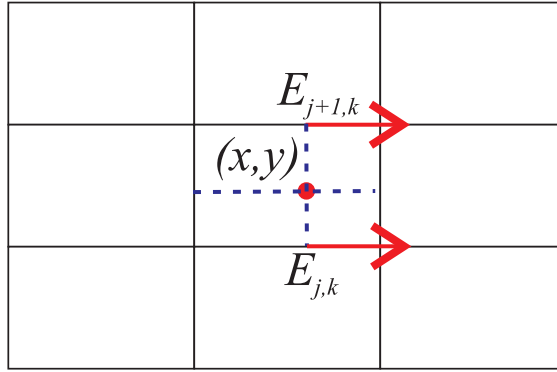


Figure 3.31: Interpolation of the field along the grid lines in  $x$  direction at the particles position  $x$ .

Finally the  $E_x$  component acting on the particle at the position  $(x, y, z)$  is interpolation of  $E_{j,k}$ ,  $E_{j+1,k}$ ,  $E_{j,k+1}$  and  $E_{j+1,k+1}$  in the  $(z,y)$  plane:

$$E_x = \frac{E_{j,k} \triangle z_2 \triangle y_2 + E_{j+1,k} \triangle z_2 \triangle y_1 + E_{j+1,k+1} \triangle z_1 \triangle y_1 + E_{j,k+1} \triangle z_1 \triangle y_2}{(h_{z,k+1} - h_{z,k})(h_{y,j+1} - h_{y,j})}.$$

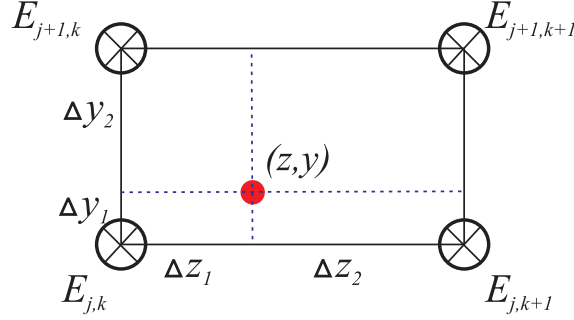


Figure 3.32: Field components on the horizontal grid lines at the particles position  $x$ .  $E_{j,k}$  and  $E_{j+1,k}$  at  $z_k$  and  $E_{j,k+1}$  and  $E_{j+1,k+1}$  at  $z_{k+1}$ .

### 3.6 Integration of the Equations of Motion

From equation (2.32) emerges a system of two ordinary differential equations (3.17) describing the motion of each macro-particle. For the  $i$ -th macro-particle at position  $\mathbf{r}_i$  with charge  $Q_i$ , rest mass  $M_i$  and velocity  $\mathbf{v}_i$  the equations of motion read as follows:

$$\begin{aligned} \frac{d(\gamma_i \mathbf{v}_i)}{dt} &= \frac{Q_i}{M_i} (\mathbf{E}_i + \mathbf{v}_i \times \mathbf{B}_i), \\ \frac{d\mathbf{r}_i}{dt} &= \mathbf{v}_i, \quad i = 1, \dots, N_p. \end{aligned} \quad (3.17)$$

The magnitude of the particle velocity  $\mathbf{v}_i$ , in Cartesian coordinates  $|\mathbf{v}_i| = \sqrt{v_{x,i}^2 + v_{y,i}^2 + v_{z,i}^2}$ , defines the Lorentz factor of the  $i$ -th macro-particle:

$$\gamma_i = (1 - |\mathbf{v}_i|^2/c^2)^{-1/2}.$$

The relativistic mass of the macro-particle is the product of the rest mass  $M_i$  and the Lorentz factor  $\gamma_i$ , whereas its relativistic momentum is  $\mathbf{p}_i = \gamma_i M_i \mathbf{v}_i$ . Since the rest mass  $M_i$  is a constant, it pairs with the charge of the macro-particle  $Q_i$  on the right hand side of equation (3.17) whereas  $\gamma_i \mathbf{v}_i$  represents a time variable which in MOEVE PIC Tracking is denoted as  $\mathbf{u}_i = \gamma_i \mathbf{v}_i$ . Hence the equation of motion (3.17) can be written as:

$$\frac{d\mathbf{u}_i}{dt} = \frac{Q_i}{M_i} (\mathbf{E}_i + \frac{\mathbf{u}_i}{\gamma_i} \times \mathbf{B}_i) \quad (3.18)$$

The electric field  $\mathbf{E}_i$  and the magnetic flux density  $\mathbf{B}_i$  responsible for the particle acceleration are the superposition of external and self-induced fields at the position of the  $i$ -th macro-particle in the bunch laboratory frame. Since the variable  $\mathbf{u}_i$  appears also on the rhs, the time integration of equation (3.18)

is not straight forward. Hence a numerical time integration must be applied. Widely spread is the Runge-Kutta Method of different order (RK2, RK4), however the higher the order of the method the higher the memory demand of the integration scheme will be. In MOEVE PIC Tracking the well known Leap-Frog time integration scheme (Fig. 3.33) has been applied. Thereby the time axis is discretized and the computation of the space charge fields and the computation of the particle velocity are staggered by half a time step ( $\Delta t/2$ ).

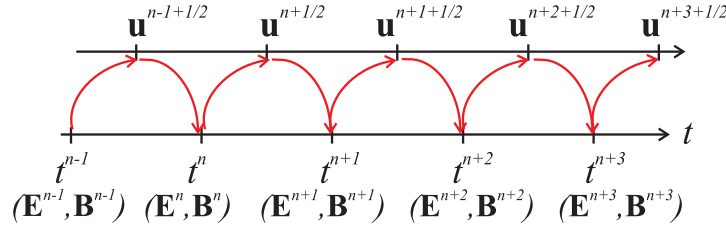


Figure 3.33: Leap-Frog time integration scheme.

The numerical integration method is stable for discrete time steps smaller than  $\Delta t_{max}$  computed by the Courant-Levy stability condition:

$$\Delta t_{max} = \frac{1}{c} \frac{1}{\sqrt{(\frac{1}{\Delta x_{min}})^2 + (\frac{1}{\Delta y_{min}})^2 + (\frac{1}{\Delta z_{min}})^2}}.$$

Finally the discrete equation of motion for the relativistic particles writes as:

$$\frac{\mathbf{u}_i^{n+\frac{1}{2}} - \mathbf{u}_i^{n-\frac{1}{2}}}{\Delta t} = \frac{Q_i}{M_i} [\mathbf{E}_i^n + \frac{\mathbf{u}_i^{n+\frac{1}{2}} - \mathbf{u}_i^{n-\frac{1}{2}}}{2\gamma_i^n} \times \mathbf{B}_i^n]. \quad (3.19)$$

For the computation of  $\mathbf{u}^{n+\frac{1}{2}}$  from equation 3.19 an algorithm is implemented which is known as the Boris pusher and is described in detail in [Birdsall 1991]. It has been successfully implemented in several plasma simulation programs and the penalty for its parallelization is relative low. The computation of  $\mathbf{u}^{n+\frac{1}{2}}$  from  $\mathbf{u}^{n-\frac{1}{2}}$  takes place in several steps. First a half of the momentum change due to the electric field is added to  $\mathbf{u}^{n-\frac{1}{2}}$ .

$$\mathbf{u}_i^- = \mathbf{u}_i^{n-\frac{1}{2}} + \frac{Q_i}{M_i} \frac{\mathbf{E}_i^n \Delta t}{2} \quad (3.20)$$

A central point in the algorithm is the rotation due to the magnetic field to get  $\mathbf{u}_i^+$ .

$$\frac{\mathbf{u}_i^+ - \mathbf{u}_i^-}{\Delta t} = \frac{Q_i}{2\gamma_i^n M_i} (\mathbf{u}_i^+ - \mathbf{u}_i^-) \times \mathbf{B}_i^n \quad (3.21)$$

Since a direct solution for the implicit equation 3.21 is complicated and computationally expensive an approximate solution for the rotation of the particle

## 72 Chapter 3. Modelling and Implementation of Particle Tracking

is used. Due to the  $\mathbf{B}$  field the particles momentum  $\mathbf{u}$  rotates around an axis which is parallel to the  $\mathbf{B}$  field vector and the angle of rotation  $\theta$  is approximated by  $\theta = -2 \arctan(Q_i B \Delta t / 2 \gamma_i^n M_i)$ . Thereby  $B$  is the amplitude of the  $\mathbf{B}_i^n$  field and  $\Delta t$  the discrete time step between  $t_{n-1/2}$  and  $t_{n+1/2}$ .  $\gamma_i^n$  represents the mean value between the time steps:  $\gamma_i^n = \frac{1}{2}(\gamma_i^{n-1/2} + \gamma_i^{n+1/2})$  and since during the rotation of the particle  $\gamma_i^n$  does not change it can be computed as  $\gamma_i^n = \sqrt{1 + (u_i^-/c)^2}$ . The error made by using the mean value of  $\gamma_i^n$  in the Leap-Frog scheme is proportional to  $\Delta t^3$ . For arbitrary directions of  $\mathbf{u}_i$  and  $\mathbf{B}_i$  the rotation is realized with the help of two vectors parallel with  $\mathbf{B}_i$ :

$$\mathbf{t}_i = \frac{Q_i \Delta t}{2 \gamma_i^n M_i} \mathbf{B}_i \quad \mathbf{s}_i = \mathbf{t}_i \frac{2}{1 + t_i^2} \quad (3.22)$$

As described in [Birdsall 1991] an intermediate vector  $\mathbf{u}'_i$ :

$$\mathbf{u}'_i = \mathbf{u}_i^- + \mathbf{u}_i^- \times \mathbf{t}_i, \quad (3.23)$$

is needed in order to accomplish the rotation of the momentum with

$$\mathbf{u}_i^+ = \mathbf{u}_i^- + \mathbf{u}'_i \times \mathbf{s}_i. \quad (3.24)$$

At last the second half of the momentum change due to the electric field is added to  $\mathbf{u}_i^+$  to obtain  $\mathbf{u}_i^{n+\frac{1}{2}}$ :

$$\mathbf{u}_i^{n+\frac{1}{2}} = \mathbf{u}_i^+ + \frac{Q_i}{M_i} \frac{\mathbf{E}_i^n \Delta t}{2}. \quad (3.25)$$

The velocity of the particle can be easily obtained from  $\mathbf{v}_i^{n+\frac{1}{2}} = \mathbf{u}_i^{n+\frac{1}{2}} / \gamma_i^{n+\frac{1}{2}}$  where  $\gamma_i^{n+\frac{1}{2}} = \sqrt{1 + (u_i^{n+\frac{1}{2}}/c)^2}$ . Finally the new position of the particle in the discrete time  $t^{n+1}$  can be easily received as:

$$\mathbf{r}_i^{n+1} = \mathbf{r}_i^n + \mathbf{v}_i^{n+\frac{1}{2}} \Delta t. \quad (3.26)$$

The implementation of the algorithm for the time integration of the particle motion as well as the Poisson solver in MOEVE PIC Tracking are parallelized for shared memory architecture according to the Open MP specifications [Chapman 2007].

### 3.6.1 Tracking of Relativistic Particles

Tracking of a bunch under the influence of its own field additionally to any external fields requires very fine discretization of the bunch in order to achieve satisfying accuracy for the Poisson Solver. However, having in mind that

the tracking distances have an order of magnitude in meters while the bunch rms. lengths are in millimeters and the time stepping has to be in picoseconds, it is obvious that a single stationary grid can not be utilized without having a huge number of grid nodes (hundreds of millions). Computing the appropriate linear system of equations at each time step for such a big number of grid nodes is even for a highly parallelized computation very expensive. On the other hand during the tracking of the bunch with its own space charge forces the focus of interest are only the bunch properties. Hence there is no interest in discretizing the whole path of the bunch at ones.

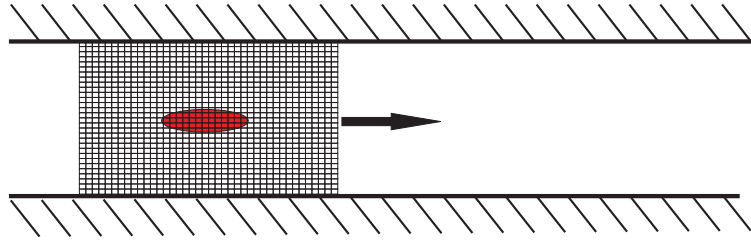


Figure 3.34: The grid moves in longitudinal direction with the bunch.

In MOEVE PIC Tracking, as principally shown in Fig.3.34, the grid can be defined as a moving frame of the bunch which moves in longitudinal direction with the same speed as the bunch. The frame can be defined arbitrarily. Usually it is defined to start two absolute bunch lengths before and ends two absolute bunch lengths after the bunch. During the simulation MOEVE PIC Tracking writes result files containing the position of each macro-particle in the six-dimensional phase space at designated time point. The result files enable the computation of beam parameters such as emmitances, energies, reconstructing trajectories of individual particles etc..

In the following an example is given of a bunch tracking with MOEVE PIC Tracking. A bunch of 1nC charge with Gaussian distribution in all three directions with rms. lengths  $\sigma_x = \sigma_y = \sigma_z = 1\text{mm}$  is tracked in a drift of 1m length. The kinetic energy at the beginning of the drift is  $E_{kin} = 5\text{ MeV}$  without any dispersion i.e. all the particles of the bunch have the same longitudinal momentum whereas the transversal momentum is defined as  $p_x = p_y = 0$ . Figure 3.35 (left) shows the initial particle distribution of  $10^5$  macro-particles in the  $z-y$  plane and the value of the Lorentz factor  $\gamma$  of each macro-particle. The initial distribution is generated by the generator program of the package Astra [Flöttmann 2000]. The bunch is tracked in circular beam pipe with radius  $r=10\text{ mm}$ . A non-equidistant grid of the moving frame is defined with  $N_x = N_y = N_z = 81$  grid lines. The tracking time is  $t_{end} = 3.5\text{ ns}$  and a time stepping for the trajectory integration is  $\Delta t = 10\text{ ps}$  whereas a results file has been written every 100 ps. Figure 3.35 (right) shows the

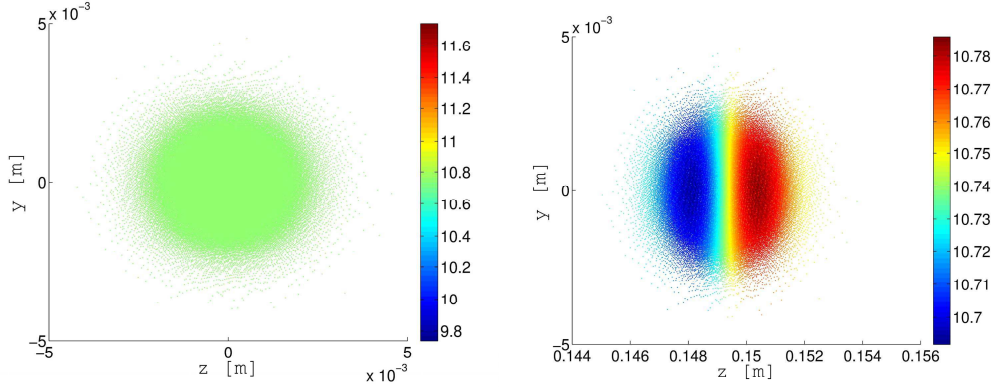


Figure 3.35: Left: Initial particle distribution of the bunch with  $E_{kin} = 5$  MeV and Lorentz factor  $\gamma = 10.7384$ . Right: Particle and  $\gamma$  distribution after 500 ps drift.

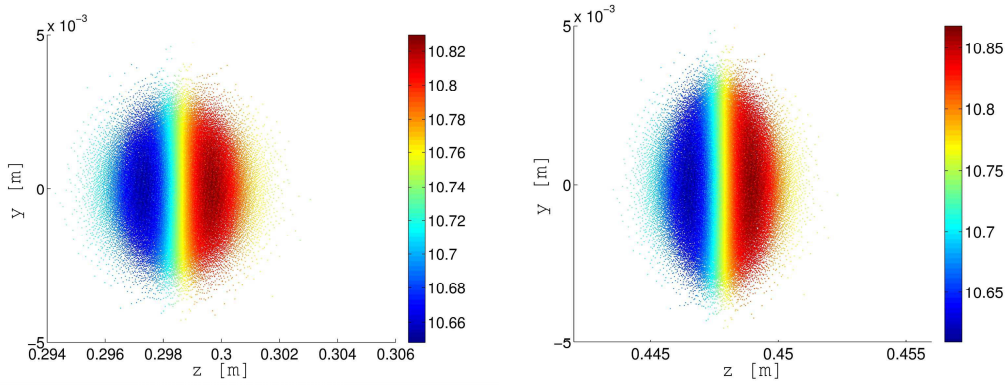


Figure 3.36: Particle and  $\gamma$  distribution after drift of the bunch for 1 ns (left) and 1.5 ns (right).

dispersion of the energy after 500 ps as result of the own space charge forces in the longitudinal direction. The energy dispersion grows along the drift as shown in Figures 3.36, 3.37 and 3.38. At the same time the particles gain transversal velocity due to the repulsive force  $F_{\perp}$  of the own  $E_{\perp}$  field which is  $\gamma$  times stronger than the transverse field in the rest frame. Equation (2.70) shows that the transverse repulsive force is  $\gamma$  times smaller than the repulsive force in the rest frame of the bunch. However since for the kinetic energy of 5 MeV  $\gamma$  has a value around 10 there will be still transversal motion of the bunch particles due to the own space charge force. Figures 3.39 and 3.40 show the development of the vertical particle velocity along the drift. Since the bunch and beam pipe are cylindrically symmetric the same values of the velocity are achieved in the horizontal direction.



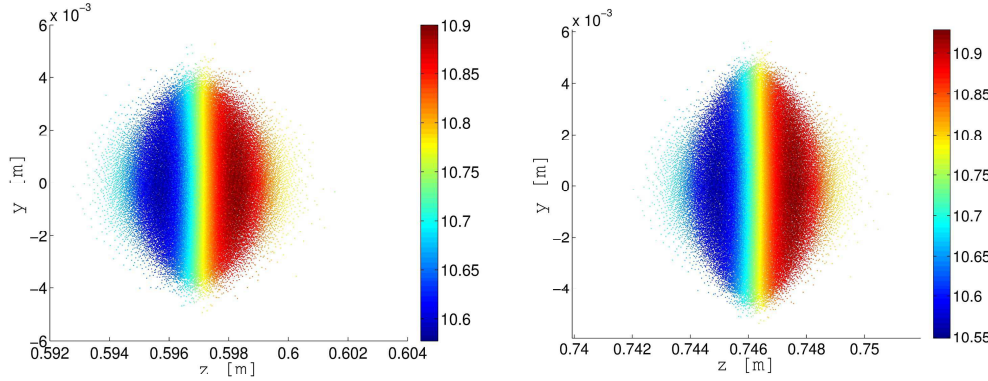


Figure 3.37: Particle and  $\gamma$  distribution after drift of the bunch for 2 ns (left) and 2.5 ns (right).

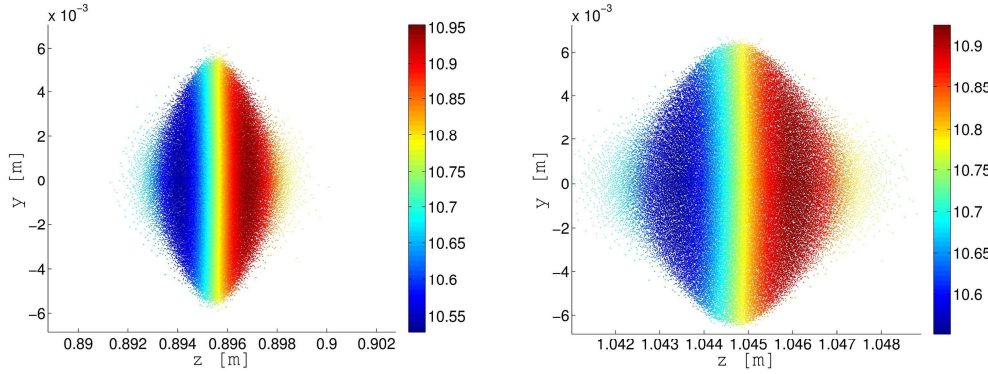


Figure 3.38: Particle and  $\gamma$  distribution after drift of the bunch for 3 ns (left) and 3.5 ns (right).

After the bunch expanded in transverse direction (Fig. 3.38) the own space charge force becomes weaker. Hence the transversal velocity growth saturates as it could be seen by comparing the  $v_y$  velocity plots in Figure 3.39 and 3.40 made in time steps of 1 ns.

The same bunch was also tracked in a circular beam pipe with radius of only 5 mm. As expected during the drift of 3.5 ns the particles of the bunch expanding in the transverse plane reached the wall where they were reflected with the same incidence angle as shown in Fig. 3.41 (left). If no other forces act on a particle after the reflection it retains its momentum and changes only its direction of motion as shown at the sketch in Fig. 3.41 (right).

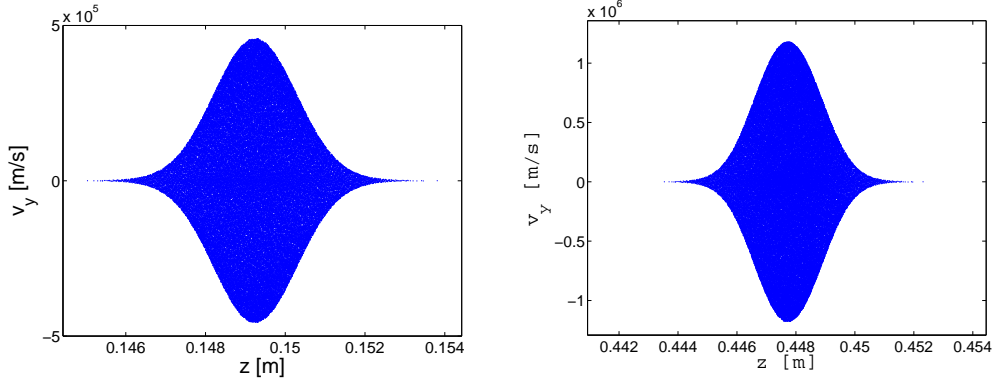


Figure 3.39: Vertical velocity  $v_y$  distribution after drift of the bunch for 500 ps (left) and 1.5 ns (right).

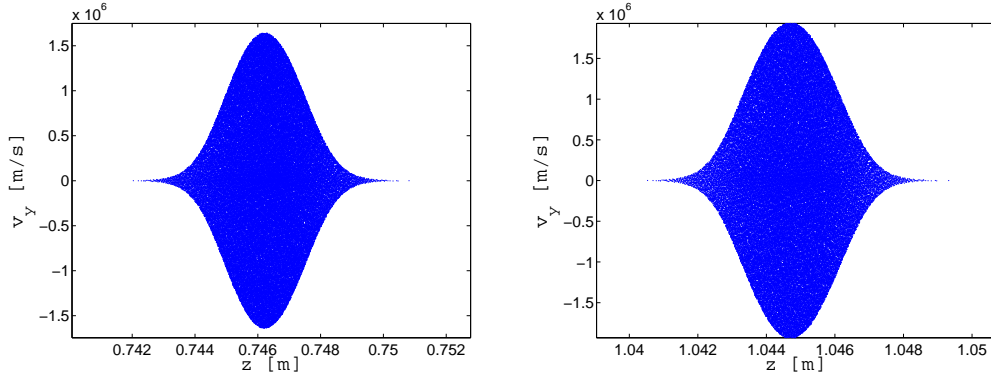


Figure 3.40: Vertical velocity  $v_y$  distribution after drift of the bunch for 2.5 ns (left) and 3.5 ns (right).

### 3.6.2 Comparison of MOEVE PIC Tracking with other PIC Programs

In order to verify the results from MOEVE PIC Tracking an extensive comparison of the results was made with the tracking program Astra [Flöttmann 2000] (used at DESY for simulations for the European XFEL [DES 2012a] and the free-electron laser facility FLASH [DES 2012b]) as well as with the widely used commercial program "General Particle Tracer"-GPT [van der Geer] from Pulsar Physics. Here the drift simulation described in the previous section is used to compare certain simulation results of the three programs. The computation of the own space charge field with Astra and GPT is done with open, whereas MOEVE PIC Tracking uses a PEC beam pipe boundary conditions. Hence the difference in the boundary conditions

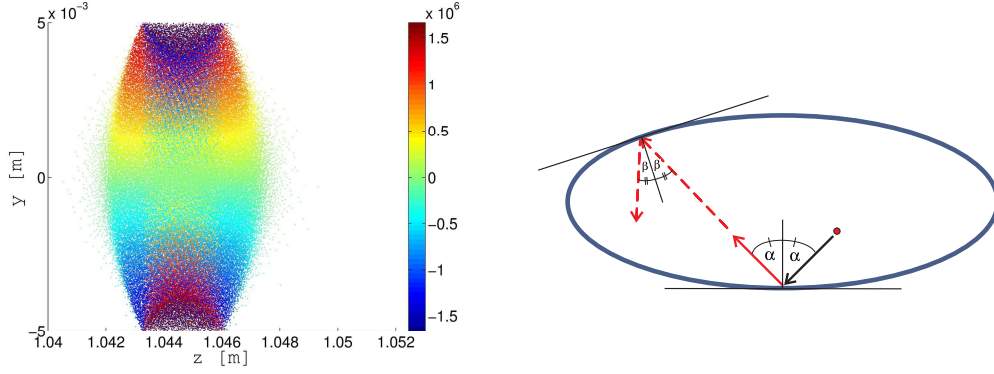


Figure 3.41: The color bar represents the vertical velocity  $v_y$  distribution after drift of the bunch of 3.5 ns in a beam pipe of 5 mm radius (left). Principle sketch of the particle reflection from the wall in the transversal plane (right).

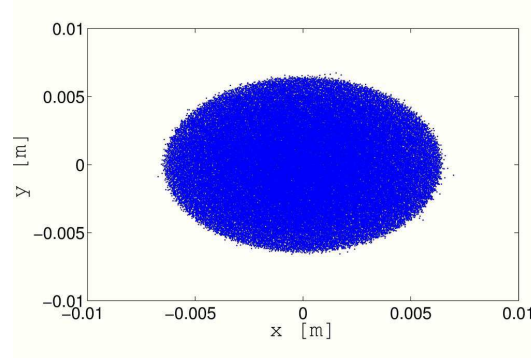


Figure 3.42: Transverse charge distribution of the bunch after the drift of 3.5 ns computed with MOEVE PIC Tracking.

explains the differences in the bunch transverse size shown in Fig. 3.42 and 3.43. The comparison in Fig. 3.19 shows that the own transverse field of the bunch computed in a beam pipe is generally higher than the one computed with open b.c.. As a consequence the bunch transverse size as a result of MOEVE PIC Tracking (Fig. 3.42) is larger compared with the transverse size computed with Astra or GPT (3.43).

Figures 3.45 and 3.45 plot the corresponding vertical phase space distribution of the bunch. The comparison with GPT of the vertical velocity (as a fraction of the light velocity) Fig. 3.45 and with Astra (eV/c) Fig. 3.45.

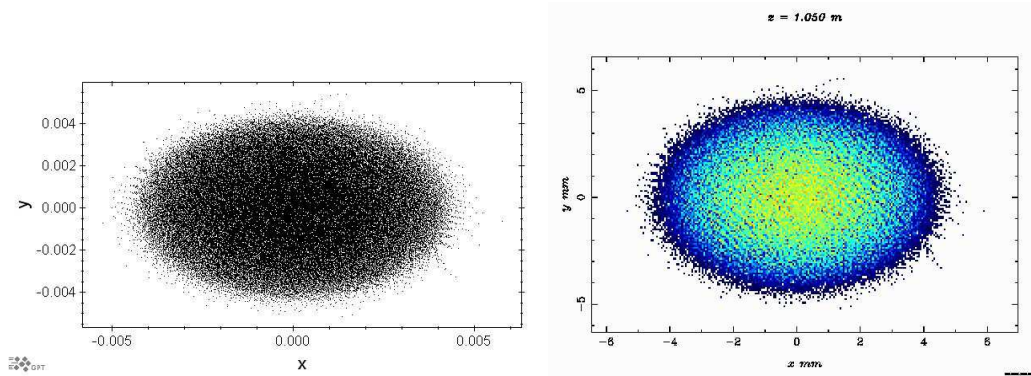


Figure 3.43: Transverse charge distribution of the bunch after the drift of 3.5 ns computed with GPT (left) and Astra (right).

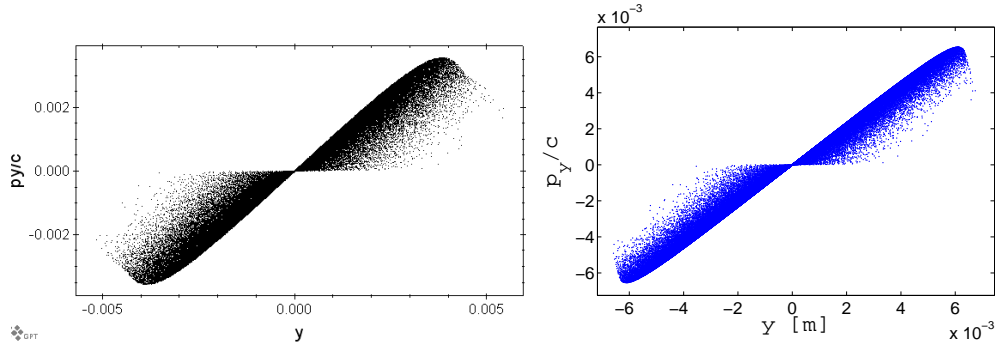


Figure 3.44: Vertical momentum distribution after a drift of 3.5 ns computed with GPT (left) and MOEVE PIC Tracking (right).

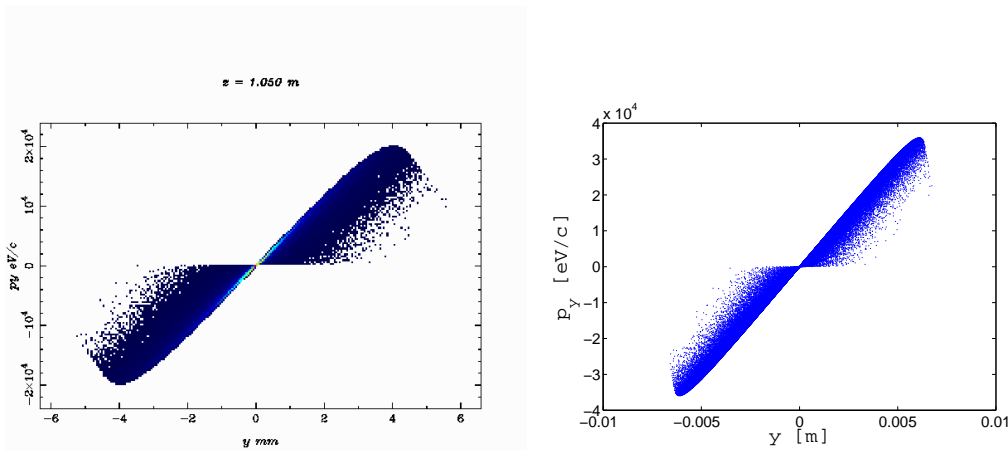


Figure 3.45: Vertical momentum distribution after a drift of 3.5 ns computed with Astra (left) and MOEVE PIC Tracking (right).

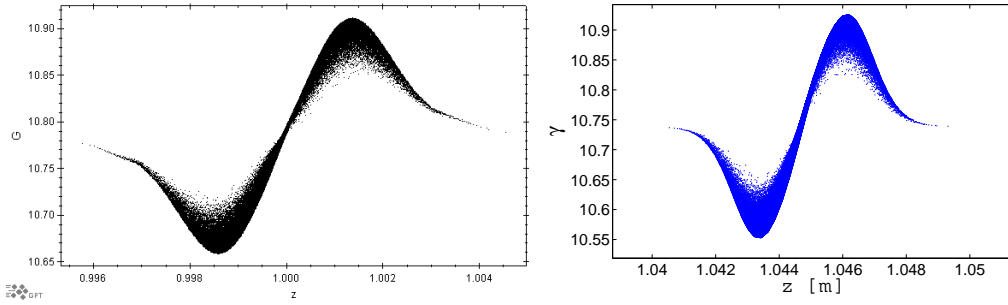


Figure 3.46: Lorentz factor distribution of the bunch after the drift of 3.5 ns computed with GPT (left) and MOEVE PIC Tracking (right).

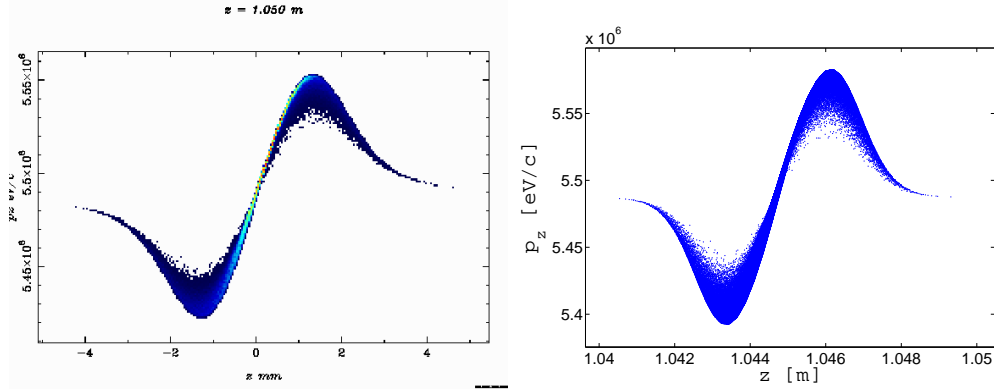


Figure 3.47: Distribution of the longitudinal momentum of the particles after the drift of 3.5 ns computed with Astra (left) and MOEVE PIC Tracking (right).

The longitudinal energy spread due to the own space charge forces in the bunch is given through the Lorentz factor distribution in Fig. 3.46. The results of GPT and MOEVE PIC Tracking simulation show a very good agreement. Fig. 3.47 gives a comparison of the longitudinal momentum in eV/c computed by Astra and MOEVE PIC Tracking. Also these results are qualitatively as well as in the spread in a very good agreement.



# Interaction of a Positively Charged Bunch with an Electron Cloud

---

## Contents

<b>4.1</b>	<b>3D self-consistent PIC Simulation of the Interaction</b>	<b>81</b>
4.1.1	Interaction Forces . . . . .	83
<b>4.2</b>	<b>Simulation Studies . . . . .</b>	<b>84</b>
4.2.1	Bunch Particles . . . . .	84
4.2.2	Electron Cloud Particles . . . . .	86
4.2.3	Interaction in a Dipole Field . . . . .	92

---

The particle in cell program MOEVE PIC Tracking was introduced in the previous chapter. An example of a single bunch tracking with an initial momentum of 5 MeV under the influence of the own space charge forces was discussed and compared with other PIC programs. Beyond that, the program is designed to simulate the interaction of two particle species i.e. a relativistic bunch and a non-relativistic particle cloud. This chapter treats the simulation of the interaction in function of the estimation of single bunch instability due to the presence of electron clouds in a storage ring accelerator machine. The results of the simulations presented here are referring to positron beams, however the program can also be used for simulating the interaction of proton beams with electron clouds.

## 4.1 3D self-consistent PIC Simulation of the Interaction

In MOEVE PIC Tracking the bunch and the cloud are each represented by a 3D distribution of macro-particles in a vacuum bounded by a PEC beam

pipe with elliptical cross-section. The macro-particles are defined in the six-dimensional phase space  $\Psi(x, p_x, y, p_y, z, p_z)$  and typical values of their number are of order  $10^6$  for both species. Usually the bunch particles have a Gaussian spatial distribution. The cloud particles are assumed to be homogeneously spread in 3D space with a certain length in longitudinal direction and bound by the beam pipe in the transverse plane. The interaction is simulated during the bunch passage through the e-cloud. Figure 4.1 shows the longitudinal profile of the bunch (blue) during it's passage through the 3D electron distribution (red).

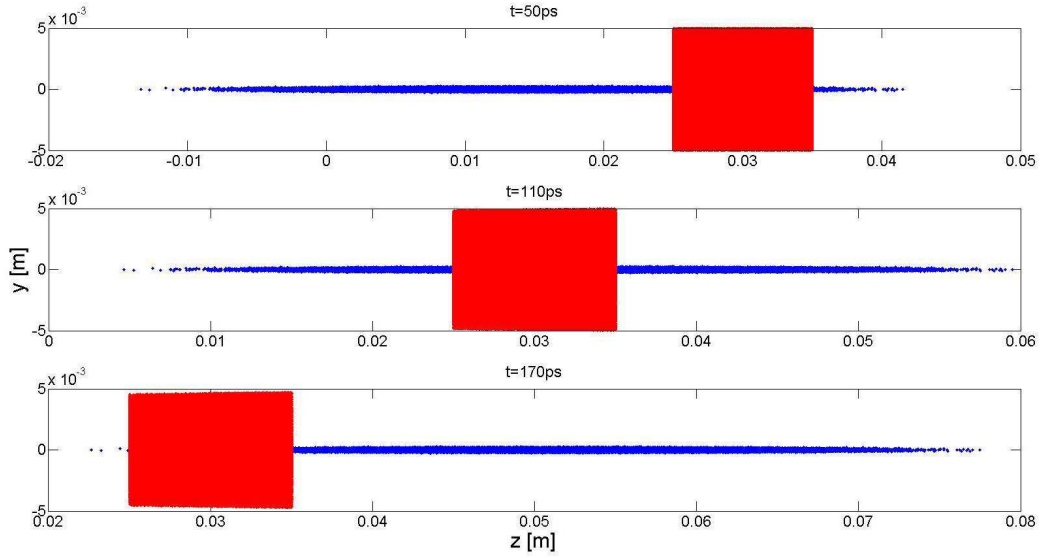


Figure 4.1: Longitudinal profile of a bunch and the e-cloud, during the passage of the bunch through the cloud.

In a drift section, only the self fields of the beam and the e-cloud act on both particle species. Beside the strong transversal electrical field  $\mathbf{E}_b$ , the beam, being highly relativistic  $\mathbf{v}_b \approx c$ , evokes also a strong transversal magnetic field  $\mathbf{B}_b = (\mathbf{v}_b \times \mathbf{E}_b)/c^2$  whereas the e-cloud provides only its own space-charge field  $\mathbf{E}_e$ . Consequently, in order to integrate the trajectory of both species it is necessary to compute the electrical fields of the beam  $\mathbf{E}_b$  and of the e-cloud  $\mathbf{E}_e$ . The time integration of the particle trajectory is computed for a discrete time step with typical values of  $dt = 1$  ps. Before the particles are pushed, following algorithmic steps are performed at every time step of the simulation:

- Definition of the 3D laboratory frame grids for the distributions of the



bunch and the cloud which is followed by weighting the particle charge on the grid nodes as an input for the discretized Poisson equation.

- The computation of the Poisson equation for the ultra-relativistic bunch takes place at its center-of-mass system. Practically, the defined laboratory frame grid is stretched in longitudinal direction by the Lorentz factor  $\gamma$ . The grid Poisson equation for the e-cloud is solved at the laboratory frame grid. Hence, two separate computations of the grid Poisson equation for both species are performed in parallel.
- Back at the laboratory frame, the grid fields  $\mathbf{E}_b$  and  $\mathbf{E}_e$  are interpolated on each particle position in space and optionally superposed with external fields, if present.

Once the forces are computed for every macro-particle of the bunch and of the cloud, their trajectories will all be pushed by the leap-frog method for one time step  $dt$ . The total simulated time equals the time which the bunch needs to cross the thickness of the defined e-cloud.

#### 4.1.1 Interaction Forces

In order to additionally speed up the time integration in a drift space, for both species, the equation of motion could be rationalized as follows:

- For beam energies of GeV order, according to equation (2.70), the own magnetic and electric forces (displayed in Figure 2.14) cancel each other. Hence the only force that affects the bunch particles  $\mathbf{F}_b$  is the space-charge force of the e-cloud:

$$\mathbf{F}_b = q(\cancel{\mathbf{E}_b} + \mathbf{E}_e + \cancel{\mathbf{v}_b \times \frac{\mathbf{v}_b \times \mathbf{E}_b}{c^2}}).$$

- The electrons experience their own and the space-charge forces of the beam. Due to the attractive force of the bunch the electrons are accelerated in the transversal plane. However, the velocities which most of the electrons reach, relative to the velocity of light, are small enough (approximately  $|\mathbf{v}_e| \approx 0.01c$ ) so that the part of the Lorentz force due to the magnetic field of the beam could be neglected:

$$\mathbf{F}_e = q(\mathbf{E}_b + \mathbf{E}_e + \cancel{\mathbf{v}_e \times \frac{\mathbf{v}_b \times \mathbf{E}_b}{c^2}}).$$

Neglecting the rotation of the particles due to the magnetic field of the beam speeds up the simulation in a drift space whereas the interaction simulation in a beam guiding magnet still requires to take into account the rotation due to the external magnetic force.

## 4.2 Simulation Studies

Detailed simulations of the interaction between the beam and the electrons give the possibility to evaluate their behavior and thus to understand the dynamics and the nature of the e-cloud effect on the beam. In the following, simulation results are presented of a symmetrical passage of a positron bunch through a homogeneous e-cloud in a beam pipe of a circular cross section. The total time simulated is 250 ps with a time step of  $dt = 1$  ps. The bunch corresponds to the beam parameters of the KEKB low energy positron ring (KEKB-LER [Funakoshi 2001]) given in Table A.2. The e-cloud density is  $\rho_e = 10^{12} N_e/\text{m}^3$ . The bunch is represented by  $10^6$  macro-particles and there are  $0.4 \cdot 10^6$  single electrons in the 10 mm thick e-cloud slab. Here

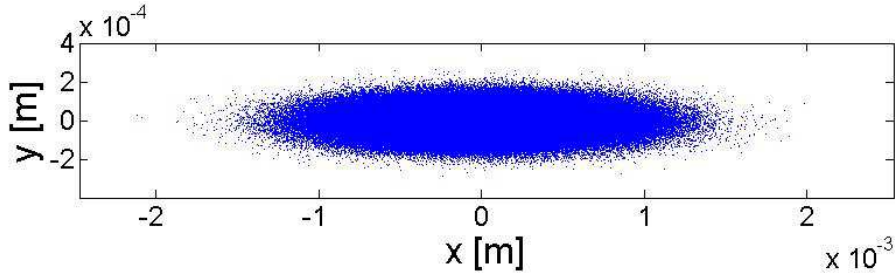


Figure 4.2: Transversal profile of the KEKB bunch. The rms beam sizes ratio is  $\sigma_x/\sigma_y = 7$ .

it should be pointed out that in modern high energy particle accelerators, regardless of their use, the transversal beam profile is flat<sup>1</sup>(Figure 4.2), typically characterized by a ratio of the rms beam sizes  $\sigma_x/\sigma_y > 5$ . As a result the transverse field of the beam in the vertical direction is stronger which also means a stronger interaction with the e-cloud in that direction. Thus, in the following the properties of the bunch and the e-cloud are discussed for the vertical direction since the effects which may lead to a beam instability are more pronounced in that direction.

### 4.2.1 Bunch Particles

The initial transversal velocity  $(v_x, v_y)$  of the bunch particles at the beginning of the interaction has been set to zero. Figures 4.3, 4.4, 4.5, 4.6 plot the vertical velocity  $v_y$  of the bunch particles as the bunch passes through the e-cloud. The e-cloud extends longitudinally between the vertical lines depicted

<sup>1</sup>In a collider machine to increase the luminosity and in a synchrotron light sources to achieve higher brilliance.

in Figures 4.3–4.6. Due to the symmetry of the setup bunch–e-cloud, in the transversal plane the distribution of the transversal momentum of the bunch particles during the interaction is also symmetrical. The median value of  $v_y$  along the bunch length is practically zero at any moment during the interaction. Thus, the overall transverse effect which may lead to a single bunch instability due to the interaction with the e-cloud is zero. However this symmetrical setup is a rather idealized representation of the interaction, in reality the longitudinal parts of the bunch are not aligned symmetrically in the transversal plane. The related effects will be treated in the following chapter. Figure 4.3 left shows that at the beginning of the interaction the particles from

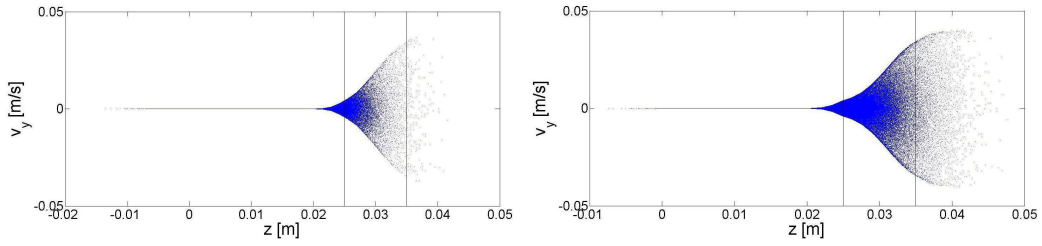


Figure 4.3: Transversal velocity ( $v_y$ ) of the bunch particles during the passage through the e-cloud, after 50 ps (left) and 70 ps (right).

the head of the bunch receive a linear increase of the absolute vertical velocity. This is due to the radial attraction from the more or less still homogeneously spread electrons starting to gain transversal velocity towards the beam axis. As the bunch passes through, the electron density in the vicinity of the beam axis starts growing and so the dispersion of the transversal velocity reduces as shown in Figure 4.3 right and Figure 4.4 especially in the right plot at 110 ps.

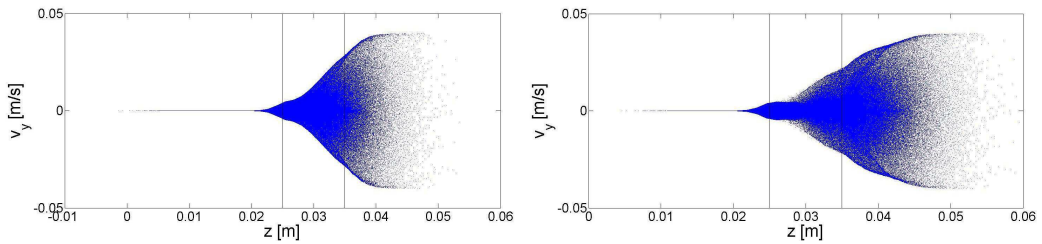


Figure 4.4: Transversal velocity ( $v_y$ ) of the bunch particles during the passage through the e-cloud, after 90 ps (left) and 110 ps (right).

However, even though still in the strong attracting field of the bunch  $\mathbf{E}_b$  the electron density near the beam axis starts decaying due to the own repulsive

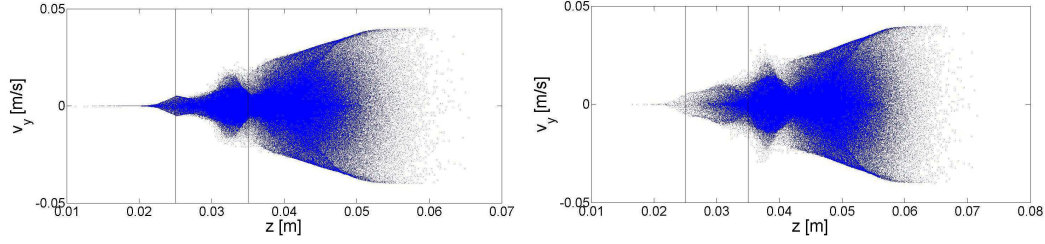


Figure 4.5: Transversal velocity ( $v_y$ ) of the bunch particles during the passage through the e-cloud, after 130 ps (left) and 150 ps (right).

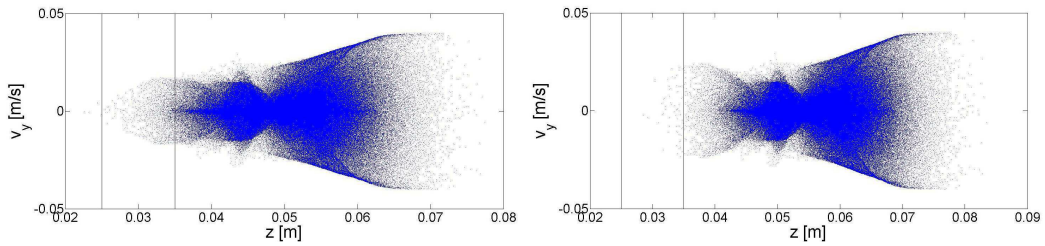


Figure 4.6: Transversal velocity ( $v_y$ ) of the bunch particles during the passage through the e-cloud, after 170 ps (left) and 190 ps (right).

space charge field  $\mathbf{E}_e$ . Even more, the electron density starts oscillating due to the still present potential of the bunch and the newly arriving electrons initially positioned at higher radii in the transverse plane. These oscillations are evident in the beam's vertical velocity spread along the length of the bunch shown in Figures 4.5 and 4.6.

#### 4.2.2 Electron Cloud Particles

During the bunch passage, the single electrons, depending on their initial position, could perform an aperiodic or a periodic motion:

- Figures 4.7–4.10 represent the vertical phase space of the initially static electrons during the bunch passage. The electrons from the periphery are attracted to the bunch centroid position. As it can be seen from the contour of the distribution in Figures 4.7, 4.8 and 4.9 the more they approach the beam axis the more energy they win due to the non-linear bunch potential. Those electrons accumulated enough energy to cross the beam axis at  $y = 0$  despite the bunch potential which may be also weaker as the bunch passes in longitudinal direction. Nevertheless, as shown in Figures 4.8 and 4.9, if those electrons are still in the attracting field of the bunch they will loose some of their velocity on their way

to hit the chamber wall on the opposite side. Figure 4.10 shows the development of the e-cloud shortly after the bunch passage. Basically the electrons continue their motion with the momentum which they received from the bunch. Since there are still electrons heading towards the beam axis, the e-cloud density near the beam axis slowly decreases which on the other hand decelerates those electrons elastically reflected from the vacuum chamber wall as shown in the right plot of Figure 4.10.

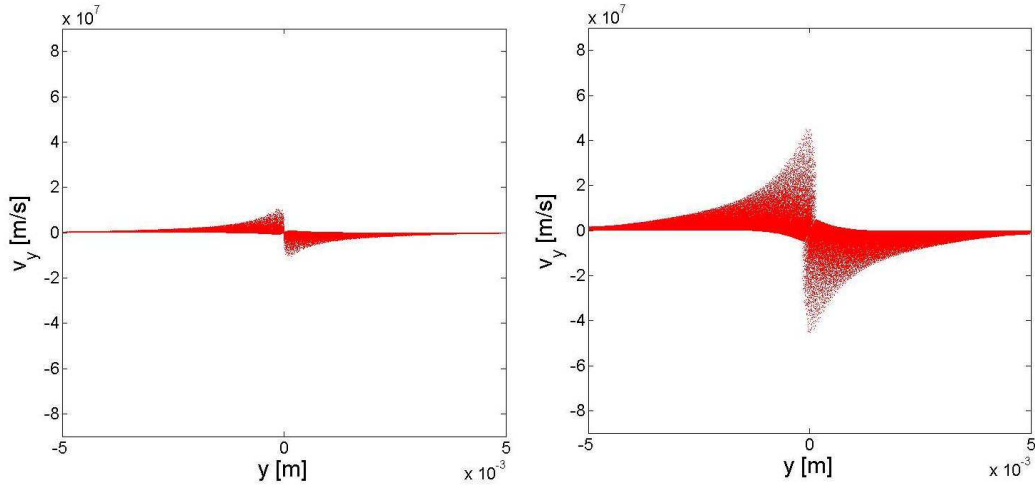


Figure 4.7: Phase space distribution of the electrons in vertical direction after 50 ps (left) and 70 ps (right)

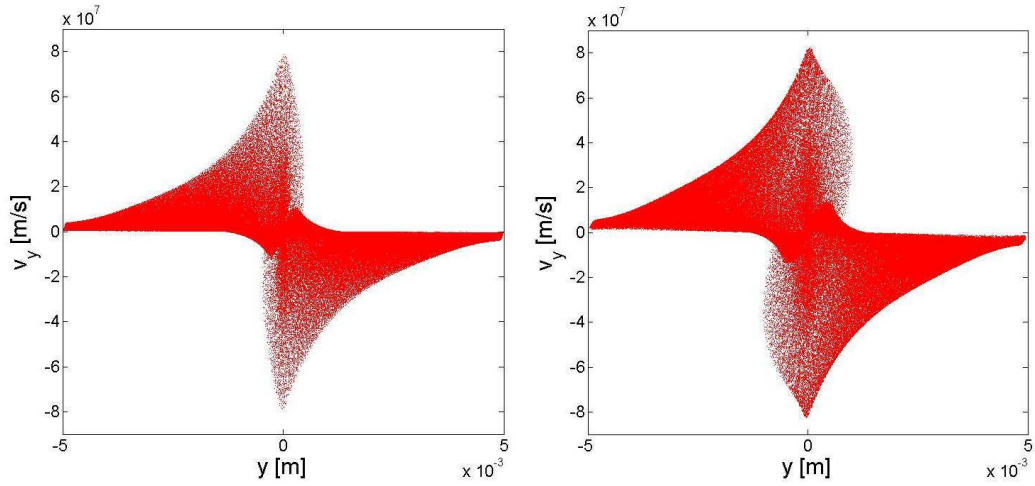


Figure 4.8: Phase space distribution of the electrons in vertical direction after 90 ps (left) and 110 ps (right).

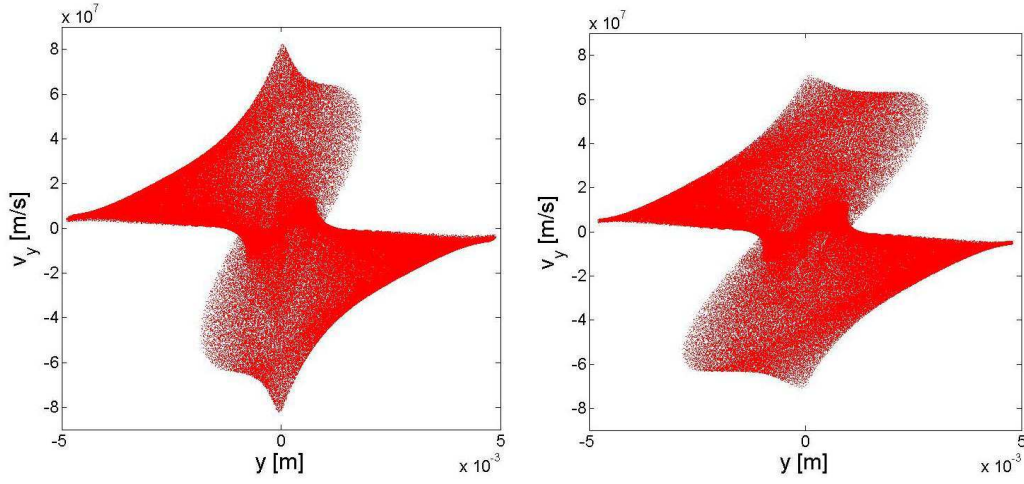


Figure 4.9: Phase space distribution of the electrons in vertical direction after 130 ps (left) and 150 ps(right).

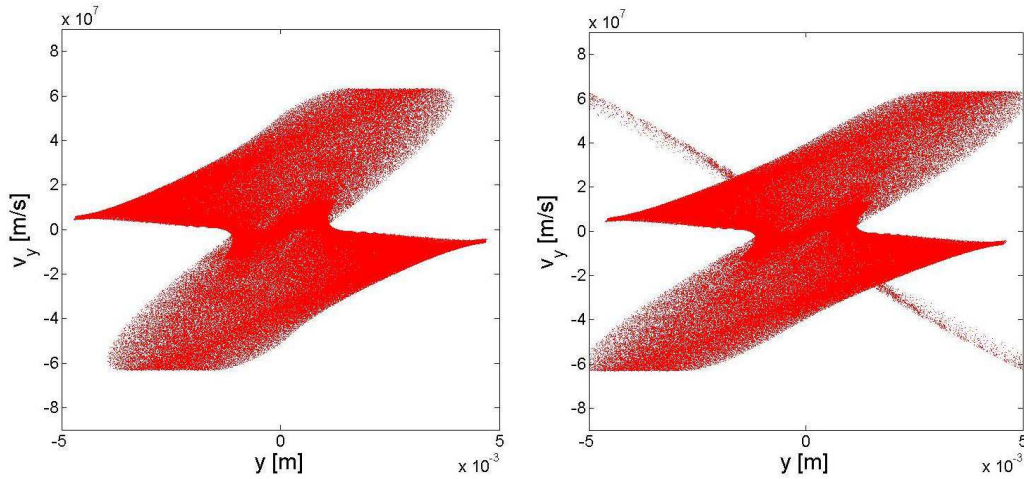


Figure 4.10: Phase space distribution of the electrons in vertical direction after 170 ps (left) and 190 ps (right).

- On the other hand, the fine resolution of the time discretization allows to monitor the oscillations of the electrons near the beam axis. Figure 4.11 displays the transversal trajectories of several electrons during the bunch passage. The electrons are initially positioned in the same transversal plane on different locations around the beam. The transversal profile of the beam is plotted in Figure 4.11 as well. Except for the electron placed exactly on the beam axis at (0,0) (straight blue line) the electrons oscillate around the beam axis. The amplitude and the frequency of the



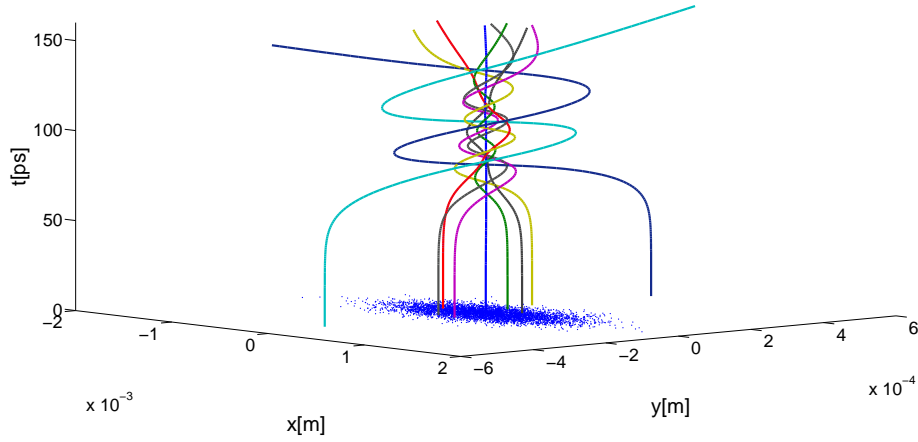


Figure 4.11: Electrons oscillating in the potential of a short positron bunch whose transversal profile is displayed in the  $(x, y)$  plane.

oscillation both depend on the longitudinal charge profile of the bunch but also on the initial position of the electrons. Figure 4.12 shows the oscillation of a particle initially positioned at  $(0, \sigma_y)$  (green line) and of two other particles below and above the beam axis at positions  $(0, \pm 7.5\sigma_y)$ . The particle starting at  $(0, \sigma_y)$  inside the beam profile performs oscillations with a period of  $T = 28$  ps (Figure 4.13). The angular frequency  $\omega = 2.244 \cdot 10^{11} \text{ rad} \cdot \text{s}^{-1}$  is comparable with  $\omega_{e,y} = 2.2008 \cdot 10^{11} \text{ rad} \cdot \text{s}^{-1}$  - the value computed with the expression given in [Ohmi 2001c] for electron oscillations in a potential of a coasting beam<sup>2</sup>:

$$\omega_{e,x(y)} = \left( \frac{2\lambda_b r_e c^2}{\sigma_{x(y)}(\sigma_x + \sigma_y)} \right)^{1/2}. \quad (4.1)$$

Thereby the line density of the bunch with  $N_b$  positrons is given by  $\lambda_b = N_b/2\sigma_z$ ,  $\sigma_{x(y)}$  is the horizontal (vertical) beam size (corresponding values in Table A.2),  $r_e$  is the classical electron radius and  $c$  the speed of light. However, expression (4.1) is an idealization not only because of the fact that the longitudinal charge profile of the bunch has a rather Gaussian distribution but also because it does not take into account the own space charge force of the electrons. Namely, while the electron concentration in a very small space grows, the repelling own space-charge

<sup>2</sup>The charge distribution of the beam is taken to be uniform in the longitudinal direction.

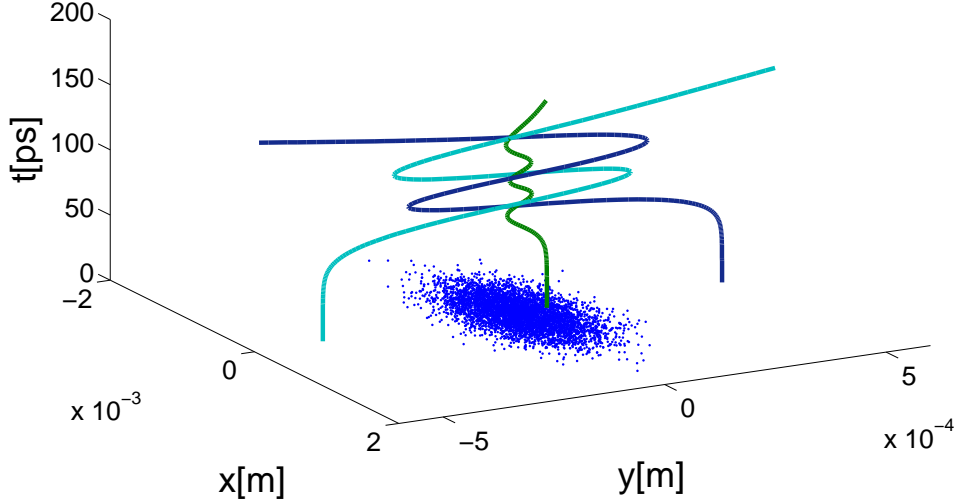


Figure 4.12: Oscillations of electrons in the potential of the beam. The electrons are initially positioned at  $(0, \sigma_y)$  (green line) and  $(0, \pm 7.5\sigma_y)$  (blue and turquoise line).

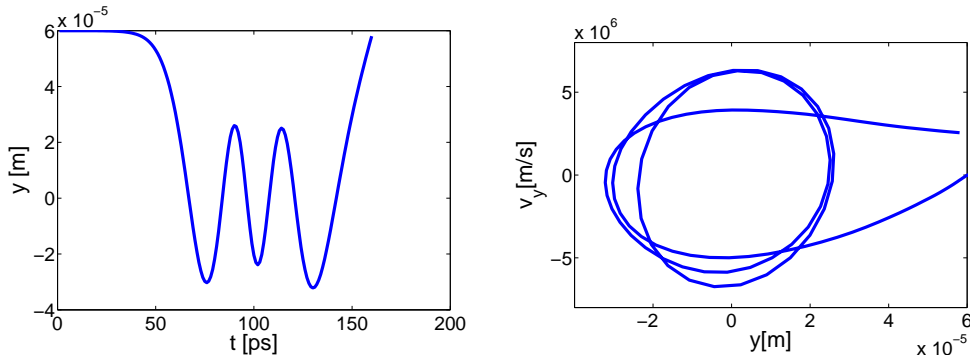


Figure 4.13: Oscillation in the vertical plane during the passage of the bunch (left). The electron is initially placed at  $(0, \sigma_y)$ . Vertical phase-space plot of the same oscillation (right).

force prevails over the beam attractive force and the electrons start to disintegrate. Hence the oscillations of the particles are also influenced by the electron density near the beam axis which changes during the bunch passage.

On the other hand, the overall e-cloud density near the beam axis is made up of the oscillatory electrons and the faster aperiodic electrons which constantly



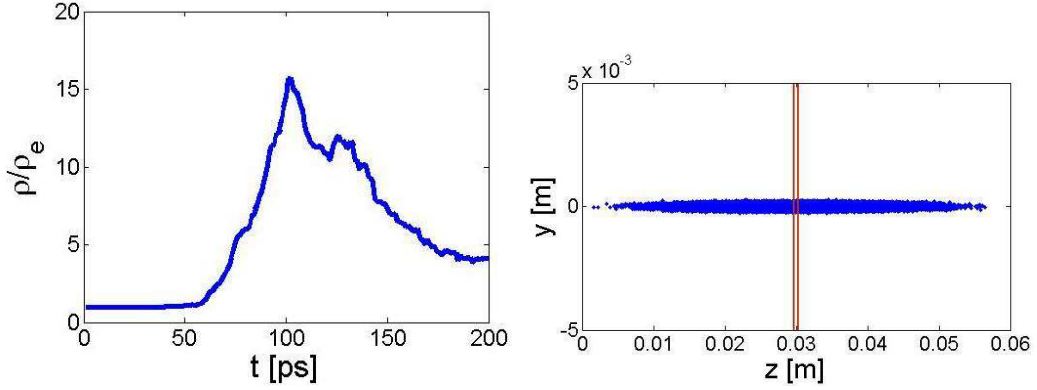


Figure 4.14: Electron density during the bunch passage (left) in a cuboid with transverse sides  $2\sigma_x$  and  $2\sigma_y$  of the bunch and length of 0.6 mm as designated between the red lines on the right.

arrive on the beam axis. Figure 4.14 (left) displays the overall density of the electrons during the bunch passage in a cuboid with transverse sides  $2\sigma_x$  and  $2\sigma_y$  of the bunch and a length of 0.6 mm as designated between the red lines in the right plot of the figure. The peak of the electron density at 100 ps corresponds to the bunch position shown on the right part of Figure 4.14. Hence, the peak of the e-cloud density matches with the maximum of the bunch's longitudinal charge profile. Later, as the longitudinal charge density of the bunch and with it its transverse potential decline, the e-cloud density starts to decline as well. However, due to the arrival of electrons attracted from more distant transverse positions and due to the electron oscillations the decline of the electron density  $\rho$  in the volume is not steady.

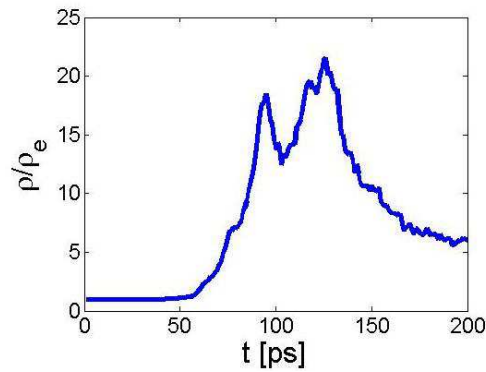


Figure 4.15: Electron density during the bunch passage in a cuboid with transverse sides  $\sigma_x$  and  $2\sigma_y$  of the bunch and length of 0.6 mm as designated between the red lines in Figure 4.14 (right).

Figure 4.15 shows the electron density  $\rho$  in a similar cuboid with smaller horizontal width of  $\sigma_x$  ( $[-\sigma_x/2, \sigma_x/2]$ ). The two peaks in Figure 4.15 are evidence of the oscillation of the electrons near the beam axis. An indication of these e-cloud density peaks around the beam axis can be also observed in Figures 4.4 and 4.5, where the spread of the transversal momentum of the bunch particles at 110 ps and 130 ps at  $z=0.03$  m is minimal. Since the electron dynamics in a drift space is almost entirely in a transverse plane the longitudinal parts of the bunch see the same electron density along their way across the e-cloud. Thus, after interacting with the whole length of the e-cloud the bunch features those two waists in the vertical velocity distribution (as shown in Figure 4.5 at 150 ps and later) that correspond to the maxima in the e-cloud density near the beam axis.

### 4.2.3 Interaction in a Dipole Field

The interaction can be simulated in a drift section or in a section with an external magnetic field which models the guiding magnets (dipoles, quadrupoles etc.). Here the particular interest is in the interaction within a dipole magnet. Due to the attractive force of the positron bunch, the electrons receive a transverse velocity towards the beam axis. The scatter plots in Figure 4.16 show the transverse components of the electron velocity at  $t=100$  ps of the interaction inside of a drift section. In a dipole field of  $B_{y0} = 1$  T, the elec-

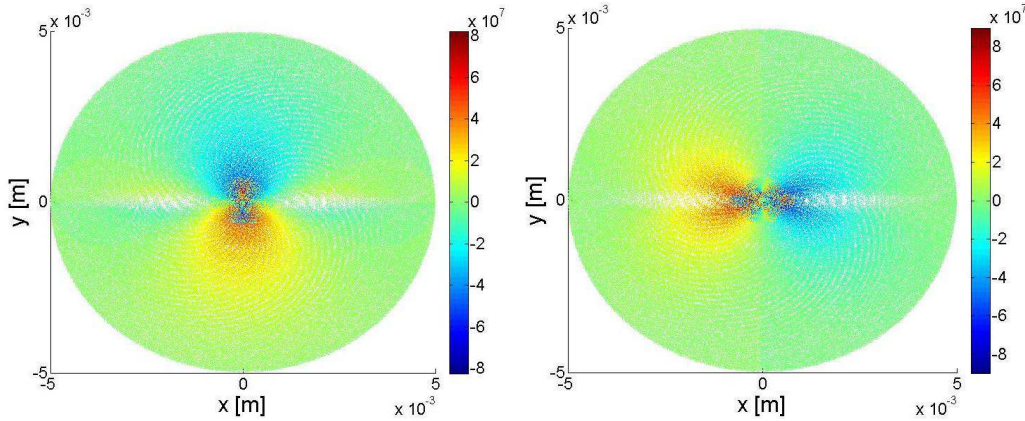


Figure 4.16: Vertical (left) and horizontal (right) component of the electron velocity in [m/s] at  $t=100$  ps from the interaction inside a drift section.

trons with transverse velocity  $\mathbf{v}$ , due to the  $\mathbf{v} \times B_{y0}$  part of the Lorentz force, additionally receive a longitudinal component of the velocity  $v_z$ . In return, the horizontal component becomes weaker as shown in Figure 4.17 right. Figure 4.18 displays  $v_z$  of the particles along the  $x$  direction during the interaction

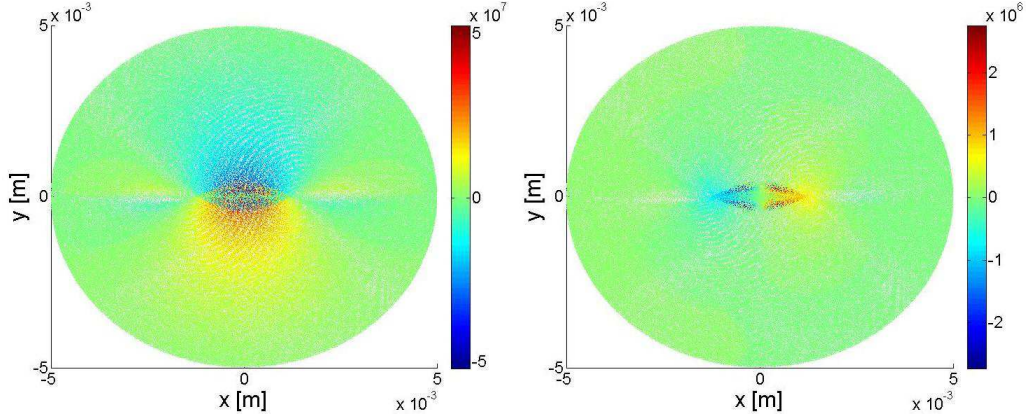


Figure 4.17: Vertical (left) and horizontal (right) component of the electron velocity in [m/s] at  $t=100$  ps from the interaction in a dipole field  $B_{y0} = 1$  T.

in the dipole field. At  $t=70$  ps the  $v_x$  component of the electrons left and right of the beam axis is directed to  $y = 0$  which results in the longitudinal  $v_z$  distribution as presented in the left plot of Figure 4.18. At  $t=170$  ps many electrons already crossed the  $y = 0$  line while others are still heading towards the beam axis which results with  $v_z$  distribution as shown on the right plot of Figure 4.18.

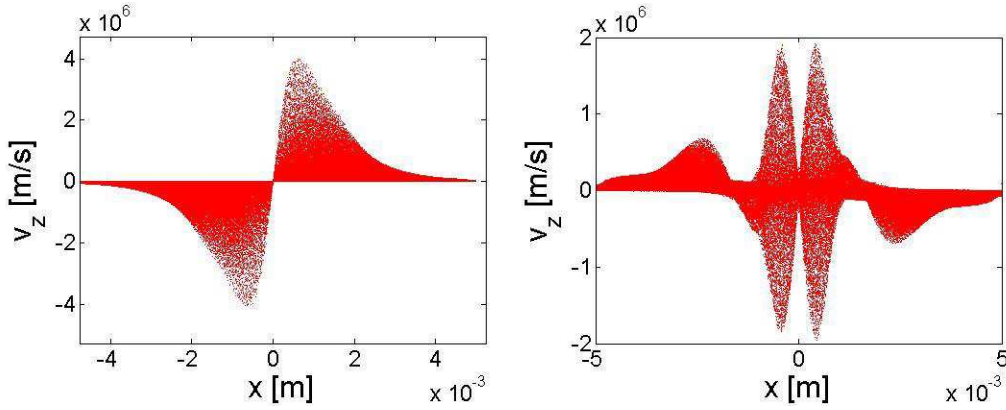


Figure 4.18: Longitudinal velocity of the electrons along the  $x$ -axis during the bunch passage in  $z$ -direction at  $t=70$  ps (left) and  $t=170$  ps (right).

The actual longitudinal motion of the electrons from one slice of the e-cloud during the interaction is shown in Figure 4.19. In a drift space, the electrons perform practically no longitudinal motion (Figure 4.19, left) whereas in the dipole field the longitudinal motion is strongest on both sides of the beam in  $x$  direction (Figure 4.19, right). That clearly indicates the build up of

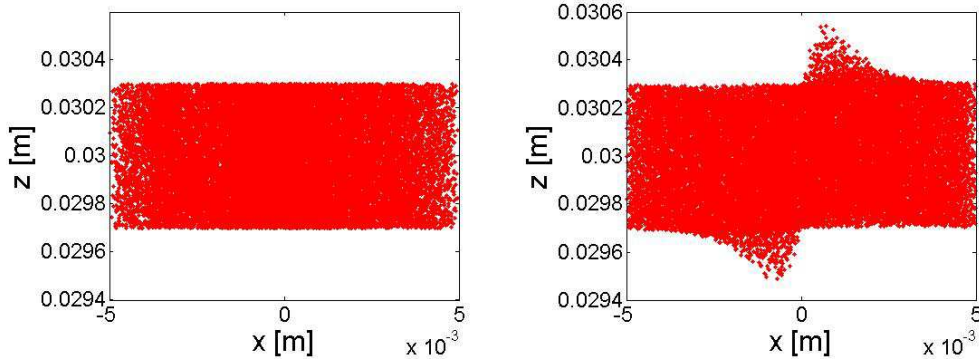


Figure 4.19: Distribution of electrons after a bunch passage in  $z$ -direction: in a drift section (left) and in a dipole field along  $y$ -direction (right).

two vertical stripes of higher electron density in the transverse plane during the bunch passage through the initially homogeneous e-cloud. Indeed, the electron distribution in a transversal plane immediately after interacting with the bunch in the dipole (Figure 4.20) shows that development.

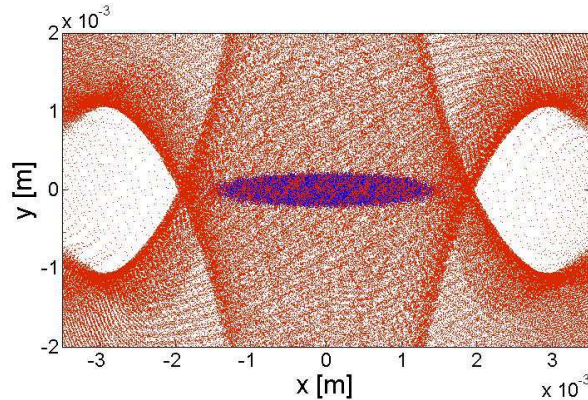


Figure 4.20: Electron distribution in a transversal plane after interacting with the bunch in a dipole field.

While the maximum density of the e-cloud during the interaction inside a drift is always located at the beam axis (Figure 4.21) the e-cloud density at the beam axis during the interaction in a dipole field is very moderate as shown in Figure 4.22.

The e-cloud concentration in vertical stripes left and right of the beam axis in a dipole magnet could lead to coupling of the vertical betatron motion with the synchrotron motion of the bunch particles. Having in mind that due to the energy dispersion the bunch particles in a dipole field have different radius of curvature it is obvious that the particles with less energy could

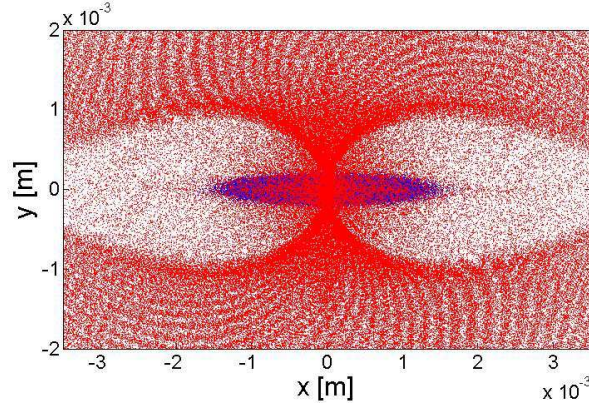


Figure 4.21: Electron distribution in a transversal plane after interacting with the bunch in a drift space.

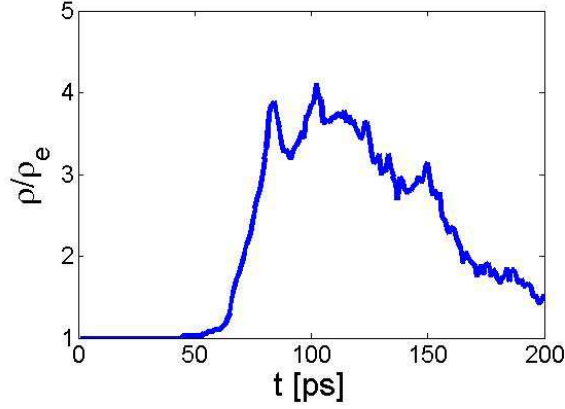


Figure 4.22: Electron density during the bunch passage inside a dipole magnet. The density is computed for a cuboid with transverse sides of  $2\sigma_x$  and  $2\sigma_y$  of the bunch and length of 0.6 mm (as defined in Figure 4.14).

interact with the electrons from the inner stripe, whereas the particles with higher energy have a larger radius and so they may interact with the outer vertical stripe of electrons. In the KEKB-LER a synchro-betatron sideband signal was measured due to electron clouds [Flanagan 2005].





# Numerical Estimation of Electron Cloud Effects on a Single Bunch

---

## Contents

---

<b>5.1</b>	<b>Coherent Tune Shift due to an Electron Cloud . . . .</b>	<b>98</b>
5.1.1	Betatron Tune . . . . .	98
5.1.2	Numerical Computation of the Tune Shift . . . . .	100
5.1.2.1	Computational Studies . . . . .	101
<b>5.2</b>	<b>Incoherent Effects of Electron Clouds . . . . .</b>	<b>103</b>
5.2.1	Head - Tail Simulation with Vertically Displaced Parts of the Bunch . . . . .	104
5.2.2	Wake Field induced by Electron Cloud . . . . .	107
<b>5.3</b>	<b>Two-Variable Wake Field induced by an Electron Cloud</b>	<b>110</b>
5.3.0.1	Two-Variable Wake Field induced by an Elec- tron Cloud in KEKB-LER and ILC $e^+$ DR . . . . .	111
<b>5.4</b>	<b>Tracking with a Pre-Computed Wake Matrix . . . . .</b>	<b>113</b>
5.4.1	Properties of the Two-Variable Wake Field . . . . .	113
5.4.1.1	Wake Function vs. Displacement . . . . .	114
5.4.1.2	Wake Function vs. Electron Density . . . . .	114
5.4.1.3	Superposition of the Wake Kicks . . . . .	116
<b>5.5</b>	<b>Single Bunch Instability . . . . .</b>	<b>118</b>
5.5.1	Tracking of a Positron Bunch in the KEKB-LER with a pre-computed Wake Matrix . . . . .	119
<b>5.6</b>	<b>Study for the PETRA III Storage Ring operated with Positron Beam . . . . .</b>	<b>120</b>

---

In storage rings operated with high positron or proton currents the number of electrons rises until a certain saturation density has been achieved. The estimated averaged density of an unperturbed e-cloud in the cross-section of a beam pipe is many orders of magnitude smaller than the positron density in

the bunch. However the results of the interaction simulations in the previous chapter demonstrated that the electron cloud, which is initially presumed as a homogeneous distribution of static electrons, changes its density in the transverse plane very fast during the passage of even a single bunch only. The rapid growth of the e-cloud density in the transversal plain around and on the beam axes depends on the parts of the bunch already passed through the specific transverse plane in longitudinal direction. In addition to the electron density growth also the centroid position of the e-cloud in the transverse plane could change very fast which may impose a dipole kick on the bunch caused by the e-cloud. This chapter presents computational studies which estimate the dipole kick from the e-cloud for different scenarios and its implications on the stability of the bunch.

## 5.1 Coherent Tune Shift due to an Electron Cloud

Measurements in positron storage rings operated with long bunch trains with short inter-bunch distances (very fertile mode to grow a considerable amount of electrons), show a betatron tune shift of the coherent dipole motion of a beam. As shown in the previous chapter, the symmetrical passage of a bunch through an initially homogeneous e-cloud leads to a symmetrical distribution of the vertical kick on the bunch particles. However, if the passage of the bunch is not symmetrical with respect to the e-cloud distribution then the vertical kick on the bunch particles will also be asymmetric. Hence the interaction of the electron cloud with the bunch results in a shift of the betatron tune of the coherent dipole motion of the beam. As the density of the electrons near the beam axis grows, its impact on the beam becomes stronger. This section presents a numerical estimation of the dipole tune shift of the beam interacting with electron clouds of different transverse size in a drift space.

### 5.1.1 Betatron Tune

The transversal tune, also called the betatron tune, represents a number of pseudo-harmonic oscillations of a particle in a transverse direction over the period of a single turn in the storage ring. As defined in the introductory chapter for the vertical direction it writes as:

$$Q_y = \frac{1}{2\pi} \oint \frac{ds}{\beta_y(s)}, \quad (5.1)$$

where  $\beta_y(s)$  is the beta function which is representing the local wavelength (at position  $s$ ) of the transverse oscillation. In the smooth focusing approx-



imation the unperturbed single particle motion is modelled as an undamped harmonic oscillator with constant wavelength given by the constant beta function  $\beta_y(s) = \bar{\beta}_y$ :

$$y'' + \left(\frac{1}{\bar{\beta}_y}\right)^2 y = 0. \quad (5.2)$$

Thus the betatron tune for unperturbed motion  $Q_{y0}$  can be obtained by dividing the circumference of the storage ring with radius  $R$  ( $2\pi R$ ) by the constant wavelength ( $2\pi\bar{\beta}_y$ ):

$$Q_{y0} = \frac{R}{\bar{\beta}_y}. \quad (5.3)$$

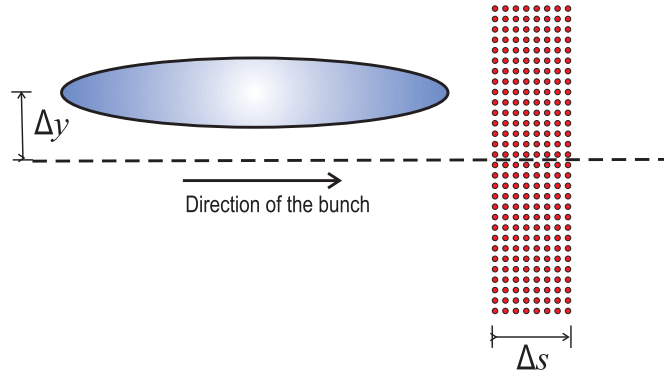


Figure 5.1: Bunch with offset  $\Delta y$  in the transversal plane.

In the presence of the e-cloud the motion of the beam particles will be perturbed especially if the center of mass of the beam and the e-cloud don't match in the transversal plane. Considering an initially homogeneous distribution of the e-cloud inside the beam pipe, a bunch with certain  $\Delta y$  offset from the symmetry axis would be perturbed by the e-cloud. The equation of vertical motion of the bunch particles perturbed by the force of the electron cloud  $F_{e,y}$  writes:

$$m \frac{d^2 y}{dt^2} = -q B_x v + F_{e,y}, \quad (5.4)$$

where  $v$  is the longitudinal velocity of the bunch  $v = \beta_{rel} c$  and  $B_x = gy$  is the horizontal component of the quadrupole field with gradient  $g$ . Writing the previous equation as function of the position  $s$  instead of the time  $t$  yields:

$$mv^2 y''(s) = -qgv y + F_{e,y}. \quad (5.5)$$

Dividing by  $mv^2$  and introducing the focusing coefficient  $k(s) = (qg)/p$  leads to the equation of vertical motion of a particle perturbed by the e-cloud:

$$y''(s) + \frac{qg}{p} y = y''(s) + k(s)y = \frac{F_{e,y}}{mv^2}. \quad (5.6)$$

Without the e-cloud force  $F_{e,y}$  the equation (5.6) is valid for unperturbed motion which for constant focusing  $k(s) = k$  gives the relation between the focusing coefficient  $k$  and the unperturbed tune  $Q_{y0}$ :

$$k = \left( \frac{Q_{y0}}{R} \right)^2. \quad (5.7)$$

By linearizing the perturbation force  $F_{e,y}$  acting on the particles of the bunch with  $\Delta y$  offset in the vertical centroid position, equation (5.6) could be written as:

$$y''(s) + ky = \frac{F_{e,y}}{mv^2} \frac{y}{\Delta y}. \quad (5.8)$$

Equation (5.8) is still describing an oscillatory motion of a simple harmonic oscillator

$$y''(s) + \left( k - \frac{F_{e,y}}{mv^2 \Delta y} \right) y = 0, \quad (5.9)$$

although now with different betatron tune  $Q_y$  given by

$$\left( \frac{Q_y}{R} \right)^2 = k - \frac{F_{e,y}}{mv^2 \Delta y} = \left( \frac{Q_{y0}}{R} \right)^2 - \frac{F_{e,y}}{mv^2 \Delta y}. \quad (5.10)$$

Since the tune shift is very small compared with the unperturbed tune  $\Delta Q_y \ll Q_{y0}$  it applies  $Q_y \approx Q_{y0}$  and so the tune shift  $\Delta Q_y = Q_y - Q_{y0}$  due to the interaction with the e-cloud could be computed as:

$$\Delta Q_y \approx -\frac{R^2}{2Q_{y0}} \frac{F_{e,y}}{mv^2 \Delta y} = -\frac{R\bar{\beta}_y}{2} \frac{F_{e,y}}{p\beta_{rel}c\Delta y}. \quad (5.11)$$

For practical computation of  $\Delta Q_y$  from (5.11),  $\bar{\beta}_y$  is the average beta function and  $p$  the momentum of the beam.

### 5.1.2 Numerical Computation of the Tune Shift

In order to compute the tune shift caused by the e-cloud (5.11) it is necessary to evaluate the vertical force acting on the bunch particles:

$$F_{e,y} = \frac{dp_y}{dt} \approx \frac{\Delta p_y}{\Delta t}. \quad (5.12)$$

Hence the change of the vertical impulse  $\Delta p_y$  of the bunch particles has to be computed after interaction with the e-cloud during the time interval  $\Delta t$ . The time span  $\Delta t$  corresponds to a longitudinal section  $\Delta s$  of the ring where the interaction takes place:

$$\Delta t = \frac{\Delta s}{v} = \frac{\Delta s}{\beta_{rel}c}.$$

Finally the vertical tune shift can be evaluated from:

$$\Delta Q_y \approx -\frac{R\beta_{y0}}{2} \frac{\Delta p_y}{p} \frac{1}{\Delta s \Delta y}. \quad (5.13)$$

Consequently it is sufficient to perform a numerical simulation with MOEVE PIC Tracking where a given bunch with momentum  $p$  and certain vertical offset  $\Delta y$  progresses through an e-cloud with length  $\Delta s$  (as principally shown in Figure 5.1). After passing through the interaction section  $\Delta s$ , the resulting  $\Delta p_y$  of the bunch particles gives the contribution to the  $\Delta Q_y$  of the e-cloud concentrated in the section  $\Delta s$ . Approximating a constant e-cloud density of  $\rho_e$  throughout the storage ring allows the results for the tune shift to be extrapolated for a single turn of the bunch.

### 5.1.2.1 Computational Studies

Interaction simulations were performed for a positron bunch of KEKB-LER defined in Table A.2 ( $\sigma_x = 0.42$  mm,  $\sigma_y = 0.06$  mm,  $\sigma_z = 6.00$  mm,  $N_e^+ = 3.3 \cdot 10^{10}$ ,  $E_{kin} = 3.5$  GeV) and an e-cloud with homogeneous density  $\rho_e = 10^{12}$  m $^{-3}$ . The interaction was simulated with e-clouds with different transversal sizes as shown in Figure 5.2. The bunch was represented by 1 million macro-particles whereas the e-cloud was represented by 0.5 million macro-particles and its elongation was taken to be  $\Delta s = 1$  cm. The bunch

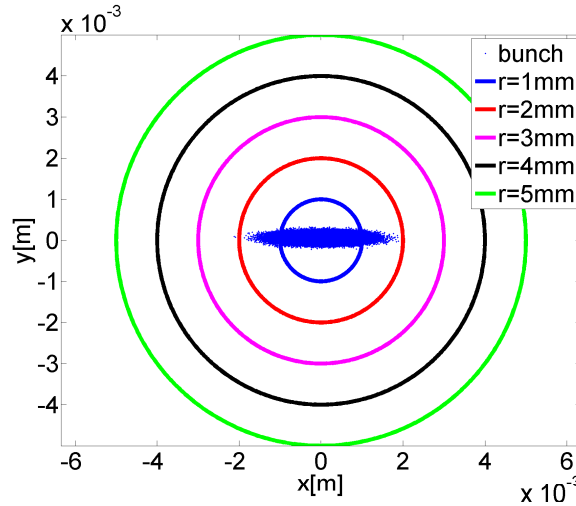


Figure 5.2: Different transverse e-cloud size and the offset beam.

was set to enter the e-cloud with an offset  $\Delta y = \sigma_y = 0.06$  mm. The traversing of the whole bunch length (from  $3\sigma_z$  to  $-3\sigma_z$ ) through the e-cloud was simulated which corresponds to a time of  $t = 200$  ps with discretization steps

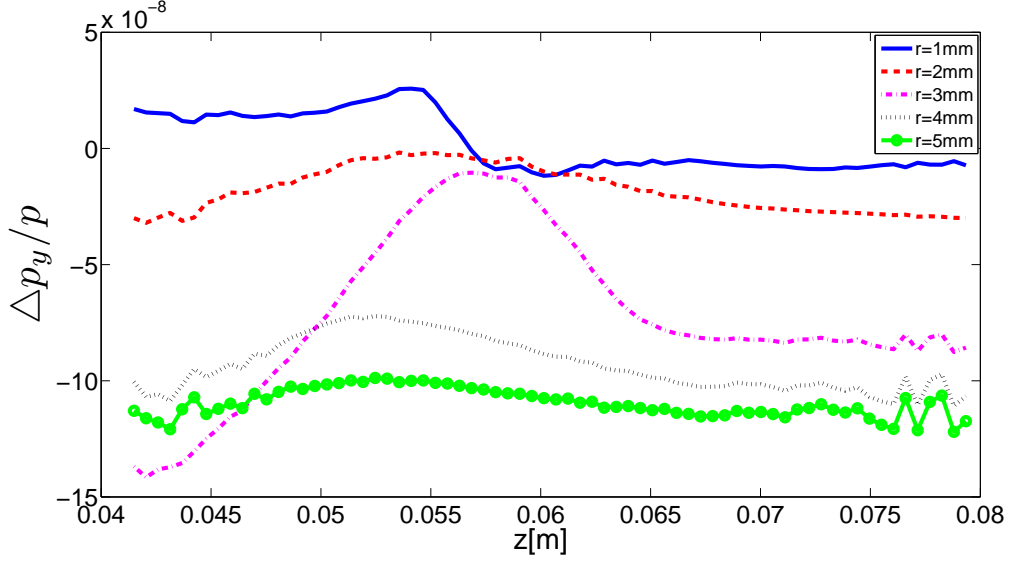


Figure 5.3: Vertical kick on the bunch particles along its length (the head of the bunch is at larger  $z$  values).

of  $dt = 1$  ps. For the beam pipe a circular cross-section with PEC boundary was assumed.

Figure 5.3 shows the average of the relative change of the vertical impulse  $\frac{\Delta p_y}{p}$  along the bunch length after the interaction with different transverse sizes of the e-cloud. The uninterrupted line in Figure 5.3 corresponds to the smallest e-cloud with  $r = 1$  mm from Figure 5.2 which in horizontal direction is even smaller than the bunch itself. The same  $\frac{\Delta p_y}{p}$  line in Figure 5.3 indicates that while the bunch particles in the head of the bunch receive a negative vertical kick, the center of mass of the electrons is shifted in the positive  $y$ -direction above the bunch axis. Hence the second part of the positron bunch receives a kick from the electrons in the positive  $y$ -direction. The kick from the second e-cloud ( $r = 2$  mm) starts lower simply because the forces of the more distant electrons sum up and give a stronger base force that pulls the offset bunch down. After half of the bunch passed through the cloud, the center of mass of the e-cloud moved up almost matching with the one of the bunch so that the overall vertical kick becomes weak (the maximum of the curve). However, this is only temporarily as the electrons repel each other and at the same time the number of electrons still approaching the bunch from below is higher than the ones from above the bunch so that again the tail of the bunch receives a negative vertical kick.

The same explanation could be applied to the kick curve from the cloud with  $r = 3$  mm with the notice that, because of the bigger number of elec-

trons, the forces from the distant electrons are stronger and those forces are reinforced with the slowly approaching electrons from higher radii. Again the electrons start repelling as their concentration on the beam axis starts to grow.

For the e-clouds with  $r = 4$  and 5 mm the kick on the bunch particles is nearly constant over the whole bunch length and a saturation of the kick amplitude can be observed. The last conclusions coincide with those from [Ohmi 2001b] except that the computed kicks with the PIC simulation are one order of magnitude lower than the ones in [Ohmi 2001b]. Presumably this is due to the fact that in the PIC simulation the own space charge forces of the electrons are taken into account so that the electrons are not just attracted on the beam axis but as their concentration grows they will also repel and lower the number of electrons on the beam axis.

The simulations show a characteristic increase of the vertical tune due to the interaction with e-clouds observed in the measurements at several storage rings with a positively charged beam [Crittenden 2010].

## 5.2 Incoherent Effects of Electron Clouds

As previously mentioned, a fast instability of the positively charged beam occurs for e-cloud densities above a certain threshold  $\rho_{th}$ . The expression for  $\rho_{th}$  introduced in [Ohmi 2005a] is derived by estimating the short range wake force due to the interaction of a coasting beam with a uniform electron distribution. However, even for e-cloud densities lower than the computed  $\rho_{th}$  the beam quality could deteriorate and become useless for the users. The reason for that is an incoherent head–tail effect on the bunch due to the interaction with the e-cloud. The head–tail effect is especially pronounced if the synchrotron damping period is relatively long [Benedetto 2007]. Hence this incoherent effects could lead to a significant long-term emittance growth. The following work follows an approach to study the long term beam stability by tracking the beam through the linear optics of the storage ring and at each turn to apply the transversal kick due to the interaction with the e-cloud. The results presented in the following are published as contributions on several international conferences on Particle Accelerator Physics ([Marković 2010], [Marković 2011] and [Marković 2012a]) and Computational Accelerator Physics ([Marković 2009] and [Marković 2012b]).

### 5.2.1 Head - Tail Simulation with Vertically Displaced Parts of the Bunch

Because of the nature of the beam - e-cloud interaction there will be a dipole kick on the bunch only if a part of the bunch perturbs the cloud, typically if a part of the bunch has a slight transversal offset at the entrance into the cloud of homogeneously distributed electrons (Figure 5.4). As shown in the

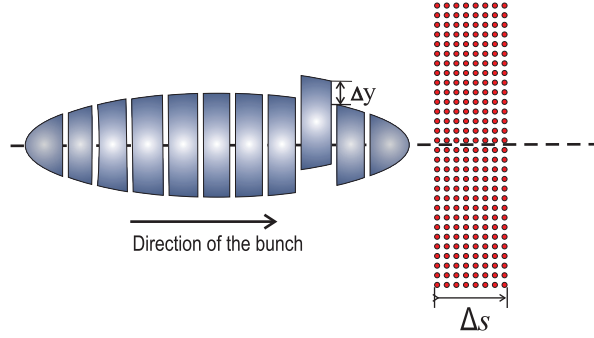


Figure 5.4: Profile of the bunch with an  $\Delta y$  offset slab in the leading part of the bunch.

previous chapter, the e-cloud is not going to be asymmetrically perturbed if the bunch traverses through without any transversely displaced parts. During its passage, it only destroys the homogeneous distribution of the electrons because it attracts them towards the beam axis. As a result, the concentration of electrons near the beam axis grows very fast during the bunch passage. As a matter of fact, the electrons near the beam axis start oscillating in the beam potential while the electrons from higher radii are approaching the beam axis and increase the number of electrons near the beam axis. Thus, if a transversal offset in the bunch occurs in the middle or the rear parts of the bunch, the number of electrons on the beam axis which will be perturbed by the displaced part is very high. Consequently the kick from the cloud on the following bunch slices would be expected to be stronger. On the contrary, if the transversal offset occurs in the head part of the bunch then the number of electrons that will be perturbed is not going to be that large and so the expected transverse kick on the following bunch slices would not be as strong as if the electron perturbation happens later during the bunch passage. To underline this simple consideration a series of interaction simulations are done with a bunch which for each simulation has a different 3D slab shifted in the transversal plane as principally shown in Figure 5.4. For the examples presented here the offset in the  $y$ -plane is equal to  $\Delta y = \sigma_y$  of the bunch. The bunch parameters are given in Table A.1. Figures 5.5–5.9 display the vertical velocity  $v_y$  of the bunch particles after the passage through an initially

homogeneous e-cloud, corresponding to different offset slabs starting from the head of the bunch backwards. The red line is the average value of the vertical velocity of the particles over the bunch length. Figures 5.5 and 5.6 result

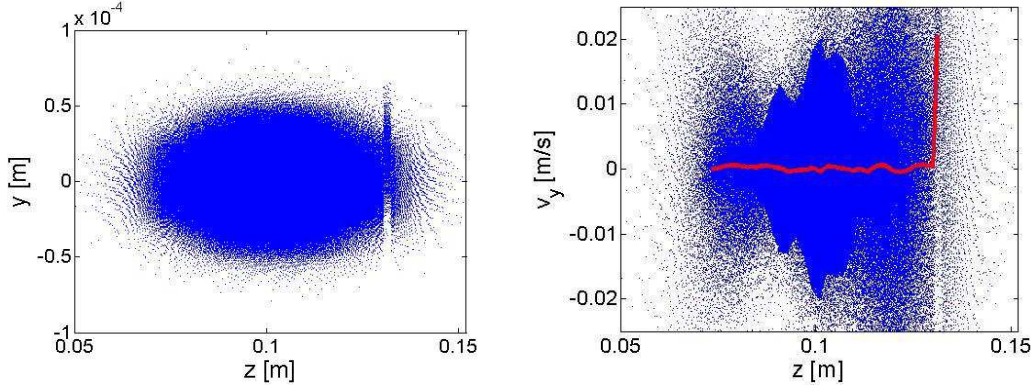


Figure 5.5: Transversal velocity ( $v_y$ ) of the bunch particles after the passage through the e-cloud (right). The offset slab is at the beginning of the bunch as shown in the profile plot (left).

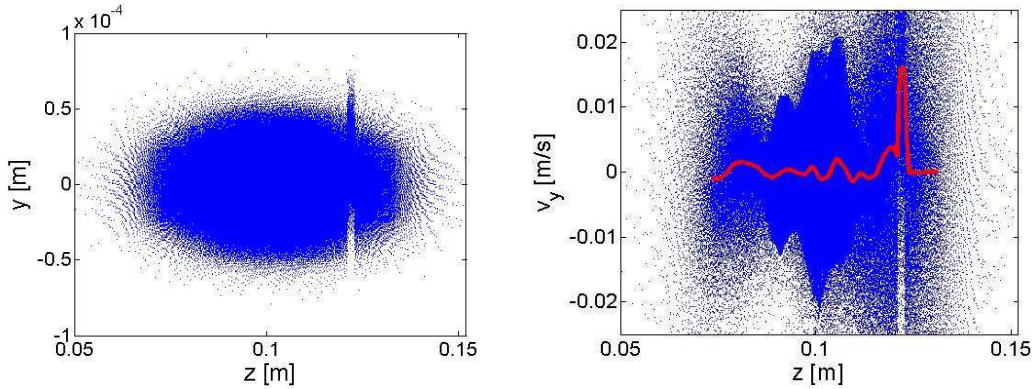


Figure 5.6: transversal velocity ( $v_y$ ) of the bunch particles after the passage through the e-cloud (right). The offset slab is at the beginning of the bunch as shown in the profile plot (left).

from the displaced head parts of the bunch (as shown on the left plot of the corresponding figure). It can be observed that the particles of the offset part got a vertical kick towards a higher radius of the pipe. This is due to the fact that the electrons from the higher radii started moving towards the beam axis being attracted by the previous head parts of the bunch. Thus, the offset part has been attracted towards those electrons approaching from the higher radii. In Figure 5.5 the number of electrons on the beam axis is relatively small at the



moment when the displaced part of the bunch arrives so that the perturbation by the displaced part of the bunch does not considerably affect the following parts. However if the displaced part is 10 ps later as shown in Figure 5.6 (left) then the number of electrons on the beam axis which are perturbed by the displaced part is higher. Thus the perturbed electrons exhibit a stronger dipole kick on the rest of the bunch as shown in Figure 5.6 (right). The

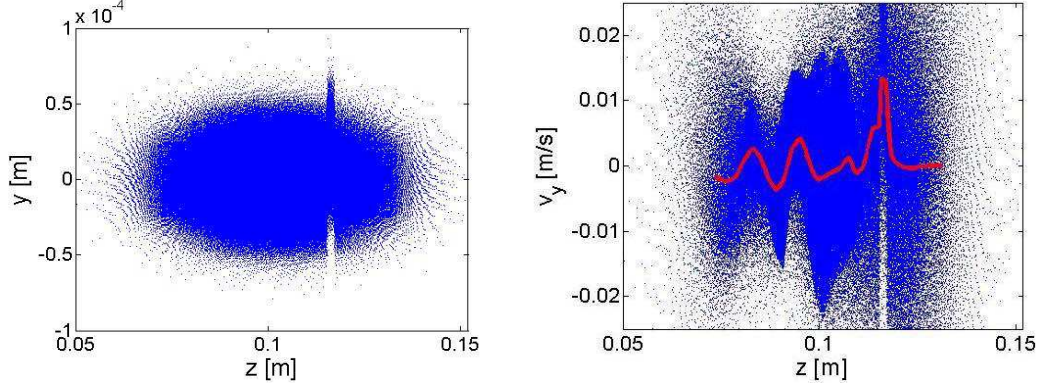


Figure 5.7: Transversal velocity ( $v_y$ ) of the bunch particles after the passage through the e-cloud (right). The offset slab is shown in the profile plot (left).

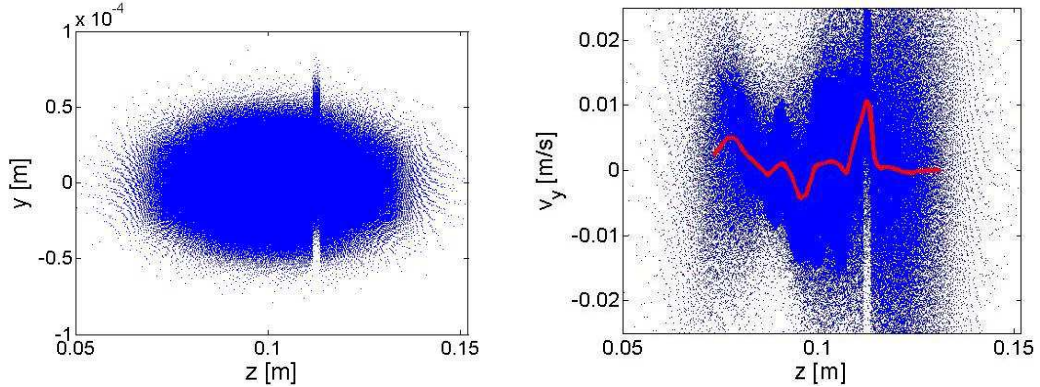


Figure 5.8: Transversal velocity ( $v_y$ ) of the bunch particles after the passage through the e-cloud (right). The offset slab is before the middle of the bunch (left).

results of simulations at which the displaced part of the bunch is still in the front part of the bunch but more towards the center of the bunch are plotted in Figure 5.7 and 5.8. The average vertical kick from the e-cloud is stronger than one in 5.6 and oscillates along the bunch length due to the oscillation of the centroid position of the perturbed electrons. Thereby, the perturbation



of the electrons is strong not only because the number of electrons near the beam axis is higher but also because the number of particles in the displaced part of the bunch is higher due to the Gaussian longitudinal charge profile.

On the other hand, Figure 5.9 (right) displays the vertical velocity of the bunch for the case that its offset part is in its middle as shown in Figure 5.9 (left). Here, due to the focusing from the previous parts of the bunch the electron concentration on the beam axis will be very high by the time at which the offset part arrives in the e-cloud. Hence, the electrons on the beam axis pull the offset part down towards the beam axis. The offset particles receive an impulse in the negative direction as it can be seen from the trend of the red line at the longitudinal position of the offset part. At the same time the electrons on the beam axis will be perturbed and shifted towards the centroid position of the offset part of the bunch. Thus, the following bunch parts will receive a transversal kick in the positive direction (towards the centroid position of the previous offset part).

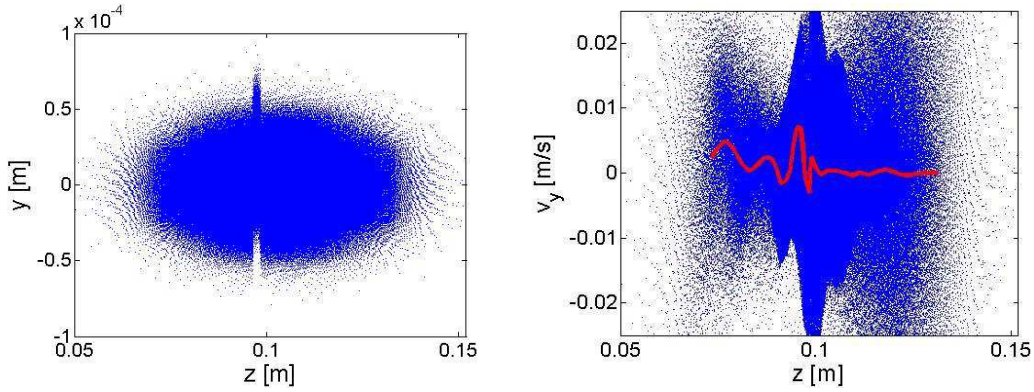


Figure 5.9: Transversal velocity ( $v_y$ ) of the bunch particles after the passage through the e-cloud (right). The offset slab is after the middle of the bunch (right).

This sort of a head-tail coupling between the bunch part perturbing the cloud and the following bunch parts happens on a very short time scale, due to a very rapid movement of the electrons in the transversal plane around the beam axis. The transversal movement of the beam particles is comparatively slow.

### 5.2.2 Wake Field induced by Electron Cloud

The excitation of the electron cloud by a single bunch progressing through it and the reaction of the cloud on the same bunch resemble a short-range wake field. The wake field drives a single-bunch instability of head-tail type

which is manifested by a strong transverse emittance growth. The head-tail instability is damped by the synchrotron motion of the particles where they change their relative longitudinal position in the bunch. Hence, in order to evaluate the stability of a bunch interacting with electron clouds, the bunch movement should be followed until the synchrotron period of the beam has been resolved. As earlier mentioned, the synchrotron period compared to the period of the betatron motion is much longer and may correspond to several thousands of turns of the bunch in the storage ring. At each turn through the storage ring the bunch interacts with the e-cloud. The interaction is more pronounced in sections of the storage ring where a considerable amount of electrons may accumulate. As previously shown for the dipole magnet, the electrons are trapped in the magnetic field. Similarly the electrons are trapped along the field lines of quadruple or sextuple magnets. In addition, in the dipole magnets the synchrotron radiation of the beam produces new primary electrons.

The approach to simulate the single bunch instability consists of tracking the bunch particles by multiplying the phase space vector of each particle  $\psi(x, p_x, y, p_y, z, p_z)$  with the transformation matrices describing the storage ring lattice. Thereby the action of the e-cloud on the bunch is applied at each turn on one or more interaction points in the lattice. A fully self-consistent PIC beam – electron cloud interaction simulation at every turn, even with only one interaction point per turn, would inevitably lead to high computational costs. An idea to speed up the single bunch instability simulation would be to pre-compute the transverse kick of the e-cloud on the bunch. Such a pre-computed wake field will be later applied on the bunch at each turn during the tracking of the bunch with the appropriate transport matrices.

In [Ohmi 2001c] the wake field is approximated by a resonator, whose parameters ( $R_s/Q$ ,  $\omega_R$ , and  $Q$ ) are determined by using both analytical and simulation approaches. The analytic approach gives the resonator parameters for a rigid Gaussian beam in the transverse plane and an electron cloud of equal rms size. In this early analytical approach  $Q$  was infinite, because the wake field had a unique frequency and did not decay. The frequency of the wake field corresponds to the frequency of electrons in the beam potential  $\omega_e$  as given in 4.1.

Since the oscillation of the electrons is damped due to the nonlinear force of the beam, in [Ohmi 2005b] the vertical wake field  $W_y(z)$  is expressed as damped oscillator:

$$W_y(z) = c \frac{R_s}{Q} e^{-\omega_e z / 2cQ} \sin\left(\frac{\omega_e}{c} z\right) \quad (5.14)$$

where  $W_y \neq 0$  for  $z < 0$ .

The resonator parameter  $c \frac{R_s}{Q}$  is computed from:

$$c \frac{R_s}{Q} = K \frac{\lambda_e}{\lambda_b} \frac{L}{\sigma_y(\sigma_x + \sigma_y)} \frac{\omega_e}{c}, \quad (5.15)$$

where  $N_b$  is the number of particles in the bunch.  $\lambda_e$  is the local density of the electron cloud near the beam axis and can be computed from the electron volume density  $\rho_e$  and the transverse size of the e-cloud as  $\lambda_e = 4\pi\rho_e\sigma_{x,e}\sigma_{y,e}$ . The enhancement factor  $K$  is due to the number of electrons contributing to the instability and  $L$  is the circumference of the storage ring.

The simulation approach to compute the wake field from [Ohmi 2001c] includes the nonlinearity of the beam–cloud interaction as well as the effect of the cloud size. On the other hand, the wake field computation did not take into account the nonuniform longitudinal charge distribution inside a bunch, and the own space charge forces of the electrons. Nevertheless, by computing the amplitude and the rough frequency range of the wake field from these conventional wake field models it is possible to estimate the threshold of the e-cloud density.

The estimation of the bunch stability requires the change of the vertical momentum of a particle  $\Delta p_y$  at a longitudinal position  $z$  in the bunch due to the e-cloud perturbations induced by the preceding part of the bunch at  $z'$ . With the pre-computed wake field ( $W(z - z') \neq 0$  for  $z < z'$ ) the change of the vertical momentum of a particle with overall momentum  $p_b$  can be computed as:

$$\frac{\Delta p_y}{p_b} = \frac{N_b r_e}{\gamma} \int W_y(z - z') \lambda_y(z') dz', \quad (5.16)$$

where  $N_b$  is the number of particles in the bunch. Furthermore,  $\lambda_y(z')$  denotes the dipole moment at  $z'$  in the bunch, which is expressed by

$$\lambda_y(z') = \int y \psi(x, p_x, y, p_y, z, p_z) dx dp_x dy dp_y dp_z \quad (5.17)$$

with the distribution function of the beam in the phase space ( $\psi$ ) normalized by 1:

$$\int \psi dx dp_x dy dp_y dz dp_z = 1. \quad (5.18)$$

Yet the bunch tracking with such a computed wake field could not predict aspects of the instability such as the synchro-betatron sideband  $Q_y + kQ_s$  ( $1 < k < 2$ ) of the vertical tune observed in experiments at several machines.

The reason is that the wake field from the perturbed cloud cannot be treated as the wake field from a broadband resonator which is computed for constant geometries and material parameters of the beam pipe. The e-cloud as a beam environment evolves during the bunch-passage and the computation

of the vertical force on the bunch particles has to take into account the e-cloud density near the beam axis when the perturbation happens.

Hence, the wake field due to the beam – e-cloud interaction cannot be treated as a function of the distance between the excitation (at  $z'$ ) and the part of the bunch receiving the kick (at  $z$ )  $W(z - z')$ . Instead, the wake field modelling the beam – e-cloud interaction should be a two-variable function of both positions  $W(z, z')$ .

### 5.3 Two-Variable Wake Field induced by an Electron Cloud

From the previous considerations it is obvious that the numerically pre-computed transverse wake due to the interaction with the e-cloud has to be a wake matrix which can be extracted from detailed beam - e-cloud interaction simulations with MOEVE PIC Tracking. Thereby, following the idea of K. Ohmi [Ohmi 2008], the 3D bunch is longitudinally divided into  $M$  slices. A slice which has a transverse displacement respective to the other slices, e. g. the slice  $i$  in Figure 5.10, induces a transverse kick from the e-cloud on the following slices. Hence it is necessary to perform  $M$  MOEVE PIC Tracking

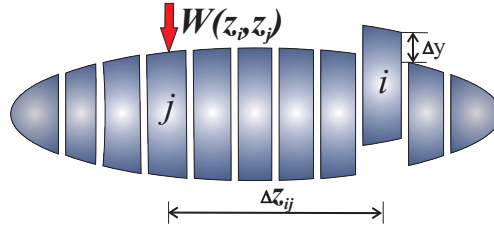


Figure 5.10: Slicing the 3D bunch into  $M$  longitudinal slices and introducing an offset  $\Delta y$  in the transversal plane for each slice at the time.

simulations of the interaction in which each of the slices  $i = 1, \dots, M$  has an offset ( $\Delta x / \Delta y$ ) at the time which is responsible for inducing a dipole kick  $\Delta p_{x/y}$  on the following  $j = i, \dots, M$  slices ( $z_i > z_j$ ). The resulting  $M \times M$  matrix of average transverse kicks is a triangular matrix with non-zero entries  $\Delta p_{x/y}(i, j)$  for  $i = 1 \dots M$  and  $j = i \dots M$ . The e-cloud is modelled as a uniform distribution of electrons in a beam pipe and is assumed to be generated by the preceding bunches. For flat beams as the KEKB-LER beam (Table A.2), the flat i. e. the vertical plane is critical for the stability. Thus the simulations feature a vertical slice displacement (as shown in Figure 5.10), typically  $\Delta y = \sigma_y$ .

According to equation (2.71) the wake  $W_y$  from the slice  $i$  which contains  $N_i$  positrons displaced by  $\Delta y$  can be expressed as:

$$W_y = \frac{\Delta p_y}{e^2 N_i \Delta y}, \quad (5.19)$$

where  $e$  is the electric charge of an electron and  $\Delta p_y$  is the change of the vertical momentum of a trailing bunch particle. By multiplying both sides of (5.19) with the relativistic energy  $\gamma m_e c^2$  of the bunch particles and introducing the relativistic electron radius  $r_e$ , the wake induced from slice  $i$  on a particle in slice  $j$  reads as:

$$W_y(z_j, z_i) = \frac{\gamma \Delta p_y(j, i)}{p_b r_e \Delta y_i N_i} [1/\text{m}^2], \quad (5.20)$$

where  $p_b$  is the relativistic energy of the bunch and  $\gamma$  is the Lorentz factor. Such a computed wake field can be converted in [V/Cm] by multiplying it with  $1/4\pi\epsilon_0$ .

### 5.3.0.1 Two-Variable Wake Field induced by an Electron Cloud in KEKB-LER and ILC $e^+$ DR

The idea of K. Ohmi to slice the 3D bunch and compute a wake function from every longitudinal slice of the bunch (Figure 5.10) backwards leads to a triangular wake matrix. Thereby the wake matrix is computed for a constant displacement of each slice, typically  $\Delta y_i = \sigma_y$ . In order to compute the kick from a transversally sliced slab  $i$  on the trailing bunch slabs  $j$  ( $z_i > z_j$ ), both positron bunches ILC-DR<sup>1</sup> (Table A.3) and KEKB-LER (Table A.2) were longitudinally divided into  $M = 30$  slabs. Thus, a series of  $M$  interaction simulations were performed. For each simulation a single slab  $i$  ( $i = 1 \dots M$ ) of the bunch was shifted by  $\Delta y_i = \sigma_y$  and the whole bunch was sent through an initially homogeneous e-cloud with  $10^{12}$  electrons/m<sup>3</sup>. The interaction was simulated until the whole bunch traversed the length of the e-cloud of 1 cm. The time step of the interaction simulation  $dt=1$  ps. The non-equidistant grid for the interaction simulations was adapted individually for each of the positron bunches due to the different bunch sizes and aspect ratios in the transverse dimensions.

The computed kick  $\Delta p_y(j, i)$  was extrapolated for the length of the interaction region which in the case of only one interaction point per turn would be the circumference  $L$  of the corresponding ring.

Each bunch slice has equal longitudinal width ( $dz$ ) and contains  $N_i = N_p \lambda(z_i) dz$  number of positrons, where  $\lambda(z) = N_p / \sqrt{2\pi} \sigma_z \exp(-z^2/2\sigma_z^2)$ .

---

<sup>1</sup>corresponding to one of the designs for the positron damping ring (DR) of the International Linear Collider (ILC)

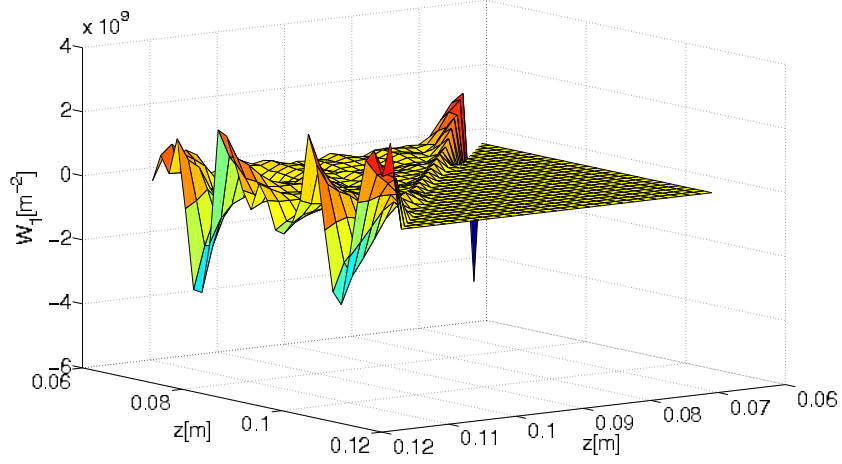


Figure 5.11: Two-variable wake field  $W_1(z_j, z_i)$  for the ILC damping ring,  $M = 30$  slabs. Both  $z$  axes represent the length of the bunch, the higher value corresponds with the beginning of the bunch and the lower the end of the bunch in longitudinal direction.

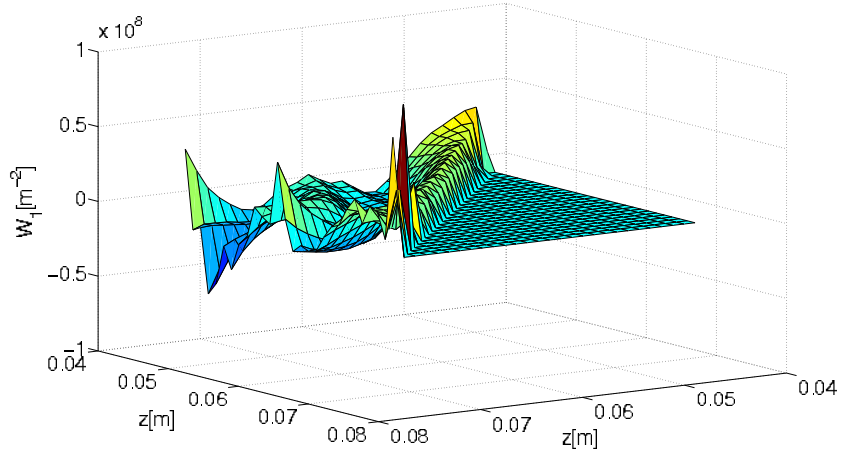


Figure 5.12: Two-variable wake field  $W_1(z_j, z_i)$  for the KEKB-LER,  $M = 30$  slabs. Both  $z$  axes represent the length of the bunch, the higher value corresponds with the beginning of the bunch and the lower the end of the bunch in longitudinal direction.

Thereby the number of positrons in each slice  $N_i$  ( $i = 1 \dots M$ ) varies considerably due to the Gaussian profile of the particle distribution in longitudinal direction  $\lambda(z)$ . Finally the wake matrix was computed for both rings as shown in Figure 5.11 and 5.12.

## 5.4 Tracking with a Pre-Computed Wake Matrix

Subsequently the wake matrix is used to track the sliced bunch through the linear optics of the storage ring while at each turn applying the corresponding transversal kick from the pre-computed wake. The applied transversal kick on a particle in a slice  $j$  is scaled with the actual offset value  $\Delta y_i$  of the preceding slice  $i$  ( $j > i$ ). During the tracking, the total vertical kick on a particle in the slice  $j$  represents a superposition of the corresponding kicks from all the preceding slices  $i = 1 \dots j$ . Hence, in order to apply the computed wake matrix for the bunch tracking it is necessary to assume properties of the wake field such as linearity, superposition and time invariance.

### 5.4.1 Properties of the Two-Variable Wake Field

The linearity of the wake kick is proven with a study of the scalability of the wake kick depending on the displacement  $\Delta y_i$  of the perturbing slice  $i$ . Additionally the wake field values and their scalability are examined for different realistic electron densities. The series of simulations is performed for

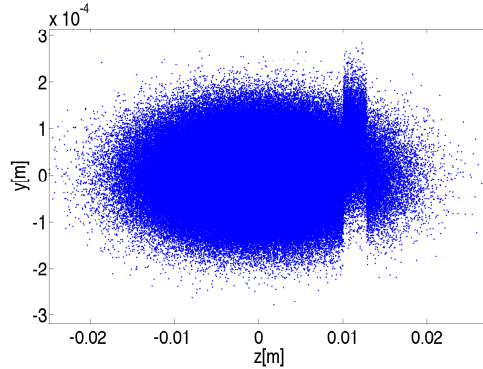


Figure 5.13: The bunch is represented by  $10^6$  macro-particles. In longitudinal direction the bunch is sliced into  $M = 20$  slices. The fifth slice from the head of the bunch is displaced by  $\Delta y_5 = \sigma_y$ .

the KEKB bunch as illustrated in Figure 5.13. The beam pipe has a small radius of 5 mm and a uniform electron distribution fills a length of 10 mm. The positron bunch is represented by  $10^6$  macro-particles whereas the cloud, at least for lower densities, is represented by unit charges. In each direction the bunch particles have a Gaussian distribution. Longitudinally the bunch spreads from  $-4\sigma_z$  to  $+4\sigma_z$  and is virtually sliced in  $M = 20$  slices. The time step used for the interaction simulation is 1 ps.



#### 5.4.1.1 Wake Function vs. Displacement

The wake field is computed for various displacements  $\Delta y$  of the fifth slice ( $\Delta y = (0.1 : 0.1 : 1) \sigma_y$ ). In (5.20) the wake field is expressed as a linear coefficient of the dipole kick  $\Delta p_y(i, j)$  and the dipole perturbation  $\Delta y_i N_i$ . Figure 5.14 shows a linear growth of the dipole kick with the displacement. The wake field in Figure 5.15 shows opposite ordering of the lines due to the

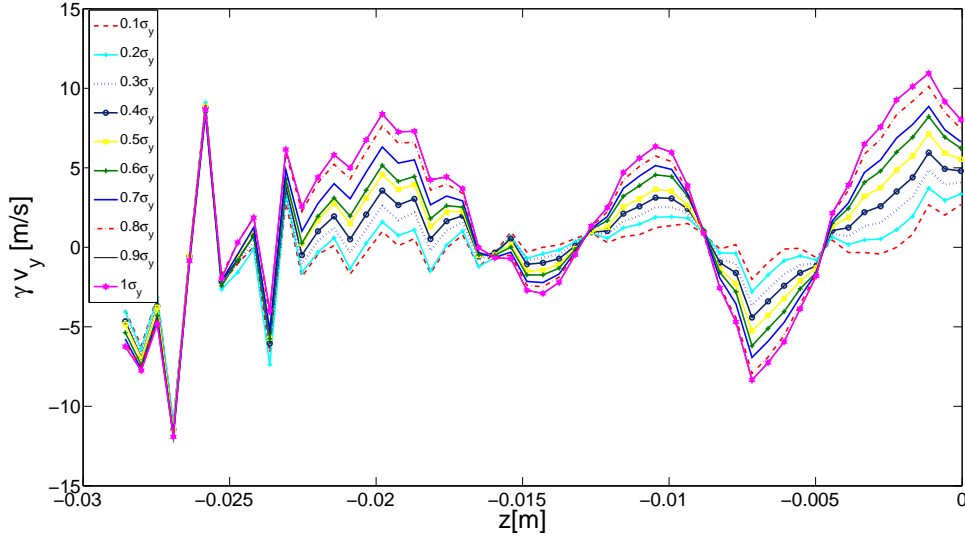


Figure 5.14: Average vertical dipole kick  $\Delta p_y(5, j)$  on the bunch slices  $j = 6, \dots, M$ , simulated for displacements of the fifth slice from  $0.1\sigma_y$  to  $\sigma_y$ .

growing denominator in expression (5.20) with the displacement.

The conclusion is that the transverse kick from the e-cloud scales linearly with the offset  $\Delta y_i$  and saturates for displacement amplitudes  $\Delta y \approx \sigma_y$ . Also, the observations in [Ohmi 2001c] indicate the same characteristics of the wake kick. Therefore, the kicks induced by slices with smaller offset  $\Delta y_i < \sigma_y$  are linearly scaled according to their actual offset  $\Delta y_i$ .

#### 5.4.1.2 Wake Function vs. Electron Density

In the simulations, the density of the electron cloud was varied below and above the computed threshold value for incoherent single bunch instability (ca.  $10^{12}$  electrons/m<sup>3</sup> at KEKB-LER). Figure 5.17 shows that the amplitude of the wake forces grows with the growing density of the e-cloud. The blue line from Figure 5.17 for  $\rho_e = 10^{11}$  electrons/m<sup>3</sup> is plotted once again in Figure 5.16. Figure 5.16 also shows the presence of the characteristic dipole



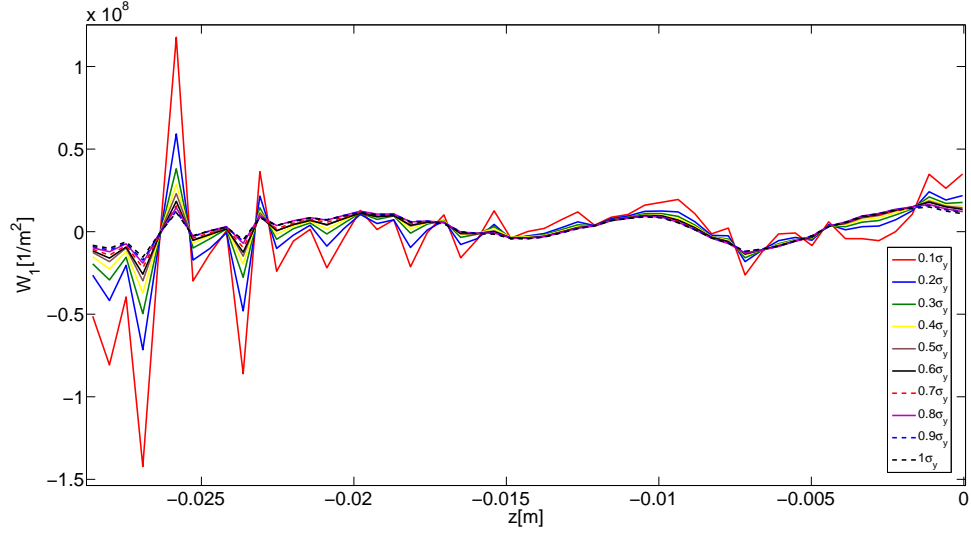


Figure 5.15: Average vertical wake field  $W_1(5, j)$  on the bunch particles of slices  $j = 6, \dots, M$ , computed for displacements of the fifth slice from  $0.1\sigma_y$  to  $\sigma_y$ .

wake kick (from the electrons perturbed by the fifth slice) for lower electron densities below the instability threshold. The oscillations of the wake kick are closely correlated to the oscillations of the electrons near the beam axis.

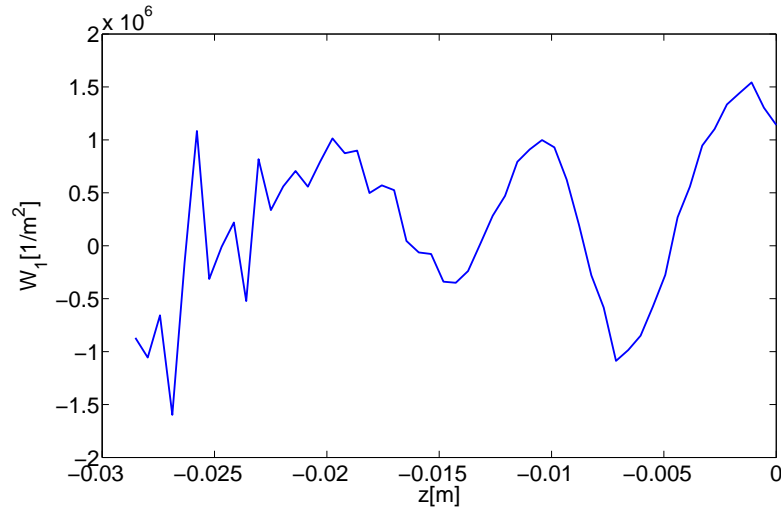


Figure 5.16: Average vertical wake field  $W_1(5, j)$  on the bunch particles of slices  $j = 6, \dots, M$ , computed for an e-cloud density of  $\rho_e = 10^{11}$  electrons/m<sup>3</sup>.

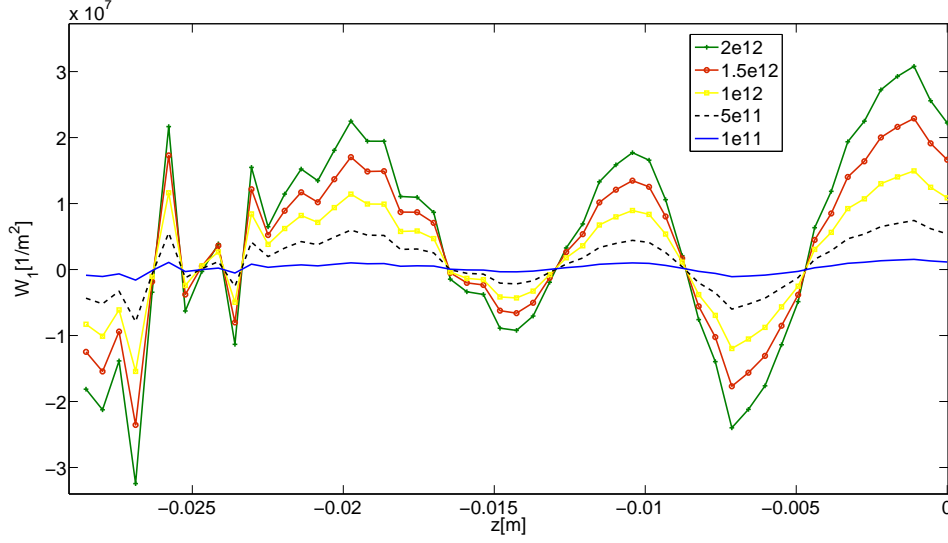


Figure 5.17: Average vertical wake field  $W_1(5, j)$  on the bunch particles of slices  $j = 6, \dots, M$ , computed for e-cloud densities  $\rho_e = 1.0 \cdot 10^{11}, 5.0 \cdot 10^{11}, 1.0 \cdot 10^{12}, 1.5 \cdot 10^{12}$  and  $2.0 \cdot 10^{12}$  electrons /m<sup>3</sup>.

#### 5.4.1.3 Superposition of the Wake Kicks

Another equally important aspect for realizing the single bunch stability tracking with the wake matrix is the applicability of the superposition principle for the kicks from the preceding slices of the bunch. Certainly a more realistic scenario of the interaction bunch – e-cloud is shown in Figure 5.18 where more than one slice has a certain vertical displacement. Thus, the question is whether the pre-computed wake, where only one slice at the time excites the perturbation of the cloud, could be applied and superposed with the other pre-computed kicks. Numerical experiments show that the overall density of the electrons in the proximity of the beam axes is not varying for small slice displacements  $|\Delta y| < \sigma_y$ . Hence the vertical displacements along the bunch length do not influence the number of electrons interacting with the slices of the bunch. However, the e-cloud centroid position changes due to the transverse displacements of the bunch slices. Note that during the PIC computation of the wake kick, the centroid position of the e-cloud is at the beam axis until the interaction with the displaced slice. The vertically displaced slice attracts the electrons towards its own centroid position. Thus, in order to superpose the kicks from consecutive displaced slices it should be ensured that the electrons near the beam have enough time to change their vertical centroid position towards the centroid position of the next displaced slice.

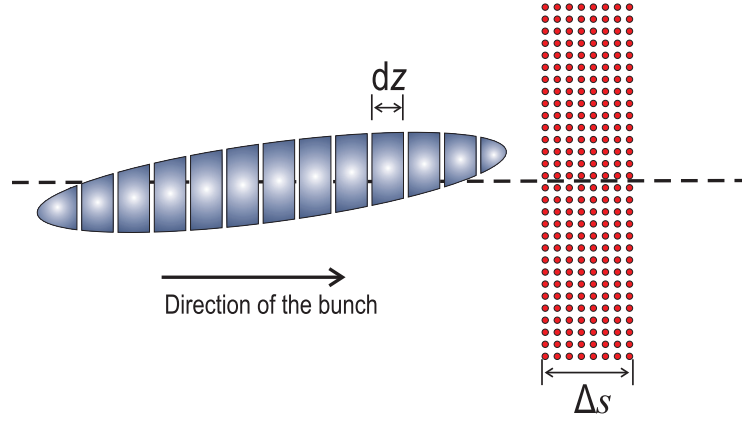


Figure 5.18: Realistic scenario of the interaction bunch – e-cloud where more than one slice has a certain vertical displacement.

To fulfill this condition for the superposition of the kicks, it is clear that the number of bunch slices  $M$ , i.e. their thickness in longitudinal direction, has to be controlled. A numerical study of the thickness  $dz$  of the slices in conjunction with the mobility of the electrons around the beam axis (the vertical velocity of the electrons near the beam axis) leads to a conclusion regarding the optimal slice thickness  $dz$ . Analyzing the vertical electron velocities oscillating in the potential of the bunch during the interaction it is possible to compute an average centroid velocity  $\bar{v}_{ye}$  of those electrons in the transversal range of  $\pm 2\sigma_y$  and  $\pm 2\sigma_x$ . Hence, the slice thickness  $dz$  in the lab frame corresponds to the time  $t_{ye}$  which the electrons need to change their vertical position for one  $\sigma_y$  in the proximity of the beam axis:

$$dz = t_{ye}c = \frac{\sigma_y}{\bar{v}_{ye}}c. \quad (5.21)$$

Since the Lorentz factor  $\gamma$  has typical values of several thousands for a storage ring beam, the bunch velocity is approximated by the speed of light  $c$ . The approximated time  $t_{ye}$  should equal the transition time of the e-cloud from one slice to the next so that the kick of each slice could be approximated by the pre-computed one. An integer division of the total bunch length  $8\sigma_z$  by  $dz$  yields the number of the slices:

$$M = 8\sigma_z/dz.$$

As an example, the average centroid velocity of the respective electrons interacting with the KEKB-LER bunch ( $\sigma_z = 6$  mm and  $\sigma_y = 0.06$  mm) is  $\bar{v}_{ye} = 7.5 \cdot 10^6$  m/s. The values plugged into (5.21) yield  $dz=2.4$  mm which corresponds to  $M = 20$  slices. If the number of longitudinal slices is much

higher than the superposition of the dipole kicks from the previous slices can not be expected.

## 5.5 Single Bunch Instability

Simulations of the bunch – e-cloud interaction demonstrated the head-tail effect on the bunch. The transverse kick of the e-cloud on the tail particles of the bunch lead to an incoherent transverse motion of the bunch and corresponding emittance growth. Fortunately, due to the synchrotron motion of the particles within the bunch, where the particles from the tail of the bunch move towards the head and vice-versa, the transversal kick is not always affecting the same particles. Thereby, the head-tail effect smears out which prolongs the emittance growth. Hence, in order to estimate the stability of a single bunch it usually needs to be tracked over the time of at least one synchrotron period. The synchrotron period lasts over many bunch turns (up to several thousands) in the storage ring. Thus, obviously the numerical simulation of the bunch stability interacting with the e-cloud is very challenging regarding computational recourses and time. It is clear that a PIC tracking of the bunch through the whole machine (while interacting with the e-cloud) for many turns is computationally impossible. Therefore, in the present simulations [Benedetto 2007] the bunch interacts with the cloud only at several interaction points (IP's) along the circumference of the ring and elsewhere it undergoes a transformation by the matrices describing the linear beam optics. The interaction on the IP's is usually simulated as PIC interaction in two or three dimensions computing the space charge forces with FFT routines [Vay 2009] or approximating the forces with the Basseti-Erskine formula in a transversal plane [Demma 2009]. However, even this approach with the IP's is relatively time and resource demanding which can be a limiting factor if many scenarios need to be simulated.

By following the approach of K. Ohmi, each turn to apply a wake kick on the bunch particles from the pre-computed wake matrix we hope to achieve a relatively fast estimation of the single bunch stability. Hence, at each turn with the tracking program PEWKT [Ohmi 2001a] of K. Ohmi the  $M$  slices of the bunch receive a kick according to the wake matrix by pre-computed MOEVE PIC Tracking. Thereby the kick at slice  $j$  is a superposition of the kicks induced by all the slices  $i = 1, \dots, j - 1$  ahead of slice  $j$  ( $z_i > z_j$ ).

The tracking program PEWKT, courtesy of K. Ohmi, uses a lowest order integrator, which is a combination of a thin lens kick and a drift in free space (or a lattice linear transformation), to integrate the motion of the particles.

In PEWKT the bunch is represented by a number of macro-particles dis-

tributed into  $M$  slices. Each slice includes about 10,000 macro-particles. After the application of the lumped kick of the electron cloud at the slices of the bunch, the bunch is transferred by the revolution matrix and the electron cloud is initialized again for the next interaction. The program considers the synchrotron oscillation i.e. the particles migrate in longitudinal direction among the slices.

The inputs of the program are the so-called twiss parameter, i.e. the mean beta function, and the tune in both transverse and in longitudinal direction. The input file contains the energy and the mass in electron volts, the number of particles in the bunch and the emittances in all three directions. Further inputs are the radiation damping in horizontal, vertical and longitudinal plane in milliseconds. Additionally the number of macro-particles which should be tracked with PEWKT and the number of turns through the machine have to be introduced. Finally the number of bunch slices  $M$  and the file containing the wake matrix are defined.

### 5.5.1 Tracking of a Positron Bunch in the KEKB-LER with a pre-computed Wake Matrix

The KEKB Low Energy Ring (LER) is a 3.5 GeV positron storage ring which is part of the electron-positron collider KEKB factory. Measurements reported in [Flanagan 2005] during operation with four trains, each of 100 bunches equally spaced at 8ns, showed a shift of the vertical betatron tune along the bunch train. Moreover, they registered the appearance of an upper sideband peak in the vertical tune spectra when the average bunch current was near the beam blow-up threshold. Also, the upper side band shifted along the train at the same amount as the betatron tune. This incoherent effect (observed until then in proton machines but since then also reported in several positron machines) is closely related to the incoherent head-tail effect of the e-cloud. After an initial part of the bunch train (around 40 bunches) the shift of the vertical tune and the side band stops and retains the values. This is probably due to the saturation of the e-cloud density. An indication of an e-cloud effect is the fact that when the solenoidal magnets which suppress the e-cloud density on the beam axis are switched on, the sidebands in the tune disappear, whereas when the solenoids are switched off, the sidebands appear again. Further indication of a head-tail effect is that the side band peak does not respond to dipole kicks from the bunch-by-bunch feedback system in the experiments [Flanagan 2005].

Hence, the measurements described in [Flanagan 2005] offer the possibility to verify the simulation technique for the single bunch stability. A computed wake matrix for a KEKB-LER bunch with the parameters given in Table A.2

and an e-cloud density of  $10^{12}$  electrons/m<sup>3</sup> is presented in Figure 5.12. For the simulation, the bunch was sliced into  $M = 30$  slices. Figure 5.19 shows a plot of the FFT power spectrum of the vertical tune of a KEKB-LER beam collected over 2048 turns. The results of the tracking with the wake matrix are

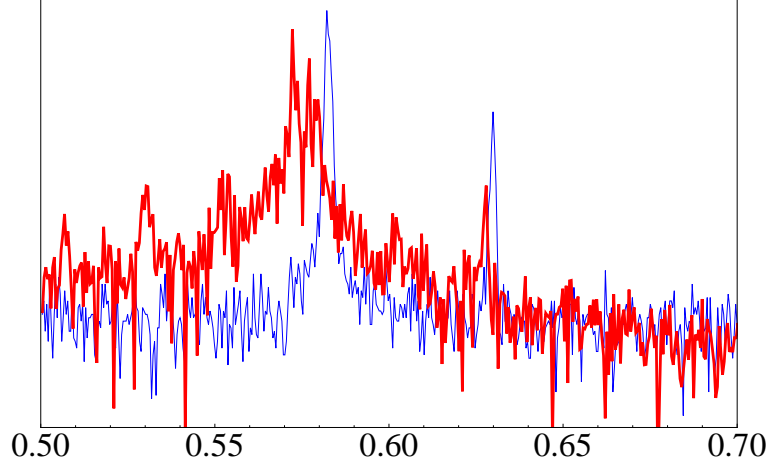


Figure 5.19: Fractional tune of the vertical betatron motion of a single bunch in a train of 100 bunches, measurement (blue) vs. simulation (red) with  $M = 30$  slices.

encouraging since they reproduce the upper side peak of the measurements. Since, the simulation (the red curve in Figure 5.19) also shows a sideband below the betatron tune which is not pronounced in the measurements.

## 5.6 Study for the PETRA III Storage Ring operated with Positron Beam

PETRA III at DESY, which started operation in 2009, is the most brilliant storage-ring-based X-ray radiation source in the world [DES 2013]. Until early 2013 the synchrotron radiation facility was running in a top up operation modus with positrons. The machine is characterized (Table A.1) by an ultra low emittance and with an emittance ratio of 2% it features very flat bunches. The design beam current of 100 mA was planned to be achieved with fillings of 40 or 960 equally spaced bunches [Wanzenberg 2003], [Balewski 2004]. However, for the filling scheme with 960 bunches with only 8 ns bunch-to-bunch distance a strong vertical emittance growth has been reported for currents of about 50 mA [Wanzenberg 2010]. The corresponding measurements of the tune spectra (Figure 5.20) show sidebands in the vertical tune which suggest incoherent effects. These effects are brought into connection with

electron cloud effects, on the bunch. After a systematic study of the effect,

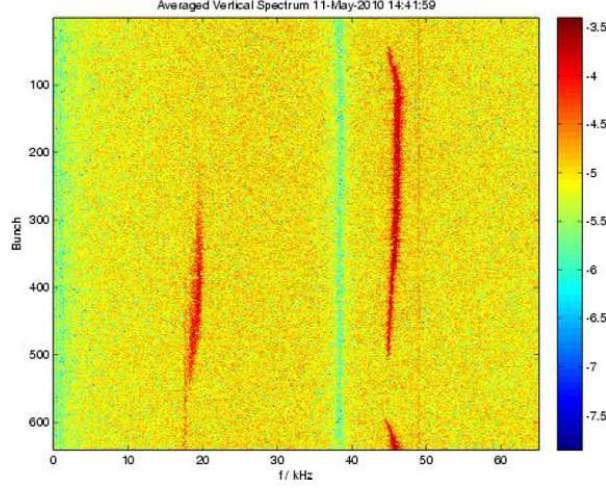


Figure 5.20: Vertical tune spectra of each of the 640 bunches with 8ns spacing, measured on May 11, 2010 [Wanzenberg 2010]. The total beam current was 62 mA. The red color represents the sidebands and the vertical betatron frequency of 38kHz is green. (Courtesy of R. Wanzenberg.)

the designed beam current of 100mA has been achieved by filling patterns with short bunch trains and longer gaps between them. The first two filling schemes presented in Figure 5.21 with 40 and 60 trains each of four bunches spaced at 16ns and 8ns respectively are used for user runs. The time spacing of 144ns and 80ns, respectively, between the trains is apparently enough to reduce the e-cloud density until the next train of four bunches arrives. On the other hand, the third filling pattern of 80 trains with only 48ns distance presented in Figure 5.21 features significant emittance growth. The e-cloud build up simulations with ECLOUD 4.0 (reported in [Wanzenberg 2010]) for a train with bunch-to-bunch spacing of 8ns and bunch population of  $0.5 \cdot 10^{10}$  positrons (secondary emission yield (SEY)  $\delta = 2.5$ ) show that after the first four bunches the e-cloud density is still below  $5 \cdot 10^{11} \text{ m}^{-3}$  which is below the instability threshold  $\rho_{th} = 1.4 \cdot 10^{12} \text{ m}^{-3}$  computed in [Wanzenberg 2012]. In 2011 and 2012 further 100 mA runs were performed with trains of 40, 60, 240 and 480 equidistantly spaced bunches with bunch-to-bunch distance of 192, 128, 32 and 16ns, respectively. Only during the run with 480 bunches a significant emittance growth has been measured [Wanzenberg 2012]. The filling pattern (Figure 5.22) was used for so-called "beam scrubbing runs"<sup>2</sup> on

<sup>2</sup>An adequate dose of photoelectrons, accelerated by positron bunches and hitting the the beam pipe wall will substantially reduce secondary emission and avoid the fast build-up of an electron cloud [Bruning 1999].



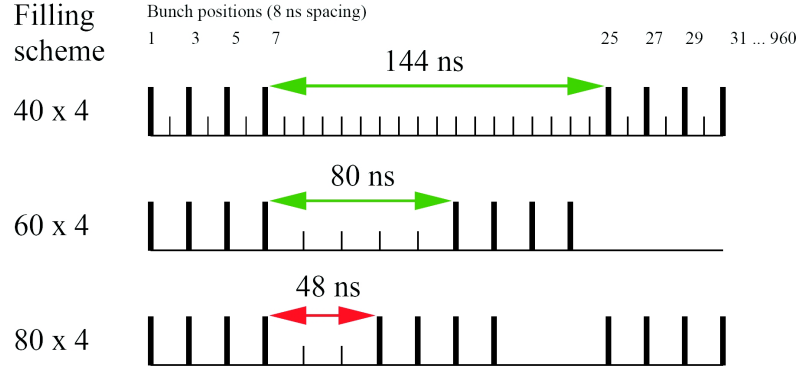


Figure 5.21: Bunch filling schemes with short bunch trains of 4 bunches. (Courtesy of R. Wanzenberg.)

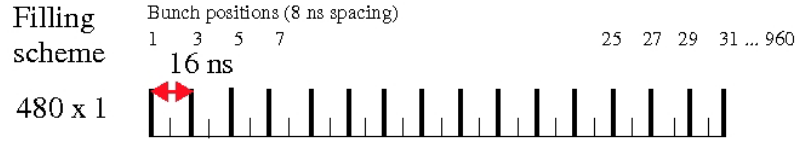


Figure 5.22: Top up operation with 480 bunches equidistantly spaced at 16ns. The filling pattern was used for beam scrubbing runs on two consecutive weekends in March 2012 (Courtesy of R. Wanzenberg.)

two consecutive weekends in March 2012 as a conditioning measure in order to lower the secondary emission yield of the beam pipe. The emittance measurements from the beam scrubbing runs are very valuable since they give the opportunity to validate the simulations.

Hence, the goal was to track a single bunch of the beam scrubbing run with a pre-computed wake matrix in order to see if the simulation could reproduce the measurements. The corresponding bunch parameters are given in the second part of Table A.1. The initial vertical emittance was taken to be  $\varepsilon_y = 20$  pm. The wake matrix was computed by vertically displacing each slice of the bunch by  $\Delta y = \sigma_y$ . The beam pipe has a small radius of 5 mm and a uniform electron distribution fills a length of 10 mm. The positron bunch is represented by  $10^6$  macro-particles whereas the e-cloud, at least for lower densities, is represented by unit charges. In each direction, the bunch particles have a Gaussian distribution. Longitudinally the bunch spreads from  $-3\sigma_z$  to  $+3\sigma_z$  and it is virtually sliced into  $M = 35$  slices. The thickness of the slices in the lab frame corresponds to the time which the electrons on the beam axis need to change their vertical position for one  $\sigma_y$ . The time



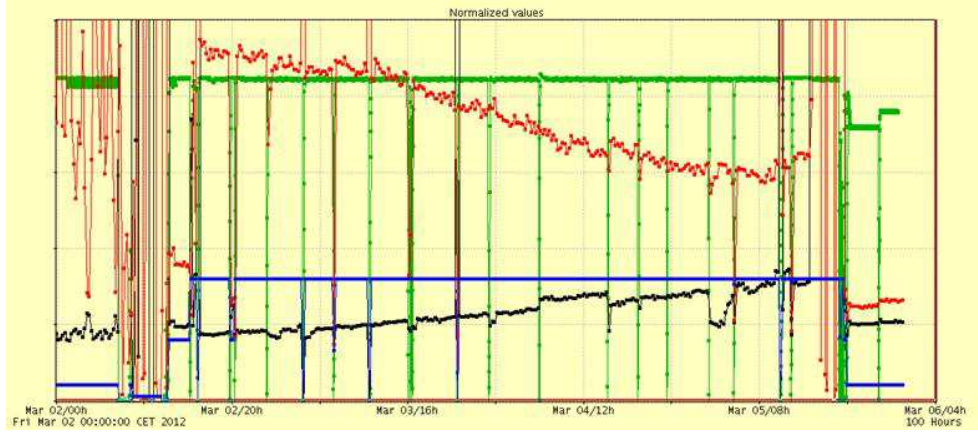


Figure 5.23: Run: 480 x 1 Beam Scrubbing, March 3 / 4, 2012. Vertical emittance 140 pm rad ( for 20 h), then dropping to 97 pmrad; Horizontal emittance Starting at 1.0 nm rad increasing to 1.8 nm rad; Green: total current (100 mA); Red: vertical emittance (scale 0-150 pm rad); Blue: Number of bunches (480); Black: horizontal emittance (scale 0-6 nm rad); (Courtesy of R. Wanzenberg.)

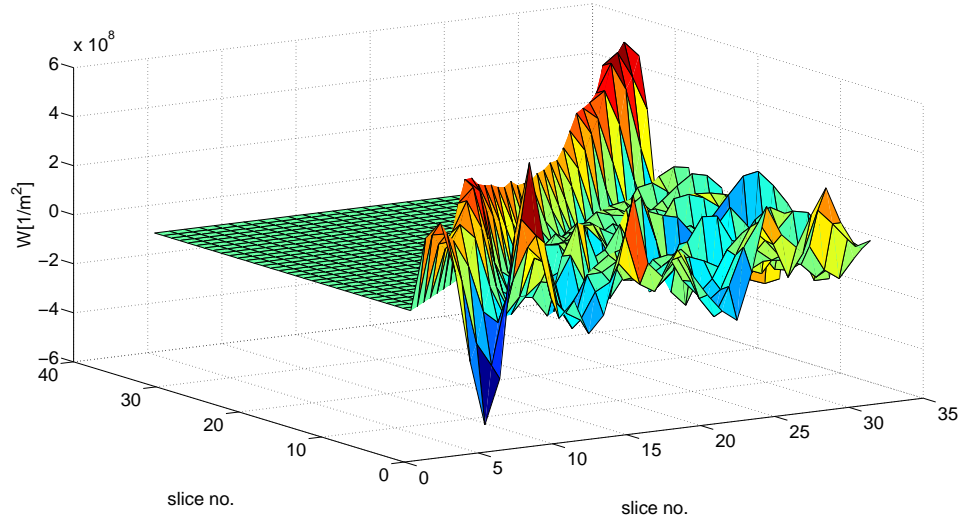


Figure 5.24: Wake matrix for  $\rho_e = 5 \cdot 10^{11} \text{ N}_e/\text{m}^3$ .

step used for the interaction simulation is 1 ps. The question the instability simulation should be able to answer is, at which e-cloud density the instability of a single bunch may occur. Therefore, the wake matrices were computed for e-cloud densities below and above the analytically computed threshold

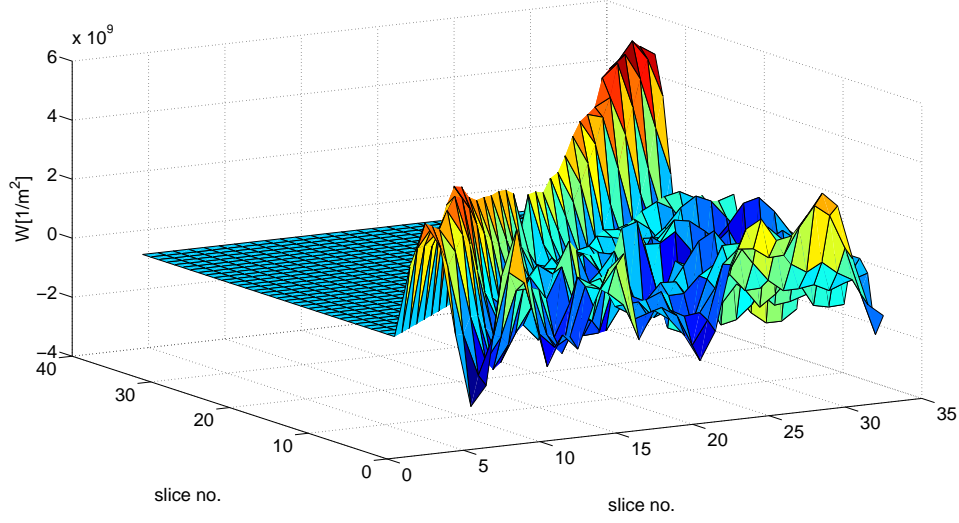


Figure 5.25: Wake matrix for  $\rho_e = 5 \cdot 10^{12} \text{ N}_e / \text{m}^3$ .

$\rho_{th} = 1.4 \cdot 10^{12} \text{ m}^{-3}$ :  $\rho_e = 1 \cdot 10^{11} \text{ N}_e / \text{m}^3$ ,  $\rho_e = 5 \cdot 10^{11} \text{ N}_e / \text{m}^3$  (Figure 5.24),  $\rho_e = 2 \cdot 10^{12} \text{ N}_e / \text{m}^3$  and  $\rho_e = 5 \cdot 10^{12} \text{ N}_e / \text{m}^3$  (Figure 5.25).

Plugging the wake matrices and the machine description in K. Ohmi's tracking program PETHS [Ohmi 2001a] the bunch was tracked for 2048 turns.

The simulation for  $\rho_e = 1 \cdot 10^{11} \text{ N}_e / \text{m}^3$  and  $\rho_e = 5 \cdot 10^{11} \text{ N}_e / \text{m}^3$ , as shown in Figure 5.26 for  $\rho_e = 5 \cdot 10^{11} \text{ N}_e / \text{m}^3$  doesn't reveal any emittance growth over the 2048 turns. The FFT of the vertical or horizontal centroid position of the bunch during 2048 turns gives the corresponding vertical or horizontal tune spectra. The vertical tune spectra for  $\rho_e = 5 \cdot 10^{11} \text{ N}_e / \text{m}^3$  (Figure 5.27) show only the peak at the betatron frequency of 38kHz. However, for higher e-cloud densities ( $\rho_e = 2 \cdot 10^{12} \text{ N}_e / \text{m}^3$  and  $\rho_e = 5 \cdot 10^{12} \text{ N}_e / \text{m}^3$ ) the vertical tune spectra exhibit side bands (Figure 5.28) indicating incoherent effects on the bunch. At the same time, the horizontal tune spectra for  $\rho_e = 2 \cdot 10^{12} \text{ N}_e / \text{m}^3$  in Figure 5.29 show only the peak at the horizontal betatron frequency. Figures 5.30 and 5.30 show the emittance growth for  $\rho_e = 2 \cdot 10^{12} \text{ N}_e / \text{m}^3$  and  $\rho_e = 5 \cdot 10^{12} \text{ N}_e / \text{m}^3$  which is clearly more moderate for the lower e-cloud density.

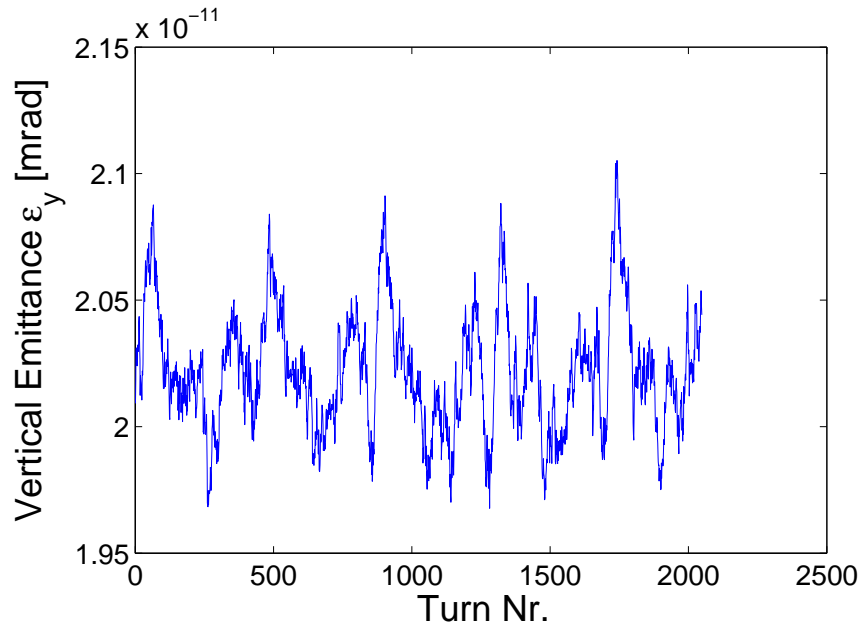


Figure 5.26: Almost no emittance growth after 2048 turns with  $\rho_e = 5 \cdot 10^{11} \text{ N}_e/\text{m}^3$ .

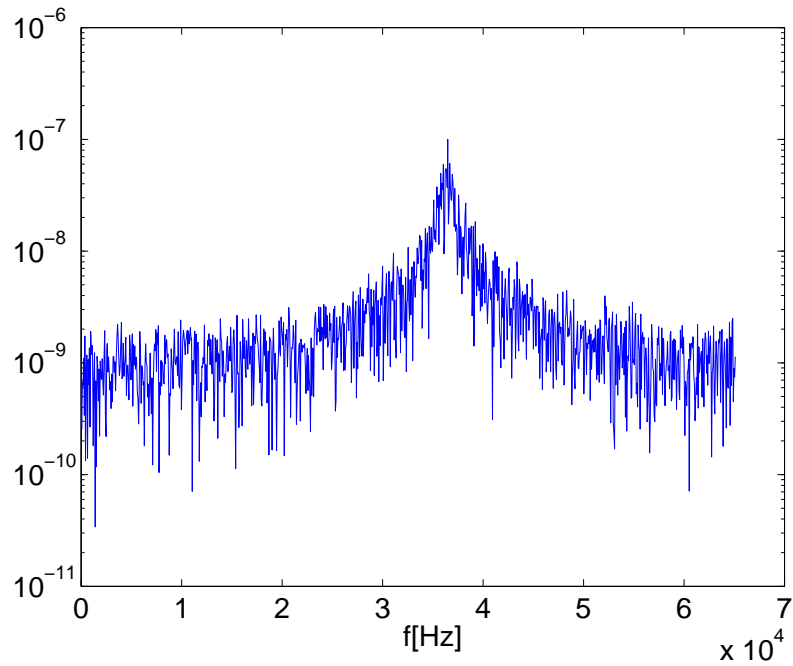


Figure 5.27: Vertical tune spectra for  $\rho_e = 5 \cdot 10^{11} \text{ N}_e/\text{m}^3$ .

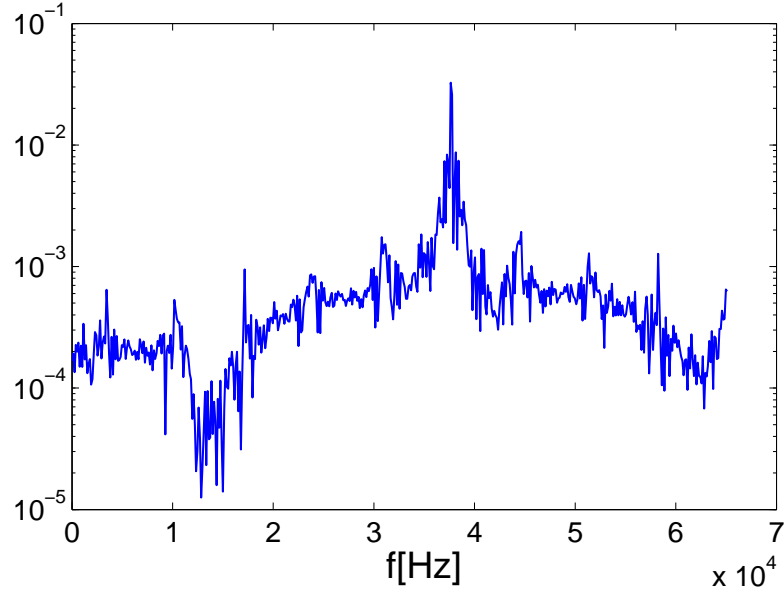


Figure 5.28: Sidebands in the vertical tune spectra for  $\rho_e = 5 \cdot 10^{12} \text{ N}_e/\text{m}^3$ .

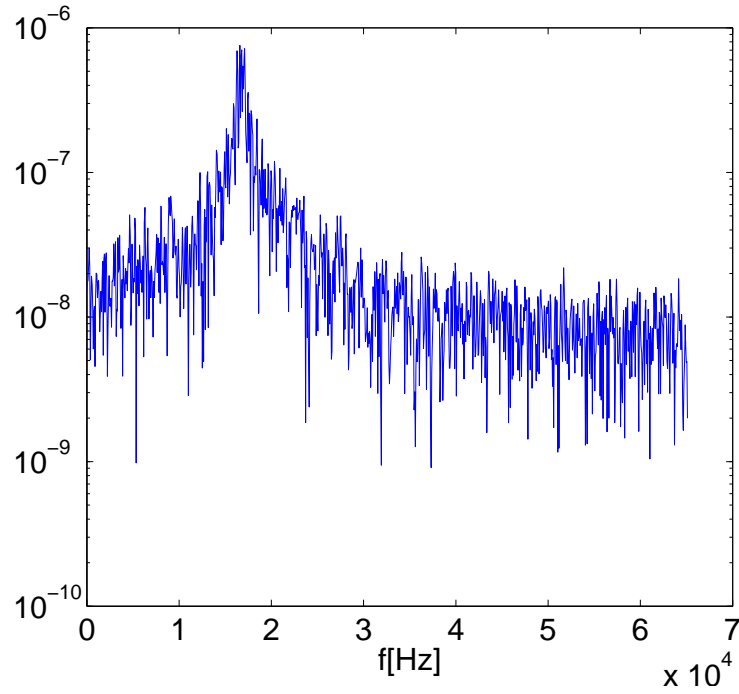


Figure 5.29: Horizontal tune spectra for  $\rho_e = 2 \cdot 10^{12} \text{ N}_e/\text{m}^3$ .

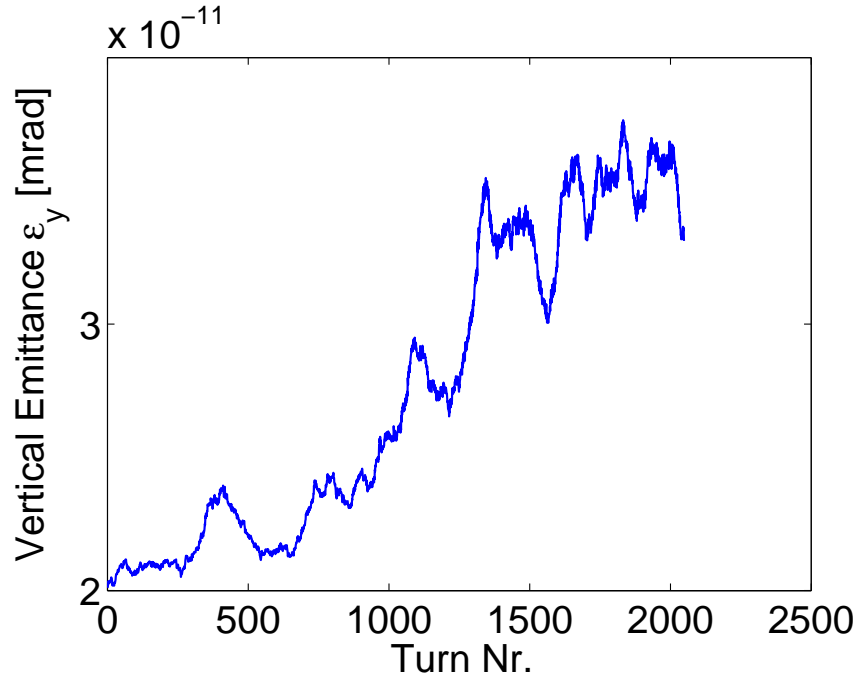


Figure 5.30: Emittance growth after 2048 turns for  $\rho_e = 2 \cdot 10^{12} \text{ N}_e/\text{m}^3$ .

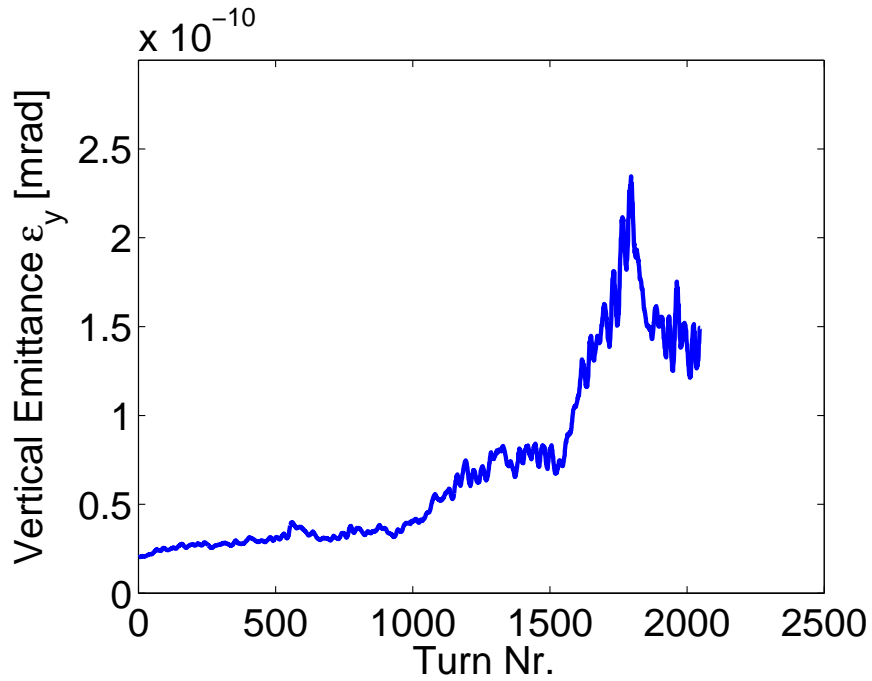


Figure 5.31: Emittance growth after 2048 turns for  $\rho_e = 5 \cdot 10^{12} \text{ N}_e/\text{m}^3$ .

The tracking simulation using the pre-computed wake matrix for the given bunch was able to predict the instability. As in the measurements, the simulation for e-cloud densities above threshold also shows sidebands in the betatron tune spectra. The simulated emittance growth seems realistic, even more the emittance from the simulation with  $\rho_e = 5 \cdot 10^{12} \text{ N}_e/\text{m}^3$  seems to match the measured longtime emittance ( 140 pm) from the beam scrubbing run with 480 bunches presented in Figure 5.22. Although further validation of the procedure is needed, it seems that such a simulation may also be used to numerically estimate the threshold e-cloud density.

## CHAPTER 6

# Summary

---

The main focus in this work was set to a development of a tool for simulation of the interaction of relativistic bunches with non-relativistic parasitic charged particles. The MOEVE PIC Tracking simulations of the interaction between positron bunches and electron clouds in this work gave a detailed insight of the behavior of both particle species during and after the interaction. Moreover MOEVE PIC Tracking is already being successfully used to simulate the interaction of electron beam with parasitic ion distributions under the influence of ion-clearing electrodes ([Pöplau 2012], [Meseck 2012]).

The simulation of single bunch instability due to the interaction with electron clouds is very challenging since the bunch has to be tracked for many turns in the storage ring. Thereby at each turn the influence of the e-clouds in the storage ring should be applied. Usually the kick on the bunch particles from the e-cloud is applied lumped on one or more positions (IP-Interaction Point) in the ring, substituting the cumulative kick from e-clouds in different parts of the storage ring i.e. dipoles, quadrupoles or drift sections. At the IPs the interaction could be simulated for instance with MOEVE PIC Tracking or the kick on the bunch particles could be applied according to a precomputed wake matrix. After the IP the bunch is transferred through the linear optics of the machine to the next IP. The simulation approach with the wake matrix as explained in this work is a very fast way to estimate the bunch stability for certain e-cloud density compared with PIC simulation at each IP for many turns of the beam. The ultimate aim of the simulation procedure presented in this work is investigation of the stability for different beam parameters (i.e. filling schemes) and cloud densities.

The results from the simulations for two storage rings (KEKB-LER) and PETRAIII are encouraging that the procedure can be applied for a fast estimation of e-cloud effects on the beam for any current and future storage ring machines with positively charged bunches.





# APPENDIX A

## Machine Parameter

---

### A.1 PETRAIII

Parameter	Symbol	PETRA III
Circumference	$L$	2304 m
Beam energy	$E_b$	6 GeV
Length (rms)	$\sigma_z$	12 mm
Emittance	$\varepsilon_x$	1nm
	$\varepsilon_y$	0.01nm
Synchrotron tune	$\nu_s$	0.049
Betatron tune	$\nu_{x(y)}$	36.13/30.29
Radiation Damping	horizontal	19.75 ms
	vertical	19.75 ms
	longitudinal	9.84 ms
Momentum compaction factor	$\alpha$	$1.2010^{-4}$
RF Frequency	RF	499.564 MHz
Beam Current	$I$	100 mA
Beam Charge	$Q$	769 nC
Bunch Charge	$Q_b$	1.6 nC
Positrons per Bunch	$N_b$	$10^{10}$
Mean $\beta$ function	$\beta_{x/y}$	15 m
Transverse beam size (rms)	$\sigma_x$	122.47 $\mu\text{m}$
	$\sigma_y$	17.321 $\mu\text{m}$

Table A.1: PETRA III machine parameters.

## A.2 KEKB-LER

Parameter	Symbol	KEKB-LER
Circumference	$L$	3016 m
Beam energy	$E_b$	3.5 GeV
Population	$N_b$	$3.3 \cdot 10^{10}$
Charge	$Q$	5.28 nC
Length (rms)	$\sigma_z$	6 mm
Transverse beam size (rms)	$\sigma_x$ $\sigma_y$	420 $\mu\text{m}$ 60 $\mu\text{m}$
Synchrotron tune	$\nu_s$	0.024
Betatron tune	$\nu_{x(y)}$	45.51/43.57
Damping time	$\tau_{x(y)}$	4000 Turns

Table A.2: Bunch parameters of the low energy ring of the KEK B-factory used for modelling the interaction with the e-cloud.

## A.3 ILC damping ring

Parameter	symbol	ILC e+ DR
Circumference	$L$	6695 m
Beam energy	$E_b$	5 GeV
Population	$N_b$	$2.0 \cdot 10^{10}$
Charge	$Q$	3.22 nC
Length (rms)	$\sigma_z$	9 mm
Beam size(rms)	$\sigma_x$ $\sigma_y$	156 $\mu\text{m}$ 7.8 $\mu\text{m}$
Damping time	$\tau_{x(y)}$	1150 turns

Table A.3: Bunch parameters of the low energy ring of the ILC positron damping ring.

## APPENDIX B

# Input file

---

```
Ellipse_Half_Axis_a:
0.005
Ellipse_Half_Axis_b:
0.005
Maximum_discretisation_points_in_each_coordinate_direction:
Nx_max
200
Ny_max
200
Nz_max
81
x_Axis
-0.005 s 31 -0.001 s 20 0.001 s31 0.005
y_Axis
-0.005 s 51 -0.0001 s 40 0.0001 s 51 0.005
BOUNDARY
Circlexy
Circlexy
Circlexy
Circlexy
Dirichlet
Dirichlet
SOLVER:_MG,_MGCG,_CG,_SOR,_BiCG,_BiCGSTAB,_PCBiCG
BiCGSTAB
DISCRETIZATION:_equi:0;non-equi:1
1
NUM_ERROR:
1.e-6
TESTEXAMPLE:
_1:sin,_2:exp(16..),_3:cos_4:sphere,_5:Analitic,_6:Interaction
6
```



# Bibliography

- [Balewski 2004] K. Balewski and Deutsches Elektronen-Synchrotron (Hamburg). *PETRA III a Low Emittance Synchrotron Radiation Source*. Technical Design Report 2004-035, 2004. [1](#), [120](#)
- [Bassetti 1980] M. Bassetti and G.A. Erskine. *Closed expression for the electrical field of a two-dimensional Gaussian charge*. CERN-ISR-TH/80-06, 1980. [62](#)
- [Benedetto 2007] E. Benedetto, G. Rumolo, D. Schulte, R. Tomas, F. Zimmermann, G. Franchetti, K. Ohmi, M. Pivi, T. Raubenheimer, W. Fischer, K. Sonnad and J-L Vay. *Modeling incoherent electron cloud effects*. In Particle Accelerator Conference, 2007. PAC. IEEE, pages 3393–3395, 2007. [103](#), [118](#)
- [Birdsall 1991] C.K. Birdsall and A.B. Langdon. Plasma physics via computer simulation. Adam Hilger series on plasma physics. Adam Hilger, 1991. [42](#), [44](#), [71](#), [72](#)
- [Brüning 2004] O.S. Brüning, P. Collier, P. Lebrun, S. Myers, R. Ostojic, J. Poole and P. Proudlock. LHC Design Report. CERN, Geneva, 2004. [1](#)
- [Bruning 1999] O. Bruning, F. Caspers, I.R. Collins, O. Grobner, B. Henrist, N. Hilleret, J. M. Laurent, M. Morvillo, M. Pivi, F. Ruggiero and X. Zhang. *Electron cloud and beam scrubbing in the LHC*. In Particle Accelerator Conference, 1999. Proceedings of the 1999, volume 4, pages 2629–2631 vol.4, 1999. [121](#)
- [Chao 1993] A.W. Chao. Physics of collective beam instabilities in high energy accelerators. Wiley, New York, NY, 1993. [29](#)
- [Chapman 2007] B. Chapman, G. Jost and R. van der Pas. Using OpenMP: Portable Shared Memory Parallel Programming (Scientific and Engineering Computation). The MIT Press, 2007. [72](#)
- [Committee 2003] International Linear Collider Technical Review Committee and International Committee for Future Accelerators. International linear collider technical review committee second report. SLAC report. Stanford Linear Accelerator Center, 2003. [63](#)

- [Crittenden 2010] James Crittenden, Joseph Calvey, Gerald Dugan, David Kreinick, Zhidong Leonget *al.* *Progress in Studies of Electron-Cloud-Induced Optics Distortions at CesrTA*. In Proceedings of IPAC 2010 (1st International Particle Accelerator Conference), Kyoto, Japan, pages 1976–1978, 2010. 103
- [Demma 2007] T. Demma, S. Petracca, F. Ruggiero, G. Rumolo and F. Zimmermann. *Maps for electron cloud density in Large Hadron Collider dipoles*. Phys. Rev. ST Accel. Beams, vol. 10, page 114401, Nov 2007. 35
- [Demma 2009] T. Demma, A. Drago, S. Guiducci, M. Zobov and K. Ohmi. *A simulation study of the electron cloud instability at DAFNE*. In Proceedings of Particle Accelerator Conference 2009, Vancouver, Canada ., 2009. 118
- [DES 2012a] DESY, Hamburg, Germany, <http://www.xfel.eu/>. *European Free-Electron Laser XFEL*, 2012. 76
- [DES 2012b] DESY, Hamburg, Germany, <http://flash.desy.de/>. *Free-electron laser FLASH*, 2012. 76
- [DES 2013] DESY, Hamburg, Germany, <http://petra3.desy.de/>. *PE-TRA III*, 2013. 120
- [Feynman 2006] R.P. Feynman, R.B. Leighton and M. Sands. The Feynman Lectures on Physic, The Definitive Edition, volume 2. Pearson Education Inc, 2006. 5, 8
- [Flanagan 2005] J.W. Flanagan, K. Ohmi, H. Fukuma, S. Hiramatsu, M. Tobiya *et al.* *Observation of vertical betatron sideband due to electron clouds in the KEKB LER*. Phys.Rev.Lett., vol. 94, page 054801, 2005. 95, 119
- [Flöttmann 2000] K. Flöttmann. *ASTRA*. DESY, Hamburg, [www.desy.de/~mpyf10](http://www.desy.de/~mpyf10), 2000. 45, 73, 76
- [Funakoshi 2001] Y. Funakoshi, K. Akai, A. Enomoto, J. Flanagan, H. Fukuma, K. Furukawa, J. Haba, S. Hiramatsu, K. Hosoyama, T. Ieiri, N. Iida, H. Ikeda, S. Kamada, T. Kamitani, S. Kato, M. Kikuchi, E. Kikutani, H. Koiso, S.I. Kurokawa, M. Masuzawa, T. Matsumoto, T. Mimashi, T.T. Nakamura, Y. Ogawa, K. Ohmi, Y. Ohnishi, S. Ohsawa, N. Ohuchi, K. Oide, E.A. Perevedentsev, K. Satoh, M. Suetake, Y. Suetsugu, T. Suwada, F. Takasaki,

- M. Tawada, M. Tejima, M. Tobiyama, S. Uno, Y. Wu, N. Yamamoto, M. Yoshida, S. Yoshimoto, M. Yoshioka and F. Zimmermann. *KEKB performance*. In Particle Accelerator Conference, 2001. PAC 2001. Proceedings of the 2001, volume 5, pages 3546 –3548 vol.5, 2001. 64, 84
- [Furman 1997] M. A. Furman and G. R. Lambertson. *The electron-cloud instability in the arcs of the PEP-II positron ring*. In LBNL41123/CBP Note-246, PEP-II AP Note 97.27, pages 15–18, 1997. 62
- [Furman 1998] M. A. Furman. *The Electron cloud effect in the arcs of the LHC*. 1998. 33
- [Furman 2002] M. A. Furman and M. T. F. Pivi. *Probabilistic model for the simulation of secondary electron emission*. Phys. Rev. ST Accel. Beams, vol. 5, page 124404, Dec 2002. 35
- [Holzer 2006] B. Holzer. *CAS Lectures on Beam Transverse Dynamics I,II,III*. Website, 2006. Available online at <http://cas.web.cern.ch/cas/Zakopane-2006/PDFs/Holzer.pdf>; visited on January 8th 2010. 18, 24
- [Jackson 1999] J. D. Jackson. Classical Electrodynamics. Wiley, New York, NY, 3rd ed. édition, 1999. 5
- [Loïez 1997] P. Loïez, P. Rakosy and L. Guiraud. *Beam screens for the LHC beam pipes. Les conduits pour les faisceaux LHC*, May 1997. CERN PhotoLab/Accelerators/Vacuum, <http://cdsweb.cern.ch/record/39110>. 36
- [Markovík 2005] A. Markovík. *A numerical computation of space-charge fields of electron bunches in a beam pipe of elliptical shape*. TESLA-Report 2005-21, DESY, Hamburg, 2005. 57
- [Markovik 2009] A. Markovik, G. Pöplau and U. van Rienen. *Computation of a Two Variable Wake Field Induced by an Electron Cloud*. In Proc. of the 10th International Computational Accelerator Physics Conference, San Francisco, USA, pages 314–317, Aug. 2009. 103
- [Markovík 2010] A. Markovík, G. Pöplau and U. van Rienen. *3D PIC Computation of a Transversal Tune Shift caused by an Electron Cloud in a Positron Storage Ring*. In Proceedings of IPAC 2010 (1st International Particle Accelerator Conference), Kyoto, Japan, pages 1928–1930, 2010. 103

- [Markovik 2011] A. Markovik, G. Pöplau and U. van Rienen. *Simulation of the Single Bunch Instability due to the Electron Cloud Effect by Tracking with a Pre-Computed 2D Wake Matrix*. In Proceedings of IPAC 2011 (2nd International Particle Accelerator Conference), San Sebastian, Spain, pages 2247–2249, 2011. [103](#)
- [Markovik 2012a] A. Markovik, G. Pöplau and U. van Rienen. *Computation of the 2D Transverse Wake Function of an Electron Cloud for Different Parameters*. In Proceedings of IPAC 2012 (3rd International Particle Accelerator Conference), New Orleans, USA, pages 280–282, 2012. [103](#)
- [Markovik 2012b] A. Markovik and U. van Rienen. *Tracking of a PETRA III Positron Bunch with a Pre-Computed Wake Matrix due to Electron Clouds*. In Proc. of the 11th International Computational Accelerator Physics Conference, Warnemünde, Germany, pages 31–33, 2012. [103](#)
- [Meseck 2012] A. Meseck, G. Pöplau and U. van Rienen. *Numerical Studies on the Influence of Fill Patterns on Ion Clouds*. In Proceedings of ICAP 2012 (Proceedings of the 11th International Computational Accelerator Physics Conference), Rostock-Warnemünde, Germany, pages 146–148, 2012. [129](#)
- [Ohmi 1995] K. Ohmi. *Beam-Photoelectron Interactions in Positron Storage Rings*. Phys. Rev. Lett., vol. 75, pages 1526–1529, Aug 1995. [36](#)
- [Ohmi 2000a] K. Ohmi and F. Zimmermann. *Head-Tail Instability Caused by Electron Clouds in Positron Storage Rings*. Phys. Rev. Lett., vol. 85, pages 3821–3824, Oct 2000. [36](#)
- [Ohmi 2000b] K. Ohmi and F. Zimmermann. Study of head-tail effect caused by electron cloud. KEK Preprint. High Energy Accelerator Research Organization (KEK), 2000. [62](#)
- [Ohmi 2001a] K. Ohmi. *Particle-in-cell simulation of beam-electron cloud interactions*. In Particle Accelerator Conference, 2001. PAC 2001. Proceedings of the 2001, volume 3, pages 1895–1897 vol.3, 2001. [118](#), [124](#)
- [Ohmi 2001b] K. Ohmi, S. Heifets and F. Zimmermann. *Study of coherent tune shift caused by electron cloud in positron storage rings*. no. CERN-SL-2001-062-AP, page 4 p, Oct 2001. [103](#)
- [Ohmi 2001c] K. Ohmi, F. Zimmermann and E. Perevedentsev. *Wake-field and fast head-tail instability caused by an electron cloud*. Phys. Rev. E, vol. 65, page 016502, Dec 2001. [36](#), [39](#), [89](#), [108](#), [109](#), [114](#)



- [Ohmi 2005a] K. Ohmi. *Electron cloud effect in damping rings of linear colliders*. In 31st ICFA Beam Dynamics Workshop on Electron Cloud Effects (ECLOUD04), Napa, California, Apr 2005. 103
- [Ohmi 2005b] K. Ohmi. *Electron Cloud Instabilities in the Damping Ring of International Linear Collider*. In International Linear Collider Workshop, Snowmass, Colorado, July 2005. 108
- [Ohmi 2008] K. Ohmi. private communication, 2008. 110
- [Petracca 2011] S. Petracca, A. Stabile, T. Demma and G. Rumolo. *A Formula of the Electron Cloud Linear Map Coefficient in a Strong Dipole*. In Proceedings of IPAC 2011 (2nd International Particle Accelerator Conference), San Sebastian, Spain, Sep 2011. 35
- [Pöplau 2005] G. Pöplau, U. van Rienen, S.B. van der Geer and M.J. de Loos. *A Multigrid Based 3D Space-Charge Routine in the Tracking code GPT*. In M. Berz and K. Makino, editeurs, Computational Accelerator Physics 2002 (Proceedings of the 7th International Computational Accelerator Physics Conference, East Lansing, Michigan, USA), numéro 175 de Institute of Physics Conference Series, pages 281–288, Bristol and Philadelphia, 2005. Institute of Physics Publishing. 41, 43, 44
- [Pöplau 2012] G. Pöplau, A. Meseck, A. Marković and U. van Rienen. *Simulations for Ion Clearing in an ERL*. In Proceedings of ICAP 2012 (Proceedings of the 11th International Computational Accelerator Physics Conference), Rostock-Warnemünde, Germany, pages 143–145, 2012. 129
- [Rumolo 2001] G. Rumolo and F. Zimmermann. *Simulation of single bunch instabilities driven by electron cloud in the SPS*. In Particle Accelerator Conference, 2001. PAC 2001. Proceedings of the 2001, volume 3, pages 1886 –1888 vol.3, 2001. 62
- [Rumolo 2002] G. Rumolo and F. Zimmermann. *Electron cloud simulations: beam instabilities and wakefields*. Phys. Rev. Spec. Top. Accel. Beams, vol. 5, no. 12, page 121002, 2002. 39
- [van der Geer ] S.B. van der Geer and M.J. de Loos. *General Particle Tracer (GPT)*. Pulsar Physics, De Bongerd 23, 3762 XA Soest, The Netherlands, [www.pulsar.nl/gpt](http://www.pulsar.nl/gpt). release 3.03 x32. 76
- [van Loan 1992] C. van Loan. Computational Frameworks for the Fast Fourier Transform, volume 10 of *Frontiers in Applied Mathematics*. SIAM, Philadelphia, 1992. 53

- [van Rienen 2001] U. van Rienen. Numerical Methods in Computational Electrodynamics. Lecture Notes in Computational Science and Engineering. Springer, January 2001. 31, 46, 57
- [Vay 2009] J.-L. Vay, C.M. Celata, M.A. Furman, G. Penn, M. Venturini et al. *Update on electron-cloud simulations using the package WARP-POSINST*. In Proceedings of Particle Accelerator Conference 2009, Vancouver, Canada., pages 4719–4721, 2009. 118
- [Wanzenberg 2003] R. Wanzenberg. *Simulation of Electron Cloud Effects in the PETRA Positron Storage Ring*. 2003. <http://www.desy.de/~mpywar/paper/DESY-M-03-02.pdf>. 120
- [Wanzenberg 2004] R. Wanzenberg. *Prediction of electron cloud effects in the synchrotron light source Petra III*. The 31st ICFA Advanced Beam Dynamics Workshop on Electron-Cloud Effects "ECLLOUD'04", April 2004. 34
- [Wanzenberg 2010] R. Wanzenberg. *Emittance Growth and Tune Spectra at PETRA III*. In Proc. 49th ICFA Advanced Beam Dynamics Workshop on Electron Cloud Physics (ECLLOUD'10), Cornell University, Ithaca, NY, USA, Oct. 2010. "<http://www.lepp.cornell.edu/Events/ECLLOUD10/>". 120, 121
- [Wanzenberg 2012] R. Wanzenberg. *Observation of Electron Cloud Phenomena at PETRA III*. In Proceedings of the International Workshop on Electron-Cloud Effects (ECLLOUD'12), La Biodola, Isola d'Elba, Italy, June 2012. 121
- [Weiland 1977] T. Weiland. *Eine Methode zur Lösung der Maxwellschen Gleichungen für sechskomponentige Felder auf diskreter Basis*. In AEÜ - International Journal of Electronics and Communications, volume 31, pages 116–120, 1977. 52
- [Wille 1992] K. Wille. Physik der Teilchenbeschleuniger und Synchrotronstrahlungsquellen: eine Einführung. Teubner Studienbücher Physik. Teubner, Stuttgart, 1992. 24
- [Zimmermann 2003] F. Zimmermann and G. Rumolo. *Practical User Guide for ECloud*. CERN, CERN-SL-Note-2002-016, <http://wwwslap.cern.ch/collective/electron-cloud/Programs/Ecloud/eccloud.html>, 2003. 34, 35

## Selbständigkeitserklärung

Hiermit erkläre ich, dass ich die vorliegende Dissertation mit dem Titel "Simulation of the Interaction of Positively Charged Beams and Electron Clouds" selbständig und ohne fremde Hilfe und nur unter Verwendung der von mir angegebenen Quellen und Hilfsmittel verfasst habe.

Rostock, 25. Juni 2013  
Aleksandar Marković

## Theses

1. The incoherent (head-tail) effect on the bunch due to the interaction with electron clouds (e-clouds) leads to a blow up of the transverse beam size in storage rings operating with positively charged beams. Even more the e-cloud effects are considered to be the main limiting factor for high current, high-brightness or high-luminosity operation of future machines.
2. MOEVE PIC Tracking is a Particle In Cell program created during this work for tracking both relativistic and nonrelativistic charged particle distributions under the influence of external electromagnetic fields and their own space charge fields.
3. The space charge field of a particle distribution computed in a beam pipe is strongly influenced by the shape of the boundary and the type of boundary conditions applied in the numerical computation. MOEVE PIC Tracking features the possibility to define an elliptical cross-section of the conducting beam pipe which is approximated as perfect electrical conductor (PEC).
4. The tracking results of the MOEVE PIC Tracking are in accordance with the results of other established particle tracking programs (i.e. ASTRA and GPT).
5. MOEVE PIC Tracking simulates the interaction of relativistic bunches with nonrelativistic electron clouds in a beam pipe with or without an external magnetic field of a dipole or quadrupole magnets.
6. At each time step of the interaction simulation, the space charge fields are computed in parallel, for the electron cloud in the laboratory frame and for the relativistic bunch in its rest frame.
7. For beam energies of GeV order the own magnetic and the electric forces cancel each other. Hence the only force that affects the bunch particles during the interaction is the space-charge force of the e-cloud. During the interaction the electrons experience the own and the space-charge force from the beam.
8. During the interaction electrons near the beam axis oscillate in the transverse plane due to the potential of the bunch and the repelling own

space-charge force. The oscillation depends on the longitudinal charge profile of the bunch.

9. During the interaction in a drift space the e-cloud concentrates on the beam axis. Inside a dipole magnet the e-cloud concentration forms vertical stripes left and right of the beam axis which could lead to a coupling of the vertical betatron motion with the synchrotron motion of the bunch particles.
10. The simulations with MOEVE PIC Tracking show a characteristic increase of the coherent vertical tune due to the interaction with e-clouds.
11. Simulations with transversally displaced longitudinal parts of the bunch demonstrated the head-tail coupling between the bunch part perturbing the cloud and the following bunch parts.
12. The wake field due to the beam - e-cloud interaction can not be treated as a function of the distance between the excitation and the part of the bunch receiving the kick. The wake field modelling the beam - e-cloud interaction should be a two variable function of the position of both the excitation and the part of the bunch receiving the kick.
13. The numerically pre-computed transverse wake due to the interaction with the e-cloud has to be a wake matrix which can be extracted from a series of detailed beam - e-cloud interaction simulations with MOEVE PIC Tracking. Thereby, the 3D bunch is longitudinally divided into a number of slices. At each interaction simulation a single slice which has a transverse displacement respective to the other slices, induces a transverse kick from the e-cloud on the following slices.
14. In order to apply the computed wake matrix for the bunch tracking it is necessary to assume properties of the wake field such as linearity, superposition and time invariance.
15. In order to estimate the stability of a single bunch interacting with e-clouds it needs to be tracked over the time of at least one synchrotron period. The wake kick from the e-cloud is applied lumped at each turn of the bunch in the storage ring.
16. The tracking through the linear optics of the storage ring using the pre-computed wake matrix for the given bunch, corresponding the beam scrubbing run at PETRAIII, was able to predict the instability. As in the measurements the simulation for e-cloud densities above threshold show also sidebands in the betatron tune spectra.

## Abstract

The incoherent (head-tail) effect on the bunch due to the interaction with electron clouds (e-clouds) leads to a blow up of the transverse beam size in storage rings operating with positively charged beams. Even more the e-cloud effects are considered to be the main limiting factor for high current, high-brightness or high-luminosity operation of future machines. Therefore the simulation of e-cloud phenomena is a highly active field of research. The main focus in this work was set to a development of a tool for simulation of the interaction of relativistic bunches with non-relativistic parasitic charged particles. The result is the Particle-In-Cell Program MOEVE PIC Tracking which can track a 3D bunch under the influence of its own and external electromagnetic fields but first and foremost it simulates the interaction of relativistic positively charged bunches and initially static electrons. In MOEVE PIC Tracking the conducting beam pipe can be modeled with an arbitrary elliptical cross-section to achieve more accurate space charge field computations for both the bunch and the e-cloud. The simulation of the interaction between positron bunches and electron clouds in this work gave a detailed insight of the behavior of both particle species during and after the interaction. Further and ultimate goal of this work was a fast estimation of the beam stability under the influence of e-clouds in the storage ring. The standard approach to simulate the stability of a single bunch is to track the bunch particles through the linear optics of the machine by multiplying the 6D vector of each particle with the transformation matrices describing the lattice. Thereby the action of the e-cloud on the bunch is approximated by a pre-computed wake kick which is applied on one or more points in the lattice. Following the idea of K.Ohmi the wake kick was pre-computed as a two variable function of the bunch part exiting the e-cloud and the subsequent parts of a bunch which receive a transverse kick from the e-cloud. A series of detailed interaction simulations with MOEVE PIC Tracking resulted with a pre-computed wake matrix for the given bunch and e-cloud parameters which was applied in the tracking through the linear optics of the storage ring. The results from the simulations for the two storage rings (KEKB-LER) and PETRAIII are encouraging that the new procedure can be applied for a fast estimation of e-cloud effects on the beam for any current and future storage ring machines with positively charged bunches.

## Zusammenfassung

Der inkohärente (Head-Tail) Effekt auf den Bunch, der durch die Wechselwirkung mit Elektronen-Wolken (e-Clouds) hervorgerufen wird, führt zu einer Vergrößerung der transversalen Strahlgröße in Speicherringen, die mit positiv geladenem Strahl betrieben werden. Effekte durch e-Clouds gelten als der bedeutendste limitierende Faktor für den Betrieb zukünftiger Maschinen mit hohen Strömen, hoher Brightness oder hoher Luminosität. Deshalb ist die Simulation von e-Cloud-Phänomenen ein sehr aktiver Bereich der aktuellen Forschung. Der Schwerpunkt dieser Arbeit war die Entwicklung eines Werkzeugs zur Simulation der Wechselwirkung relativistischer Teilchen-Bunche mit nicht-relativistischen geladenen parasitären Teilchen. Das Ergebnis ist das Particle-In-Cell-Programm MOEVE PIC Tracking, das prinzipiell einen 3D Bunch unter dem Einfluss von eigenen und externen elektromagnetischen Feldern verfolgen kann. In erster Linie simuliert es jedoch die Wechselwirkung relativistischer positiv geladener Bunche mit zunächst statischen Elektronen. In MOEVE PIC Tracking wird das leitende Strahlrohr mit beliebigem elliptischen Querschnitt modelliert, um genauere Raumladungsfeldberechnungen sowohl für den Bunch als auch für die e-cloud zu erreichen. Die Simulation der Wechselwirkung zwischen Elektronen-Wolken und Positron-Bunchen in dieser Arbeit ermöglichte einen detaillierten Einblick in das Verhalten von beiden Teilchen-Spezies während und nach der Wechselwirkung. Weiteres und ultimatives Ziel dieser Arbeit war eine schnelle Abschätzung der Strahlstabilität unter dem Einfluss von e-clouds im Speicherring. Der Standard-Ansatz, um die Stabilität eines einzelnen Bunches zu simulieren ist, die Teilchen-Bunche durch die lineare Optik der Maschine zu verfolgen. Dazu wird der 6D Vektor jedes Teilchens mit den Transformationsmatrizen, die das Lattice beschreiben, multipliziert. Die Wirkung der e-Cloud auf den Bunch wird hierbei von einem vor-berechneten Wake-Kick approximiert, der dann an einem oder mehreren Punkten im Lattice angewendet wird. Einer Idee von K. Ohmi folgend wurde der Wake-Kick als 2D Wake-Funktion des Bunch-Teils, der die e-Cloud anregt und der nachfolgenden Teile des Bunches, die einen transversalen Kick von der e-Cloud erhalten, vorberechnet. Eine Reihe von detaillierten Wechselwirkungssimulationen mittels MOEVE PIC Tracking resultierten in der vorberechneten Wake-Matrix für den gegebenen Bunch und gegebene e-Cloud-Parameter, die dann beim Tracking durch die lineare Optik des Speicherrings angewendet wurde. Die Ergebnisse der Simulationen für die zwei Speicherringe KEKB-LER und PETRAIII zeigen, dass das neu entwickelte Verfahren für eine schnelle Abschätzung von e-Cloud-Effekten auf den Strahl für alle aktuellen und zukünftigen Speicherringe mit positiv

geladenen Bunchen angewendet werden kann.



